Microstructural evolution and hardness changes in ion irradiated Ni-based superalloys

A Dissertation Presented for the

Doctor of Philosophy

Degree

The University of Tennessee, Knoxville

Qinyun Chen

December 2024

© by Qinyun Chen, 2024
All Rights Reserved.

Acknowledgments

This research was sponsored by the Office of Nuclear Energy, U.S. Department of Energy under contract DE-NE0008971 and Nuclear Energy University Program NEUP 20-19367 with the University of Cincinnati and University of Tennessee, Dr. Sam Sham (NRC) as the technical program monitor. This research was performed, in part, using instrumentation (FEI Talos F200X STEM) sponsored by the Office of Fusion Energy Sciences, U.S. Department of Energy under contract DE-AC05-00OR22725 with UT-Battelle, LLC. We thank Dr. Michael Fahrmann and Haynes International for providing the bulk alloy materials for this work.

First and foremost, I am deeply grateful to my advisor, Dr. Steven Zinkle, for his continuous support, invaluable advice, and patience. I could not have persevered to the end without your guidance and encouragement. I am also thankful for the insightful feedback and valuable suggestions provided by my committee members, Drs. Maik Lang, Khalid Hattar, Eric Lass, and Shradha Agarwal.

Special thanks to Dr. Neal Evans and Dr. John Dunlap for their training on microscopy techniques and for understanding when I made mistakes. I am also grateful to Drs. Yan-Ru Lin, Ling Wang, Siwei Chen and Yao Li for their assistance with material characterization and guidance on transmission electron microscopy, as well as Dr. Pengcheng Zhu and Ryan Thier for their help with nanoindentation acquisition and sample preparation. I thank Dr. Yajie Zhao for guidance in APT data analysis and predicting precipitate size, which significantly contributed to my work. The help from our present group members, Zehui Qi, Emily Proehl, and other colleagues is appreciated.

To my husband and my parents, thank you for your unwavering love, support, and encouragement. Your belief in me has been my foundation and refuge, giving me the courage

to keep going and start anew. Finally, I thank myself for going through this challenging journey. My life is just beginning, and though I may not know precisely where the future will take me, I am sure that the present is precious and tomorrow will be better.

Abstract

Nickel-based superalloys are promising structural material candidates for molten salt reactors and other advanced nuclear reactors. However, traditional Ni alloys exhibit severe mechanical degradation after neutron irradiation, and the gamma-prime precipitates in these alloys are susceptible to dissolution during irradiation. This study focuses on the microstructure evolution and mechanical property changes of Ni-based superalloys subjected to ion irradiation at different temperatures and doses. Several high-performance commercial Ni-base superalloys (solid solution-strengthened Haynes 244, Haynes 214, and Hastelloy C-276, precipitation-strengthened Haynes 244 and Haynes 282) were irradiated with 8 MeV Ni ions to midrange doses of 1 and 10 dpa at 600 °C and 750 °C.

During 750 °C irradiation to 10 dpa, the Ni_2(Mo, Cr, W) precipitates in aged Haynes 244 exhibited remarkable stability. In contrast, such precipitates were partially dissolved in the 600 °C samples. For solid solution treated Haynes 244, the Ni_2(Mo, Cr) grew in both irradiated regions (500–1000 nm depth from the sample surface) and pristine regions subjected to long time high-temperature exposure, except in the 750 °C, 1 dpa sample, suggesting longer nucleation time is required at the high temperature close to the critical transformation temperature from short-range ordering to long-range ordering. $\gamma' - Ni_3Al$ precipitates grew in the solution annealed Haynes 214 under irradiation and thermal exposure. A high number density of $Cr_{23}C_6$ carbides was exclusively observed in the irradiated region of the 750 °C, 1 dpa sample, attached to the dislocation lines originating from mechanical polishing. $\gamma' - Ni_3$(Al, Ti) in Haynes 282 showed remarkable radiation resistance and thermal stability at 600 °C and 750 °C. No statistical difference in size and number density of precipitates was observed after irradiation. Hastelloy C-276 demonstrates superior metallurgy stability since there is no precipitation of Ni_2(Mo, Cr), μ phase, and

Mo-enriched carbides within the matrix after irradiation. The modified NHM model and the Ostwald ripening LSEM model were employed to predict precipitate evolution under thermal exposure and irradiation conditions. Factors that might impact the accuracy of models were discussed. The post-irradiation nanoindentation analysis revealed significant hardening for both solution-annealed Haynes 214 and Haynes 244. The superposition method and dispersed barrier hardening model were applied to correlate the microstructures with the mechanical properties. Tan's and Zhu's methods are applied to derive the yield strength from nanoindentation hardness. Overall, the yield strength predictions showed acceptable agreement with experimental data.

Table of Contents

1 Introduction **1**

2 Literature Review **3**

2.1 Nickel-based superalloys as candidates for next-generation fission reactors . . 3

2.2 Radiation effects on the microstructure and mechanical properties of Nickel alloys 6

2.2.1 Common mechanical property degradation 6

2.2.2 Precipitate stability under irradiation 10

2.3 Ion-irradiation alternative to neutron irradiation 15

3 Materials and Methods **18**

3.1 Materials and sample preparation 18

3.2 Methods 23

3.2.1 Ion irradiation 23

3.2.2 Nanoindentation 26

3.2.3 Atomic force microscopy 29

3.2.4 Atom probe tomography 29

3.2.5 Transmission electron microscopy 31

4 Results **34**

4.1 Phase stability under ion irradiation 34

4.1.1 $\gamma' - Ni_3(Al, Ti)$ 34

4.1.2 $Ni_2(Mo, Cr, W)$ precipitates 41

4.1.3 Other secondary phases . . . 52
4.1.4 Dislocation evolution . . . 57
4.2 Nanoindentation hardness . . . 60

5 Discussion **65**
5.1 Correlation between microstructure and mechanical properties . . . 65
5.1.1 Haynes 282 . . . 71
5.1.2 Haynes 214 . . . 73
5.1.3 Haynes 244 . . . 75
5.2 Phase stability and precipitate size prediction under irradiation conditions . 79
5.2.1 γ' precipitates . . . 79
5.2.2 Ni_2(Mo, Cr, W) precipitates . . . 81
5.2.3 μ phase and Mo-enriched carbides . . . 83
5.2.4 Models to predict precipitate evolution under irradiation . . . 85

6 Conclusions **96**

A Additional information **115**
A.1 Large precipitate size correction . . . 115
A.2 Phase stability . . . 118
A.2.1 γ' precipitates . . . 118
A.2.2 Ni_2(Mo, Cr, W) precipitates . . . 120
A.2.3 Simulation of electron diffraction pattern . . . 120
A.3 Nanoindentation hardness . . . 120

List of Tables

3.1 Nominal composition of Ni-based superalloys in weight percentage(wt%) . . 19
3.2 Heat treatment conditions of Nickel based superalloys before irradiation . . . 19
3.3 Irradiation matrix of the Ni-based superalloys 24

5.1 Key parameters of selected nickel based superalloys 66
5.2 Strengthening constants for solution strengthening in Nickel 68
5.3 Summary of the strengthening contribution, the superposed model strengths, and the measured strength converted from nanoindentation results for Haynes 282 72
5.4 Summary of the strengthening contribution, the superposed model strengths, and the measured strength converted from nanoindentation results for Haynes 214 74
5.5 Summary of the strengthening contribution, the superposed model strengths, and the measured strength converted from nanoindentation results for aged Haynes 244 76
5.6 Summary of the strengthening contribution, the superposed model strengths, and the measured strength converted from nanoindentation results for solutionized Haynes 244 SHT 78
5.7 Material parameters related diffusivity used in this work 84
5.8 Summary of TEM results and NHM simulated precipitate size in aged Haynes 244 under different irradiation conditions 89
5.9 The detailed comparison of precipitate size and number density between TEM observation and modified LSEM model in irradiation Haynes 214 92

A.1 Results of STEM-EDS analysis showing the size (average diameter), number density and volume fraction of γ' precipitates 119
A.2 Size and number density of precipitates in Haynes 214 under various irradiation conditions 119
A.3 Size and number density of features observed in aged Haynes 244 under various irradiation conditions 123
A.4 Size and number density of features observed in solutionized Haynes 244 under various irradiation conditions 123
A.5 Nanoindenation summary of Haynes 282 under various conditions 125
A.6 Nanoindentation summary of Haynes 214 under various conditions 125
A.7 Nanoindentation summary of aged Haynes 244 under various conditions . . 125
A.8 Nanoindentation summary of aged Haynes 244 under various conditions . . 125

List of Figures

2.1 Tensile property changes of (a) Hastelloy X-280 and (b) Inconel 702 depending on the test temperature and neutron exposure level [1]. 7

2.2 Dose dependence of void swelling at several particle sizes. The irradiation condition was 10^{-2} dpa/s and 600°C [2]. 10

2.3 Diffusion coefficients as a function of 1/T for a nickel-based alloy during irradiation at a displacement rate of 10^{-6} dpa/s. D_{rad} is the radiation enhanced diffusion coefficient calculated from rate theory equations for various sink annihilation probabilities, p. D_m and D_{th} are diffusion coefficients from radiation mixing and thermal diffusion, respectively [3]. 13

2.4 The γ' precipitate evolution in aged PE16(a, c) and overaged PE16(b, d) during neutron irradiation at 600°C. (a) and (b) presented the initial precipitate distribution before irradiation; (c) and (d) depicted the precipitates morphology after irradiation to the total dose of $5.4 \times 10^{22} n/cm^2$. Reproduced from Ref.[4]. 13

2.5 The change in γ' precipitate size and density in Ni-Al alloy as a function of size. The sample was irradiated by charge particles with the dose rate of 10^{-2} dpa/s at 550°C [5]. 14

2.6 Calculated temperature- and depth-dependent regions affected by the free surface and injected ions for Fe-10%Cr steel irradiated with 5 MeV Fe^{+} . . . 16

2.7 Damage and implantation profiles of Fe-15 at.% Cr alloys irradiated with 2 MeV Fe^{2+} ions irradiated at 300°C calculated with SRIM 2013 and the 3D distribution of Cr atoms observed using APT at different depths [6]. 17

3.1 (a) Schematic of the unit cell for the Pt_2Mo-type structure within an FCC matrix; (b) Schematic electron diffraction patterns of the FCC matrix, showing six different orientation variants along various FCC matrix zone axes [7]. 21
3.2 The mounted sample configuration consists of six samples. The defocused beam fully covered all samples. 24
3.3 Detailed duration at each temperature. Heating and cooling rates are not available. 25
3.4 SRIM estimated profiles of 8 MeV Ni ion with fluence of 2×10^{15} ions/nm^2 in Ni target. The correction factor is 1.5. 26
3.5 Example of bi-linear fitting: Plot of H^2 versus $1/h$ for Fe-1.4Mn before and after 6.4 MeV Fe^{3+} ion irradiation at 290 °C [8] 28
3.6 (a) The AFM image of a 1000 nm indent of 300 h aged Fe18Cr [9]. (b) The schematic diagram of the indent and the cross section. the semi ellipse with short axis a_i refers to the estimated contact periphery of the indenter with material [10]. The red dotted line shows the sinusoidal approximation of the pileup periphery. The blue dashed line shows the pileup shape with an equivalent area to the sinusoidal shape [9]. 29
3.7 The magnified region of implanted ion region with red meshes to calculate the dislocation network density in irradiated Haynes 282 (600 °C, 10 dpa). Tiny dots in green are the intersections between the dislocation network and mesh grids. 33

4.1 Titanium EDS maps highlighting the precipitate distribution in aged Haynes 282 irradiated by Ni ions to a midrange dose of 10 dpa at 600 °C: Profiling from the surface (Pt protective layer) to 3μm depth. Annotated in blue ellipsoids, we provide a representative example, illustrating one group with depths between 1200 nm and 1400 nm, for a comprehensive understanding of precipitate distribution. 35

4.2 The statistical depth dependence of γ' precipitates in irradiated aged Haynes 282 (600 °C, 10 dpa). 36
4.3 The summary of a statistical distribution (a) precipitate size and (b) number density of γ' precipitates in Haynes 282 under various conditions. The solid circles represent the data calculated from irradiated regions, and the hollow circles are based on the pristine regions in the same irradiated sample. . . . 37
4.4 TEM dark field images of Haynes 214 irradiated at 600 °C with a dose of (a) 1 dpa and (b) 10 dpa, captured along zone [011]. 39
4.5 Micrographs of Haynes 214 irradiated at 600 °C with a mid-range dose of 1 dpa: (a) The magnified TEM dark field image captured from the pristine region; (b) and (c) are electron diffraction patterns from the irradiated region and pristine region, respectively. 39
4.6 The summary of a statistical distribution (a) precipitate size and (b) number density of γ' precipitates in Haynes 214 under various conditions. The solid circles represent the data calculated from irradiated regions, and the hollow circles are based on the pristine regions in the same irradiated sample. . . . 40
4.7 (a) Dark-field image showing the precipitate distribution in aged Haynes 244 irradiated by Ni ions to a midrange dose of 1 dpa at 600 °C. Profiling extends from the surface (Pt protective layer) to a depth of approximately 4 µm; (b) Detailed STEM-EDS analysis reveals that the element distribution varies with radiation damage as a function of depth. The yellow rectangle highlights the W atoms enriched in the precipitates. 42
4.8 (a) STEM-EDS mapping of aged Haynes 244 irradiated at 750 °C with a mid-range dose of 10 dpa; (b) the corresponding atomic fraction of key elements in Ni_2(Mo, Cr, W) at different depths. 42
4.9 Dark field images of (a)Variant I and (b) variant II taken along zone [001] axis of 750 °C, 10 dpa irradiated aged Haynes 244 sample; (c) and (d) are the corresponding depth dependence of the precipitate size and number density distribution. 44

4.10 TEM micrographs of 244SHT irradiated at 600 °C with a mid-range dose of 1 dpa; (b) and (c) are the corresponding electron diffraction patterns of the irradiated region and pristine region, respectively. 46
4.11 APT analysis of Haynes 244 SHT irradiated to 1 dpa at 600 °C: (a) atomic concentrations and (b) 18 % Mo iso-concentration surfaces obtained from the pristine region. 47
4.12 Dark-field images of different grains selected from irradiated 244 SHT at 600 °C with a mid-range dose of 10 dpa. (b) and (c) are annotated images. . . . 47
4.13 (a) APT atom maps of various elements in the irradiated region of 244 SHT after irradiation at 600 °C to a mid-range dose of 10 dpa; (b) Si distribution and (c) Mo iso-concentration surface of the same region. 48
4.14 Concentration of (a) W and (b) Al at interfaces of Ni_2(Mo, Cr) precipitates and Al enriched clusters with matrix, respectively; Nearest neighbor distribution of (c) W and (d) Al in order of 10. 49
4.15 (a)STEM bright field image and (b) the electron diffraction of 244SHT irradiated at 750 °C with a mid-range dose of 1 dpa. 50
4.16 STEM-EDX results of irradiated Haynes 244-SHT (750 °C, 10 dpa). The first two are the high-angle annular dark field (HAADF) image and bright field image; the others are the Ni, Mo, Cr, and W EDX maps. 51
4.17 (a) TEM dark field image with a 10 μ m objective aperture along [001] zone axis, as highlighted by the red circle in (c); (b) STEM bright field image showing dislocation distribution; (c) and (d) show electron diffraction patterns, captured from the irradiated and pristine regions, respectively. . . . 53
4.18 (a)STEM bright field image, (b)STEM HAADF, and (c)-(f) EDS results of various elements. 54
4.19 APT atom maps of Haynes 214 following irradiation to 1 dpa at 750°in the irradiated region at a depth of 500 nm from the sample surface, showing the presence of two distinct precipitates. 54

4.20 (a) BF-STEM and (b) SAED images of the region at a depth of 650 nm to 900 nm in Hastelloy C-276 to a midrange dose of 10 dpa at 600 °C, and (c)-(f) detailed STEM-EDS results showing the distribution of various elements. . 56
4.21 (a) and (c) are the SEM images, (b) and (d) are the EDS mappings for grain boundaries in Hastelloy C-276 irradiated at 600 °C and 750 °C, respectively, with a mid-range dose of 10 dpa. 56
4.22 Comparison of (a) calculated SRIM profile and (b) experimental dislocation distribution of irradiated Haynes 282 (600 °C, 10 dpa). 58
4.23 Bright-field STEM (BF-STEM) images of Haynes 244 irradiated at 600 °C: (a–b) aged STD samples and (c–d) solutionized SHT samples, with (a, c) at 1 dpa and (b, d) at 10 dpa. 58
4.24 BF-STEM images of samples irradiated at 600 °C: (a–b) aged Haynes 282 and (c–d) Hastelloy C-276, with (a, c) at 1 dpa and (b, d) at 10 dpa. 59
4.25 The STEM-EDS results of irradiation safe analysis region in irradiated Haynes 282 (600 °C, 10 dpa): (a) STEM dark field image, (b) aluminum (Al) elemental mapping and (c) overlapping of (a) on (b). 60
4.26 (a) An example of the Nix-Gao fitting of the depth-dependent hardness of irradiated aged Haynes 282 (600 °C, 10 dpa); (b)The bulk equivalent hardness H_0 after pileup correction of various conditions. 62
4.27 (a) Hardness vs. depth, and (b)the bulk equivalent hardness H_0 after pileup correction of Haynes 214 under various conditions. 62
4.28 (a) Hardness vs. depth, and (b)the bulk equivalent hardness H_0 after pileup correction of Haynes 244 STD under various conditions. 63
4.29 (a) Hardness vs. depth, and (b)the bulk equivalent hardness H_0 after pileup correction of Haynes 244 SHT under various conditions. 63
4.30 Plot of h^* values versus H_0 for all measured Ni alloys. 64

5.1 Comparison of the model-predicted strength with the measured strength converted from nanoindentation and Vickers hardness for unirradiated and ion irradiated Haynes 282. 72

5.2 Comparison of the model-predicted strength with the measured strength converted from nanoindentation and Vickers hardness for unirradiated and ion irradiated Haynes 214. 74
5.3 Comparison of the model-predicted strength with the measured strength converted from nanoindentation and Vickers hardness for unirradiated and ion irradiated aged Haynes 244. 76
5.4 Dark field image of aged Haynes 244 along the [001] zone axis. The yellow rectangles highlight regions where dislocation shearing may have occurred. . 77
5.5 Comparison of the model-predicted strength with the measured strength converted from nanoindentation and Vickers hardness for unirradiated and ion irradiated solutionized Haynes 244. 78
5.6 The diffusion coefficients for Mo in Ni matrix under Ni ion irradiation at a steady state are presented as functions of reciprocal temperature, considering a damage rate of 10^{-3} dpa/s. 86
5.7 Calculated γ' precipitate radius as a function of time in Haynes 282 at 600 and 750 °C with different ballistic dissolution factor: (a) $f_m = 1.17 \times 10^{17} atoms/cm^2 \times dpa$, (b) $f_m = 8 \times 10^{16} atoms/cm^2 \times dpa$, and (c) $f_m = 1.4 \times 10^{16} atoms/cm^2 \times dpa$. 88
5.8 Calculated Ni_2(Mo, Cr, W) precipitate radius as a function of time in Haynes 244 STD at 600 and 750 °C with different ballistic dissolution factor: (a) $f_m = 1.17 \times 10^{17} atoms/cm^2 \times dpa$, (b) $f_m = 8 \times 10^{16} atoms/cm^2 \times dpa$ and (c) $f_m = 1.4 \times 10^{16} atoms/cm^2 \times dpa$. 90
5.9 Calculated (a) diameters and (b) number density of γ' precipitate as a function of time in Haynes 214 at 600 °C and 750 °C 92
5.10 (a) Diameter, (b) number density of precipitates, and (c) diffusivity of Al solutes in Haynes 214 600 °C, 1 dpa sample, simulated by the modified LSEM model with a time step of 0.001 seconds. 94
5.11 The γ' precipitate diameter as a function of time in Haynes 14 at 600 and 750 °C, simulated by the modified NHM model. 95

A.1 The schematic representation of precipitates from side view. 116
A.2 An example of the size distribution of $Ni_2(Mo, Cr, W)$ 117
A.3 The statistical depth dependence of (a)-(c) precipitate counts and (d)-(f) size distribution of γ' precipitates in irradiated Haynes 282. Subfigures (a) and (d) correspond to the 600 °C, 1 dpa sample; (b) and (e) represent the 750 °C, 1 dpa sample; (c) and (f) depict the 750 °C, 10 dpa sample. 118
A.4 (a) Micrographs showing the evolution of precipitates in aged Haynes 244 under Ni ion irradiation at 600 °C, up to a midrange dose of 10 dpa; (b) and (c) are selected area electron diffraction patterns captured from the region of the irradiated region (at a depth of 1 μm) and pristine region (at 3 μm.) . . 121
A.5 (a)STEM-bright field image and (b) TEM-dark field image of aged Haynes 244 irradiated at 750 °C with a mid-range dose of 1 dpa. (c) and (d) are selected area electron diffraction patterns captured from the region of the irradiated region (at a depth of 1 μm) and pristine region (at 3 μm.) 122
A.6 (a) The selected area electron diffraction pattern of irradiated Haynes 214 (750 °C, 1 dpa); (b) The simulated multi-phase electron diffraction pattern consists of Ni, $\gamma' - Ni_3Al$ and $Cr_{23}C_6$ phases. All separate phases are observed from the [001] zone axis, simulated with SingleCrystal software. 124

Chapter 1

Introduction

Generation IV fission reactors and fusion reactors are expected to bring significant advancements in terms of economics, safety, and reliability compared to existing light and heavy water reactors. Structural materials play a crucial role in maintaining integrity in extreme operating conditions like such as higher operating temperatures above 600°C and higher doses up to hundreds of dpa [11]. Nickel-based superalloys exhibit numerous promising properties that make them attractive for these demanding applications. They possess superior high temperature strength, good high temperature thermal creep resistance, good corrosion resistance and chemical compatibility with molten chloride/fluoride salts and sodium. Some Ni-based alloys are applied in present nuclear systems. Currently, some nickel-based alloys, such as Nimonic alloy PE 16 and Inconel 706, are already employed as fuel cladding materials in European nuclear systems [12]. Furthermore, the extensive non-nuclear industrial use of nickel-based alloys in sectors like aerospace and chemical processing provides a well-established foundation for their fabrication and joining techniques [13].

However, it has been reported that conventional nickel-based alloys experience a significant reduction in tensile ductility and a breakdown in swelling resistance as neutron doses increase, particularly below 650 °C. As the operating temperature rises, high-temperature helium embrittlement emerges as the dominant radiation degradation mechanism, especially in Ni alloys. This phenomenon significantly deteriorates the mechanical properties of structural materials, leading to a reduction in rupture strains and fatigue life cycles.

Consequently, the upper operating temperature of both fission and fusion reactors is constrained by this degradation mechanism.

Ni is a major source of He in thermal reactors due to the large cross section of interacting with thermal neutrons by the two-step reaction $^{58}Ni\,(n_{th},\gamma)^{59}\,Ni\,(n_{th},\alpha)\,^{56}Fe$. Researchers widely believe that the high temperature embrittlement and the transformation of fracture mode from transgranular to intergranular can be attributed to the accumulation of helium at grain boundaries [12]. To address this issue, one of the most promising approaches is to introduce a high number density of nanoscale precipitates uniformly distributed throughout the material matrix. Consequently, the resistance to helium embrittlement is improved. These precipitates act as trapping sites for helium, preventing its migration towards grain boundaries. Moreover, the presence of high-density nano-features not only enhances the creep strength of materials but also facilitates the recombination of point defects. Therefore, both thermal stability under pure thermal conditions and irradiation stability, which occurs far from equilibrium, are critical factors that warrant further investigation [14].

Researchers have turned to ion beam irradiation to expedite the post-irradiation measurement process. Ion beam irradiation can also provide the possibility to systemically control irradiation conditions to explore some single effects [15]. In this paper, 8 MeV Ni^{3+} ions will be utilized to examine the radiation-induced damage and phase instabilities. These ion irradiation experiments serve as an alternative for neutron irradiation, offering valuable insights into the behavior of materials under radiation exposure in a more efficient manner.

Besides, the database of radiation effects on commercial Ni base alloys is relatively limited compared with stainless steels [11, 16]. Therefore, our objective is to expand the scope of investigation by exploring a wide range of novel commercial alloys through screening tests. This approach will allow us to systematically examine the interrelationships among chemical composition, phase stability, microstructure evolution, and mechanical behavior under radiation conditions. By conducting these comprehensive investigations, we aim to gain a deeper understanding of the radiation response of these novel commercial Ni alloys.

Chapter 2

Literature Review

2.1 Nickel-based superalloys as candidates for next-generation fission reactors

Ni alloys have been proposed for various in-core components in Gen IV reactor systems owing to their exceptional properties, like high-temperature strength higher creep strength than austenitic and ferritic–martensitic steels [11, 12]. In European nuclear systems, the successful utilization of Nimonic alloy PE16 and Inconel 706 as fuel cladding further highlights the capabilities of Ni-based alloys. Moreover, these alloys have an extensive non-nuclear industrial base, particularly in aerospace and chemical processing industries, where they are widely employed for fabrication and joining purposes [12]. Given these promising attributes, Ni-based alloys are well-suited for critical reactor components including piping, heat exchangers, and reactor vessel materials.

Notably, nickel-based superalloys emerge as one of the most promising candidates for a range of molten salt reactor (MSR) concepts. MSRs encompass primarily two subclasses: salt-fueled and salt-cooled designs. In salt-fueled MSRs, the fuel is dissolved within the liquid salt. On the other hand, salt-cooled MSRs, such as the Fluoride-Salt-Cooled High-Temperature Reactors (FHR), utilize liquid salt as a coolant instead of water or gas to a Tri-Structural Isotropic (TRISO) particle fuel [17].

Salt-fueled and salt-cooled MSRs have some shared advantages, offering a potentially safer and more efficient form of nuclear power. Large saferty margins due to high boiling points and high volumetric heat capacities of molten salts [17], high operating temperature (up to 750 °C [18, 19, 20]), high fuel utilization, and near atmospheric system pressure [21, 22, 23].

One big difference between salt-fueled MSRs and FHR is radiation resistance. Salt-fueled MSRs suffer from high radiation dose levels from 100 to 200 dpa at the end of their lifetime [24, 25]. In contrast, the reactor vessel of FHRs is designed to experience substantially lower levels of radiation damage, with expected doses typically remaining below 0.1 dpa throughout its operational lifetime [18]. Moreover, structural materials used in salt-fueled and salt-cooled MSRs must meet specific requirements beyond traditional reactors. In addition to the standard mechanical strength demands placed on reactor materials, such as high temperature strength and creep resistance, MSRs necessitate characteristics tailored to their unique operating environments, including moderate oxidation and salt corrosion resistance [24].

It has been reported that Mo, Ni, Nb, Fe, and Cr can approach near-equilibrium with commonly used salts like LiF and UF_4. However, Cr is the most active alloying component among them, corresponding to the free energy of formation of specific compounds [20, 26]. The rapid cracking and material degradation was observed due to the outward dissolution of Cr [27]. Consequently, efforts are directed towards minimizing the Cr content to maintain suitable high-temperature oxidation resistance properties. Therefore, alloy development has focused on high-Mo (for strengthening), low-Cr advanced Ni alloys, exemplified by Hastelloy N [26, 28].

In addition to concerns regarding salt corrosion of structural components, high-dose irradiation damage poses another significant challenge in salt-fueled MSRs. Research into the effects of irradiation on nickel-based alloys reached its zenith during the fast reactor development programs of the 1970s and 1980s [12]. Numerous studies were conducted to investigate the radiation-induced effects, including microstructural changes and mechanical property degradation to ensure the safe and reliable operation of fast reactors.

However, the database of radiation effects on Ni based alloys is relatively limited compared with austenitic and ferritic–martensitic steels [11] and many alloys have little or no associated data [29]. Additionally, Ni exhibits a significant nuclear interaction cross section with thermal neutrons through a two-step reaction $^{58}Ni\,(n_{th},\gamma)^{59}\,Ni\,(n_{th},\alpha)\,^{56}Fe$, resulting in a substantial production of helium. Additionally, the presence of transmutation product tellurium can potentially result in intergranular embrittlement, further restricting the application of this material [30].

According the screening tests, Hastelloy N (Ni-16Mo-7Cr-5Fe-0.05C wt%) shows excellent flexibility and compatibility with different salt systems and presents remarkable corrosion resistance [20]. However, Hastelloy N suffered from high temperature helium embrittlement at the grain boundaries and severe intergranular embrittlement due to the selective diffusion of tellurium [31]. Nb and Ti additions are used to form fine scale MC-type carbides to trap He and Te atoms. However, the modified Hastelloy N is still questionable if the service temperature is above 650 °C due to the carbide coarsening. HN80MTY(Ni-13Mo-7Cr-1Ti-1Al-0.02C wt%) showed even better corrosion resistance than standard Hastelloy at 600 °C while the severe intergrannular cracking occurred at 750 °C [32, 33].

Nowadays, novel commercial Ni-Mo-W-Cr-Al-X alloys are being proposed for new MSR concepts for higher operation temperature (up to 750 °C) [20, 21]. Further research is essential to investigate their high temperature corrosion and radiation resistance, aiming to gain valuable insights into their performance and limitations within extreme environments and ensure their optimal utilization in relevant applications. For the scope of this study, we will exclusively concentrate on investigating the radiation effects on these novel advanced commercial alloys.

2.2 Radiation effects on the microstructure and mechanical properties of Nickel alloys

The US Cladding and Duct Program conducted extensive neutron irradiation experiments on Ni alloys over the range of 450 - 700°C and 10 - 40 dpa during the 1960s and 1970s[11]. Post-irradiation tensile testing revealed a notable decrease in ductility. This decrease was thought to be caused by helium embrittlement, although conclusive evidence from microscopy was scarce or absent [11, 29]. Further investigation included swelling behavior, microstructure evolution of dislocation and voids, radiation-enhanced and radiation-induced changes of precipitates. We will delve into these aspects in this section.

2.2.1 Common mechanical property degradation

2.2.1.1 Tensile property

Nimonic PE16 shows the slight increase in the yield strength but great decrease in total elongation from 40% to 10% tested at 600 °C, with the neutron (E > 0.1 MeV) exposure up to 1.6×10^{20}n/m^2 at around 627 °C [13]. Hastelloy X-280 and Inconel 702 were irradiated by 1 MeV fast neutron at 700°C with the exposure levels between 2.5×10^{19} and 1.2×10^{21} nvt (time-integrated flux of neutron/cm^2) [1]. When examining the ductility of Hastelloy X-280, there was minimal change observed in terms of total elongation during room temperature testing. However, during high temperature tensile testing at 700 °C, the elongation decreased from 48 % to 5 % after 1.2×10^{21} nvt exporsure. On the other hand, significant strength degradation was observed in Inconel 702 during the 700 °C testing. The yield strength decreased from 90,000 psi in the unirradiated condition to 5,000 psi after higher level exposure. Similar reductions in the ultimate strength values were identified as shown in Fig.2.1. The decrease in high-temperature ductility might be attributed to several factors, including intergranular fracture caused by the precipitation of intermetallic compounds and carbides, segregation of impurity elements (such as S and P) induced by radiation, and the stress-driven growth of helium bubbles, along grain boundaries [11].

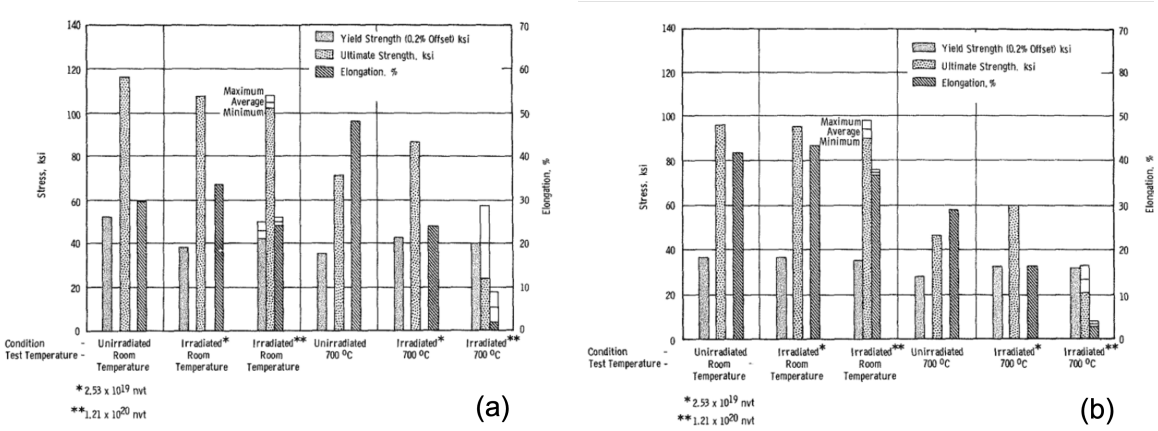


Figure 2.1: Tensile property changes of (a) Hastelloy X-280 and (b) Inconel 702 depending on the test temperature and neutron exposure level [1].

2.2.1.2 Fracture toughness

Inconel 600 and Incoloy 800 were irradiated at temperature around 400-427 °C with the neutron exposure of 2.2×10^{22}n/m^2. Prior to irradiation, the fracture toughness values for Inconel 600 and Incoloy 800 were 575 kJ/m^2 and 605 kJ/m^2, respectively. However, after neutron irradiation, these values decreased significantly to 68 kJ/m^2 and 71 kJ/m^2. This decrease indicates that the irradiated materials became more prone to flaws and exhibited a shift in fracture behavior from homogeneous plastic deformation to a heterogeneous slip and localized channel fracture mechanism, derived from the scanning electron microscopy (SEM) fractographs [34]. Fracture toughness data are scarce for irradiated Ni alloys.

2.2.1.3 Swelling

Ni concentration plays an important role in the suppression of swelling. Ternary alloys consisting of iron, nickel, and 15 % chromium were irradiated in a fast reactor up to 100 dpa at the temperature ranges of 538 °C to 650 °C. The observed swelling was constrained to 5 % within the nickel concentration range of 40-50 wt%. However, for compositions outside this range, once the incubation dose was surpassed, the steady state swelling rates reached 1 % per dpa [35]. The critical dose of swelling breakout is influenced by a multitude of factors, encompassing alloy composition, temperature, microstructure and neutron spectrum [29].

The relationship between temperature and dose may be closely tied to the formation of helium bubbles. Inconel 600 was irradiated in the high flux isotope reactor(HFIR) at 55 - 700 °C, reaching a total dose within 4 to 9 dpa and helium content from 600 to 1800 appm [36]. Within the temperature range of 55 to 600 °C, swelling was found to be relatively unaffected by temperature, remaining at approximately 1 %. However, beyond 600 °C, swelling increased significantly with increasing dose.

The attempts to use cold working as a means to reduce swelling has been proved to be ineffective in Inconel 600 during irradiation with high-helium production rates [36]. It was reported that swelling in solution annealed materials was lower than in aged samples. The remaining minor elements in solution can suppress swelling by interacting with point defects; Subsequent precipitation will reduce this benefit during irradiation [12]. On the other hand, nano-structured precipitates have emerged as a promising approach to enhance resistance against radiation-induced embrittlement and swelling. These precipitates act as effective traps for helium, hydrogen, and undesirable elements, preventing their migration towards grain boundaries. They hinder the coalescence of vacancies by enhancing the mutual annihilation of point defects at the particle-matrix interface, thereby impeding the formation of voids. Consequently, this leads to a higher swelling incubation dose and retarding swelling. However, it is important to note that they can have detrimental effects if the precipitates are large in size but low in density [37, 12].

Solution annealed Hastelloy X and Inconel 625 were irradiated in a fast flux reactor (EBR-II) (E $>$ 0.1 MeV) at the temperature range between 600 and 650 °C with a total dose of 5×10^{22}n/cm^2 [38]. After neutron irradiation, Hastelloy X exhibited significant growth of rod-shaped precipitates, tentatively identified as M_6C. These precipitates had an average length of 700 nm and a thickness of 100 nm. The material also showed a relatively low void number density of approximately 10^{12}/cm^3 with an average void size of around 300 nm, leading to 2 % swelling. The relatively large and sparsely distributed isolated carbides worked as efficient sinks and nucleation points, favorable for facilitating rapid helium-stabilized cavity growth.

In contrast, Inconel 625 exhibited a different response, as no voids and only a few dislocations were observed. Instead, a high number density of finely dispersed, disk-shaped semi-coherent precipitates was present. These precipitates were tentatively identified as

Ni_3Nb, with diameters ranging from 100 to 200 nm and thicknesses of approximately 10 to 20 nm [38]. Similar effective suppression of swelling has also been observed in other alloys such as Nimonic PE-16 and Inconel X-750. These alloys have a homogeneous distribution of nano-scaled intragranular precipitates known as γ', specifically Ni_3(Al,Ti) precipitates [29, 39]. It is believed that the interface between the closely spaced, coherent precipitates and the matrix played a role in enhancing the mutual annihilation of point defects, leading to the absence of void formation.

Furthermore, Williams et al. conducted three distinct heat treatments on PE-16 in order to induce various sizes of precipitates. Subsequently, electron irradiation at 1 MeV was performed within a temperature range of 500 to 650 °C using a high voltage electron microscope [2]. In the condition where the particles had an average diameter of approximately 20 nm, the swelling rate demonstrated the least magnitude when compared to precipitates larger than 70 nm or smaller than 3 nm, as depicted in Fig.2.2. One proposed mechanism suggests that the optimal condition for effective point defect trapping lies within an intermediate particle size range, where dislocation pinning is strongest. Conversely, an alternative mechanism proposes that smaller particle sizes, which correspond to higher precipitate-matrix interface areas at the same volume fraction, exhibit greater defect-trapping capabilities [12]. More relevant investigation is needed to gain a comprehensive understanding.

2.2.1.4 Radiation induced segregation

Radiation-induced segregation (RIS) is often observed in alloys where different elements have different diffusion properties and associated atomistic sizes. Radiation generates abundant point defects which are far away from equilibrium states. These defects can migrate towards low-energy locations or preferentially towards certain types of solute atoms at high temperature, leading to enrichment or depletion of such elements at grain boundaries. The segregation of elements due to radiation can have significant implications for the properties and performance of materials. The segregation of impurity solutes, like sulphur(S), phosphorus(P),and silicon(Si), and the formation of secondary phases, like continuous films

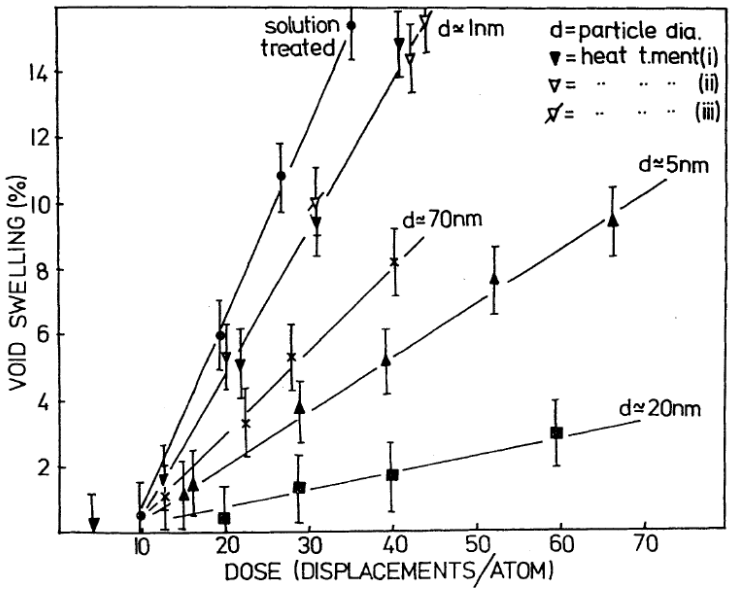


Figure 2.2: Dose dependence of void swelling at several particle sizes. The irradiation condition was 10^{-2} dpa/s and 600°C [2].

of gamma-prime $Ni_3(Al,Ti)$, which will greatly embrittle the grain boundaries and reduce the strength of particle-matrix interfaces, leading to lower ductility [11, 13, 40].

2.2.2 Precipitate stability under irradiation

The attributes of second-phase particles, including size, density, morphology, and composition, play a crucial role in achieving the desired mechanical properties of materials. Notably, the distribution of these second-phase particles and their stability under irradiation conditions significantly influence the suppression of void swelling at low to intermediate temperatures, as well as the alleviation of high temperature helium embrittlement. The high number density small precipitates function as effective sinks, facilitating the mutual recombination of point defects, and serve as traps for helium atoms at the interface between the particles and the matrix, preventing the migration of helium atoms towards grain boundaries. However, when these precipitates grow excessively in size, they can facilitate nucleation for gas-stabilized cavities and the precipitate-cavity pair will undergo synchronized growth. Furthermore, radiation-induced segregation of minor elements, such as C and Si,and formation of carbides or intermetallic might aggregate void swelling, since these elements tend

to hinder swelling when they are maintained in solution within the matrix[11]. Thus, it is crucial to investigate phase instabilities under irradiation conditions.

2.2.2.1 Theoretical background

The understanding of thermodynamic and kinetic models of precipitation in metals under thermal activation conditions has undergone extensive research for many decades. In such conditions, the stability of precipitates is determined by two critical factors: the diffusion rate of solute atoms to the precipitate, and the dissolution rate where atoms are thermally activated and subsequently released from the precipitate surface [11]. Exploring phase stability in precipitates and phase transformations under extreme, far-from-equilibrium conditions, such as irradiation, demands further investigation and development. Irradiation induces a disturbance in the equilibrium state, giving rise to competing effects: radiation-enhanced dissolution on precipitates versus radiation-enhanced precipitation/Ostwald ripening within the matrix. Other phase instabilities, like vacancy-induced dissolution, radiation-induced precipitation, and radiation-modified precipitation [41] are not described in detail in this study.

2.2.2.1.1 Radiation-induced dissolution The high-energy particles cause atoms in the material to be displaced from their initial positions during energy transfer. These recoiled atoms are continuously generated during collision cascades. As a result, atoms from the surface of precipitates can be recoiled into the surrounding matrix, leading to ballistic dissolution. In the case of precipitates with long-range ordering, the original order of atomic arrangement is disrupted by neutron and ion beam mixing. Within these precipitates, disordered regions have the potential to re-order during diffusion. Meanwhile, the high concentration of solute atoms in the disordered areas near the precipitate surface will diffuse into the matrix, resulting in disordering dissolution [5].

2.2.2.1.2 Radiation-enhanced diffusion Irradiation can create a much higher concentration of interstitials and vacancies at intermediate temperatures. For example, at 600 °C, the steady-state vacancy concentration produced by 0.001 dpa/s irradiation was

approximately seven orders of magnitude higher than the thermally activated vacancy concentration in pure Haynes 282. The diffusion rate under irradiationD_{red} can be written as,

$$D_{red} = f_v D_v C_v + f_i D_i C_i \tag{2.1}$$

where D_v, D_i and C_v, C_i are the self-diffusion coefficients and concentrations of vacancies and interstitials, respectively. f_v and f_i are corresponding correlation factors ($f_v = f_i = 1$ in Was's book[3], while $f_v = 0.78, f_i = 0.44$ is used in Chen's simulation [42]). The point defect balance equations, which follow standard kinetic rate theory, vary across different temperature ranges. Fig.2.3 illustrates the overall trend of the diffusion rate. This study focuses on the intermediate temperature ranges where both dose rate and temperature play significant roles, as well as the high-temperature range where thermal equilibrium vacancy predominates. A more detailed investigation will be discussed in the later session.

2.2.2.2 Experimental background

γ' precipitates are the primary strengthening source in many commercial Nickel-based superalloys. Thus, in this part, we briefly summarize the relevant studies about the γ' phase stability as an example.

It was reported that pre-existing γ' precipitates in PE 16 underwent redistribution towards sinks, such as dislocation network, leading to the formation of a skeletal structure of γ' under fast neutron irradiation in EBR-II, at temperatures ranging from 513 to 636 °C, as shown in Fig.2.4 [39]. Comparable findings of initial γ' precipitates redistribution were observed in Ni-Al alloys when exposed to irradiation with Ni ions, at 550 °C with a dose rate of 10^{-2} dpa/s [5]. Large pre-existing γ' (25 nm) dissolved, and new γ' precipitates nucleated on a very fine scale, ultimately reaching uniform size across all precipitates as illustrated in Fig. 2.5. In Fe-Cr-Ni alloys, γ' precipitates also exhibited notable stability at 593 °C under fast neutron irradiation up to 1.7×10^{22}neutrons/cm^2, while a propensity for cellular-shaped precipitate transformation spherical shape emerged under 3 MeV Ni ion irradiation at 0.005 dpa/s.

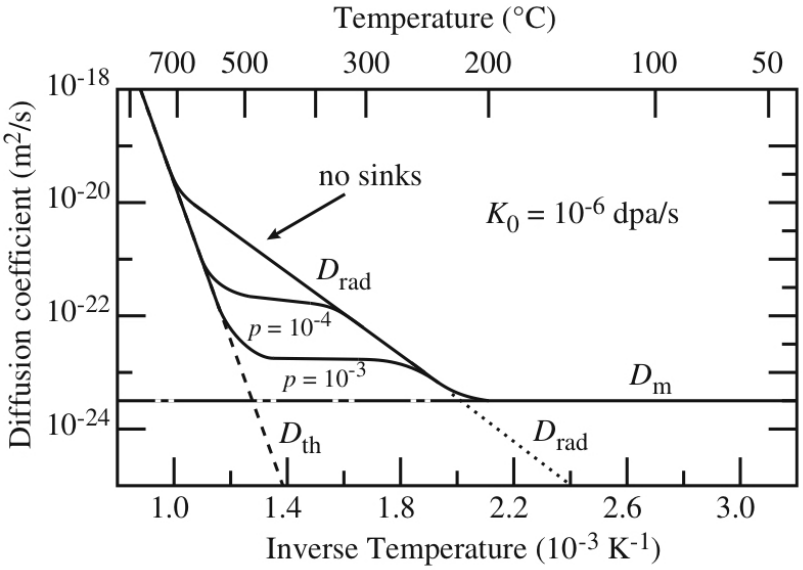


Figure 2.3: Diffusion coefficients as a function of 1/T for a nickel-based alloy during irradiation at a displacement rate of 10^{-6} dpa/s. D_{rad} is the radiation enhanced diffusion coefficient calculated from rate theory equations for various sink annihilation probabilities, p. D_m and D_{th} are diffusion coefficients from radiation mixing and thermal diffusion, respectively [3].

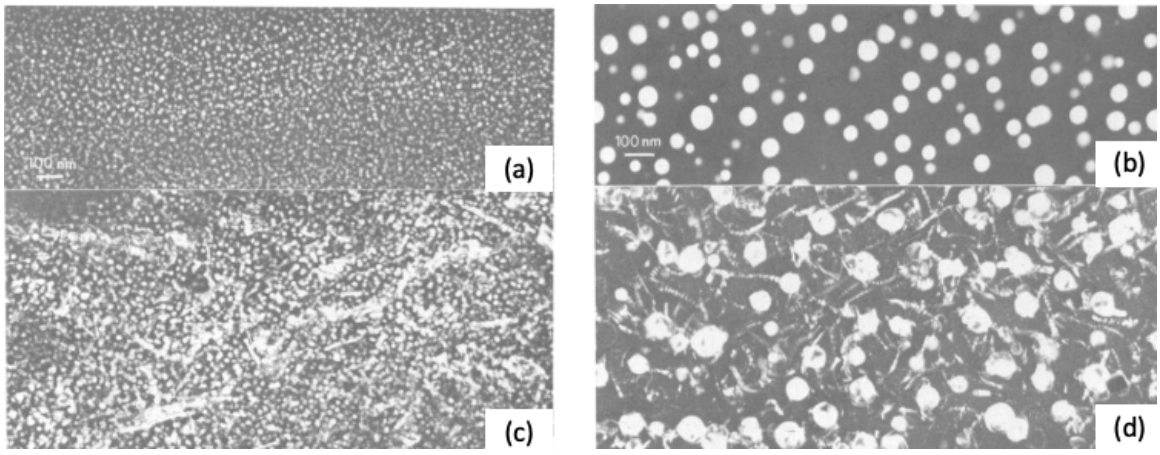


Figure 2.4: The γ' precipitate evolution in aged PE16(a, c) and overaged PE16(b, d) during neutron irradiation at 600°C. (a) and (b) presented the initial precipitate distribution before irradiation; (c) and (d) depicted the precipitates morphology after irradiation to the total dose of $5.4 \times 10^{22} n/cm^2$. Reproduced from Ref.[4].

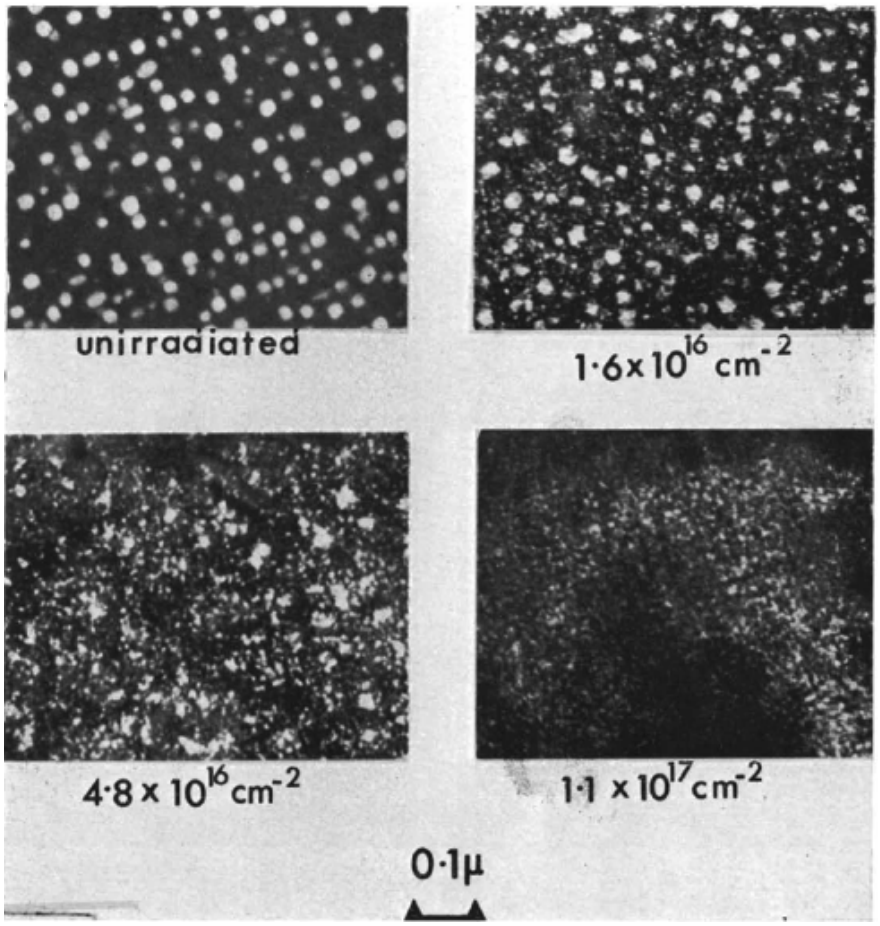


Figure 2.5: The change in γ' precipitate size and density in Ni-Al alloy as a function of size. The sample was irradiated by charge particles with the dose rate of 10^{-2} dpa/s at 550°C [5].

Thus, the phase stability under irradiation is closely related to the historical heat treatment, the dose rate, the chemical composition of the matrix, the Ti/Al ratio of precipitates, precipitate size, and the degree of coherency of precipitates, other sinks (like intrinsic dislocation lines), irradiation conditions, and needs more investigation [5, 43, 44, 45, 46].

2.3 Ion-irradiation alternative to neutron irradiation

To facilitate the development of materials for next-generation fission and fusion reactors, the most optimal and direct approach is to investigate neutron irradiation damage on candidate materials either in test reactors or real reactors in operation. However, the dose rate within these reactors is exceedingly low (10^{-7} dpa/s), potentially requiring several decades to reach the desired dose. Additionally, the materials become activated through nuclear reactions, resulting in inevitable high radioactivity. It is quite time-consuming to wait for a long decay period until the neutron-irradiated materials can be characterized. Moreover, the limited availability of facilities capable of handling activated samples, and the high costs associated with such experiments, have prompted researchers to seek more efficient approaches to studying irradiation effects.

Charged particle irradiation has been widely utilized as an alternative to neutron irradiation for several decades. It can significantly accelerate the process because of its high dose rate range of $10^{-4} - 10^{-3}$ dpa/s and the absence of radioactive production [47]. This technique also offers unique capabilities, like allowing careful and systematic control of irradiation conditions to explore fundamental specific single-effects [15]. However, there are still several limitations and differences between ion and neutron irradiation. Charged particles have limited penetration depth, resulting in a restricted volume for post-irradiation characterization, particularly in mechanical testing. Gradient damage level with depth further complicates the extraction of bulk property information.

Moreover, the analysis region for 'safe' radiation assessment, where ion irradiation-induced artifacts are minimal, is constrained by near-surface and injected ion phenomena, as depicted in Fig.2.6. Near the surface, the concentration of vacancies and interstitials is much

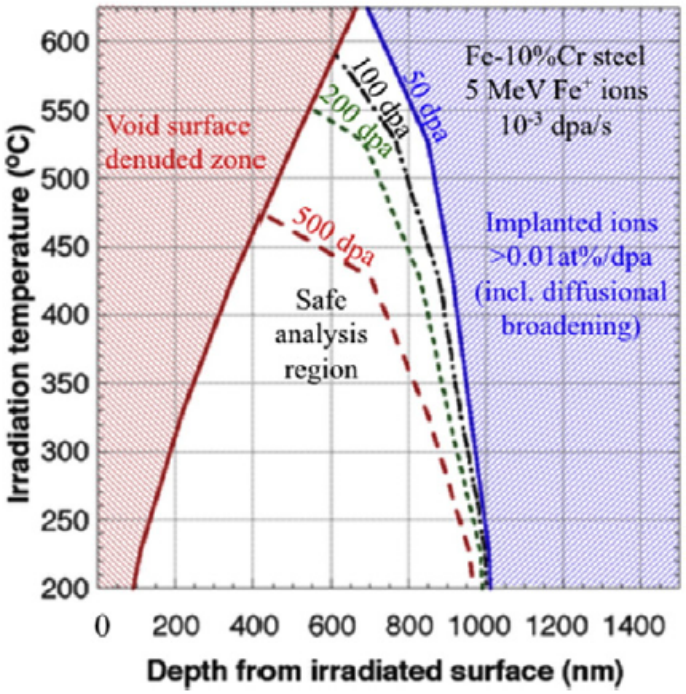


Figure 2.6: Calculated temperature- and depth-dependent regions affected by the free surface and injected ions for Fe-10%Cr steel irradiated with 5 MeV Fe^{+} ions at 10^{-3} dpa/s to dose levels of 50-500 dpa. [15]

lower compared to the intermediate range. Free surfaces (including grain boundaries) acts as effective sinks for point defects, altering the local microstructural evolution and leading to regions depleted of dislocation loops and voids [48]. Injected ions play a significant role in suppressing precipitation during irradiation [6]. In Fe-15 at.% Cr alloys irradiated with 2 MeV Fe^{2+} ions irradiated at 300 °C the depth dependence of α' is closely associated with the concentration of injected Fe ions rather than the damage level, as illustrated in Fig.2.7. The bombarding ions are deposited near the region of peak displacement damage, resulting in a localized surplus of interstitial atoms and the formation of high-density interstitial clusters. This disrupts the balance of vacancy supersaturation, leading to increased vacancy annihilation through enhanced recombination. Consequently, fewer vacancies are available to interact with essential elements, which retards the diffusion process and the formation of precipitates [15, 6]. Moreover, when the atomic fraction of implanted ions exceeds 5×10^{-5} and 10^{-3}, it is likely to suppress void swelling at high temperature and promote amorphization at low temperature, respectively [49]. During high-temperature

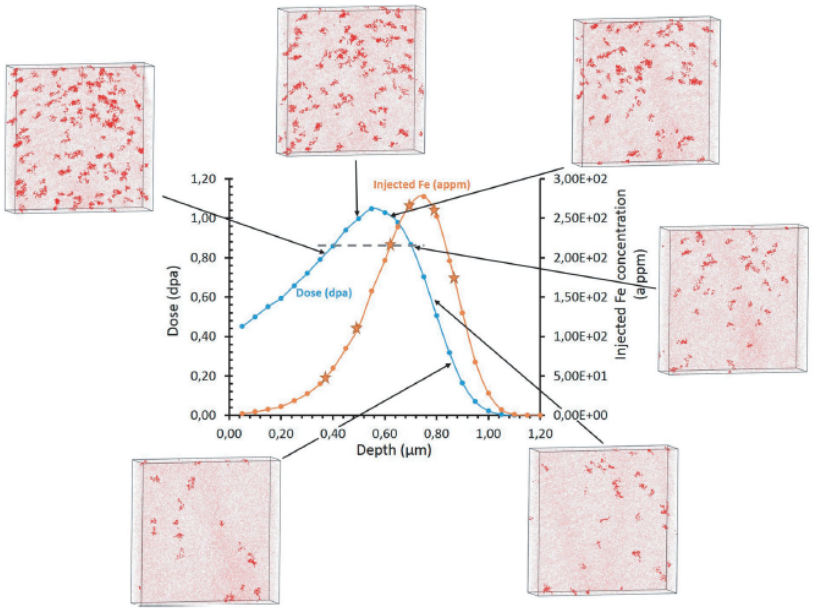


Figure 2.7: Damage and implantation profiles of Fe-15 at.% Cr alloys irradiated with 2 MeV Fe^{2+} ions irradiated at 300°C calculated with SRIM 2013 and the 3D distribution of Cr atoms observed using APT at different depths [6].

irradiation, radiation-enhanced diffusion, along with thermal diffusion, can significantly broaden the profile of implanted ions and further reduce the mid-range safe radiation analysis region [50, 51]. Therefore, it is crucial to comprehend these artifacts, establish meticulous experimental designs, and exercise caution when interpreting data.

Chapter 3

Materials and Methods

3.1 Materials and sample preparation

All commercial nickel-based superalloys used in this study were provided by Dr. Vijay Vasudevan from the University of North Texas, USA. HAYNES ® alloys are designed for high-temperature applications, such as aircraft gas turbine engines [52]. The nominal composition and thermomechanical heat treatment conditions of each alloy is listed in Table. 3.1 in unit of weight percentage and Table. 3.2, respectively. We will briefly introduce promising properties and microstructures before irradiation for each sample separately.

- **Haynes 282**

  Haynes® 282® was provided in the solution-annealed condition, with the typical solution-annealing temperature range falling between 1121 and 1149 °C, which contained a moderate density of heterogeneous dislocation lines with the dislocation density of $(8.8 \pm 1.8) \times 10^{13}/m^2$. The standard two-step aging process involves 1010 °C / 2 hours/ air cooling and 788 °C / 8 hours / air cooling, subsequently performed at the University of Tennessee, Knoxville (UTK). The intrinsic dislocation line density decreased to $(1.2 \pm 0.3) \times 10^{13}/m^2$ after the standard two-step aging process, and the remaining dislocation lines primarily accumulated at the sample surface due to mechanical polishing. Some Cr-enriched precipitates are sporadically dispersed throughout the matrix in both the annealed solution sample and the aged sample.

Table 3.1: Nominal composition of Ni-based superalloys in weight percentage(wt%)

Alloy	Ni	Cr	Mo	W	Al	Fe	Co	C	Mg	Si	B	Other
Haynes 244	71 bal	8.0	22.5	6.0	0.5*	2*	/	0.03*	0.8*	/	/	/
Haynes 214	75 bal	16.0	0.5*	0.5*	4.5	3.0	2*	0.04	0.5*	0.2*	0.01*	Ti 0.5*, Zr 0.1*, Nb 0,15*
Haynes 282	57 bal	20.0	8.5	/	1.5	/	10.0	0.06	0.3*	0.15*	0.005	Ti 2.1
Hastelloy C-276	57 bal	16.0	16.0	4.0	/	5.0	2.5*	0.01*	1*	0.08*	/	Co 0.5*, V 0.35*

Table 3.2: Heat treatment conditions of Nickel based superalloys before irradiation

	Heat treatment condition
Aged Haynes 244 (STD)	As-received plate (AR) + 760 °C/ 16 hours/ furnace cooling (FC) + 650 °C/ 32 hours/ air cooling (AC)
Solutionized Haynes 244 (SHT)	AR + 1150 °C/ 24 hours/ slow cooling
Haynes 214	AR + 1095 °C/ 0.5 hour/ water quenching
Aged Haynes 282	AR + 1010 °C/ 2 hours/ AC + 788 °C/ 8 hours/ AC
Hastelloy C-276	As-received plate

Haynes 282 demonstrates a remarkable combination of superior creep strength (649 °C - 923 °C), thermal stability, weldability, and fabricability [53]. The primary source of strength enhancement is the gamma prime phase $\gamma' - Ni_3(Al,Ti)$ with the $L1_2$ ordered crystal structure, which is coherent with the γ-disordered matrix. The γ' precipitates uniformly distributed within the matrix in the aged sample. The initial average precipitate diameter of γ' precipitates was 29 ± 5 nm with the number density of $(5 \pm 1) \times 10^{21}/\text{m}^3$. The calculated volume fraction was about 7%. The measured Vickers hardness values (0.5 kg load) for solid solution annealed and aged unirradiated Haynes 282 were 2.5 ± 0.2 GPa and 3.7 ± 0.2 GPa, respectively.

- **Haynes 244**

  Haynes® 244 ® alloys were provided in the solution-annealed condition (1150 °C / 1 hour/ air cooling). For the solutionized sample (SHT), an additional solution annealing treatment was carried out at 1150 °C for another 24 hours with a slow cooling rate to avoid precipitation by reducing vacancy concentration. For the 244 aged sample (STD), the sample was held at 1150 °C for 1 hour followed by two-step standard aging, including 760 °C/ 16 hours/ furnace cooling and 650 °C/ 32 hours/ air cooling. These heat treatments were performed at the University of North Texas. The intrinsic dislocation density was $(4.3 \pm 4.0) \times 10^{12}/m^2$ and $(3.3 \pm 0.8) \times 10^{14}/m^2$ for SHT and STD samples, respectively. The measured Vickers hardness values (0.5 kg load) were 4.76 ± 0.10 GPa and 1.92 ± 0.06 GPa for the Haynes 244 STD and SHT, respectively.

  Haynes 244 offers an extended operating temperature range of up to 760 °C, coupled with low thermal expansion and excellent low-cycle fatigue resistance, along with good oxidation resistance [16, 52]. The primary strengthening phase in Haynes 244 alloys is Ni_2(Mo, Cr, W), which is a long-range-ordered metastable phase with a Pt_2Mo-type orthorhombic crystal structure, coherent with the γ-disordered matrix [7]. It has been reported that Ni_2(Mo, Cr, W) precipitates form in Haynes 242 (Ni-25Mo-8Cr wt%) during isothermal aging between 550 °C and 750 °C. However, no precipitation or significant hardening occurs at 775 °C, suggesting that this temperature may represent the critical transformation point from short-range to long-range ordering [54]. Two

ordering mechanisms occur at different ranges: Continuous ordering works below 700 °C, while the first order nucleation and growth mechanism dominates above 700 °C [54, 55].

The lattice parameter of Ni_2(Mo, Cr, W) can be estimated as $a_p = 1.5\sqrt{2}a_M, b_p = 0.5\sqrt{2}a_M, c_p = a_M$, where the subscripts p and M refer to precipitate and matrix, respectively. The schematic crystallographic relationship between the coherent precipitate and disordered FCC matrix is shown in Fig. 3.1(a). Under typical thermal aging conditions, six variants can form randomly. The c-axis of the orthorhombic unit cell can align with any of the three a-axes of the disordered FCC unit cell, while the a and b axes align along the corresponding ⟨110⟩ directions, leading to the different orientational variants as plotted in Fig. 3.1(b). Since the precipitate is either ellipsoid or disk-shaped, we use the aligned thin-plate model. The long axis shows the thin-plate diameter and the short axis shows the thin-plate thickness.

However, getting the accurate size and number density is a great challenge. It should be noted that due to the limited thickness of the foil, some of large precipitates are truncated in images. As a result, the projected or measured length of these truncated precipitates is smaller than their true diameter. This truncation effect can lead to a higher number density of precipitates, and consequently, the histograms of measured particle sizes may exhibit a bias towards smaller sizes. This effect was discussed in the

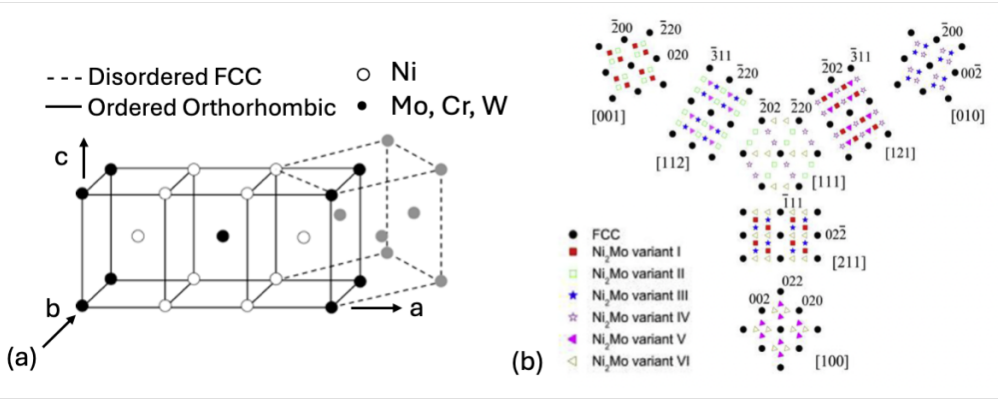


Figure 3.1: (a) Schematic of the unit cell for the Pt_2Mo-type structure within an FCC matrix; (b) Schematic electron diffraction patterns of the FCC matrix, showing six different orientation variants along various FCC matrix zone axes [7].

Appendix A.1. The uncorrected and corrected average diameters were 77.4 and 71.1 nm, respectively. The difference between these values was relatively small compared to the standard deviation, suggesting that the correction to the remaining samples may not be necessary. Overall, the average diameter of precipitates in the unirradiated sample was approximately 73.8 ± 31.2 nm, and the average thickness was about 20.1 ± 6.1 nm. It is even more tricky to estimate the number density, as only two variants are visible along the [001] zone axis in the dark-field TEM images (see Fig. 3.1(b)). A common approach is multiplying the observed number density by three, assuming that six variants are equivalent and randomly distributed on the macro-scale. However, our later analysis suggests a competitive relationship between the variants, indicating that this assumption may not hold in all cases. Therefore, a more accurate method for estimating the number density may be required rather than simply applying a factor of three across all cases. We will revisit this issue after thoroughly reviewing all data related to Ni_2(Mo, Cr, W) precipitates.

- **Haynes 214**

  Haynes® 214 ® alloy was provided in the solution-annealed condition. Since we observed that the surface hardness was not uniform, we performed the solution-annealing treatment at 1095 °C for half an hour with water quenching at UTK. No precipitation or elemental segregation around the dislocation lines were observed before irradiation. The dislocation density was about $(1.5 \pm 1.7) \times 10^{13}/m^2$. The Vickers hardness values (measured with a 0.5 kg load) for Haynes 214 were found to be 1.73 ± 0.08 GPa.

  Solutionized Haynes 214 exhibits unparalleled oxidation resistance at very high operating temperature ($\geq$ 950 °C) [52]. $\gamma' - Ni_3Al$ grows rapidly in the intermediate temperature range of 595 °C to 925 °C, which is not recommended due to the probability of strain-age cracking [52]. This sample is part of a screening test to evaluate the performance of γ' precipitates in Ni alloys under irradiation

- **Hastelloy C-276**

Hastelloy® C-276® alloy was provided in the solution-annealed condition, with the initial dislocation line density of $(1.5 \pm 0.5) \times 10^{13}/m^2$. Renowned for its exceptional corrosion resistance across a wide range of severe environments, this alloy is highly suitable for numerous chemical process applications [56] and serves as one of the main candidates for the component of supercritical-water-cooled reactor [57].

- **Haynes 230**

  Haynes 230 is a solid solution strengthened superalloy, decorated with MC, M_6C and M_23C_6. Decomposition of primary carbides would occur between 650 °C and 900 °C after long-term thermal exposure [58]. This sample was irradiated, but since the main strengthening phases are carbides, not intermetallics. This sample is excluded in this dissertation and can be explored to compare the carbides and intermetallic secondary phase stability in future research.

3.2 Methods

3.2.1 Ion irradiation

Before irradiation, the front and back sides of all samples underwent sandpaper grounding up to 1500 grits to achieve a flat surface. Subsequently, the front side was polished using diamond suspension, gradually reducing the surface roughness to 0.5 μm, and finally finished with 0.05 μm colloidal silica to attain a mirror surface. The samples were attached to the Ni-base plate with the high vacuum-compatible silver paste and cured for 2 hours. Samples were plasma cleaned for 2 hours in the chamber one night before irradiation.

Ion irradiation was performed at the Michigan Ion Beam Laboratory with a 3 MeV tandem accelerator. Each sample has the dimension of $2 \times 3 \times 1$ mm^3. Fig.3.2 shows the mounted sample configuration. The irradiation matrix receives a total of 4 irradiation exposures with 8 MeV Ni^{3+} broad ion beam up to 1 and 10 dpa with a dose rate of 0.001 dpa/s at 600 °C and 750 °C. Table.3.3 presents all the irradiation conditions. The heating period and irradiation timeline is listed in Fig. 3.3. Four thermocouples were attached to the sample plate, and one infrared camera was also used to monitor the temperature of

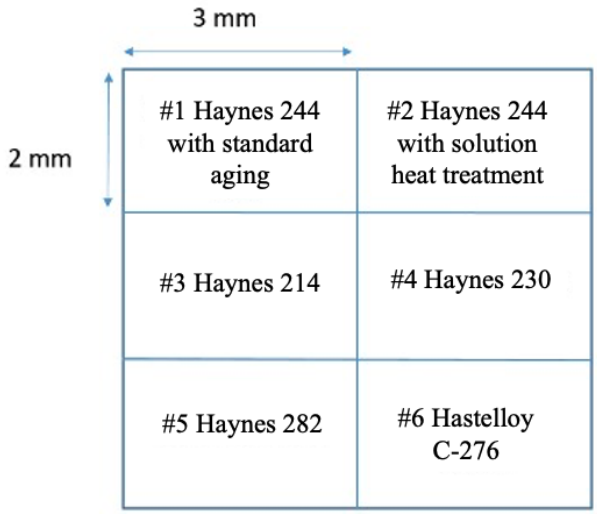


Figure 3.2: The mounted sample configuration consists of six samples. The defocused beam fully covered all samples.

Table 3.3: Irradiation matrix of the Ni-based superalloys

Ions	Midrange Dose (dpa)	Fluence (ions/cm^2)	Flux (ions/cm^{2}s)	Temperature (K)
8 MeV Ni^{3+}	1	2E15	2E12	600 °C
	10	2E16		600 °C
	1	2E15		750 °C
	10	2E16		750 °C

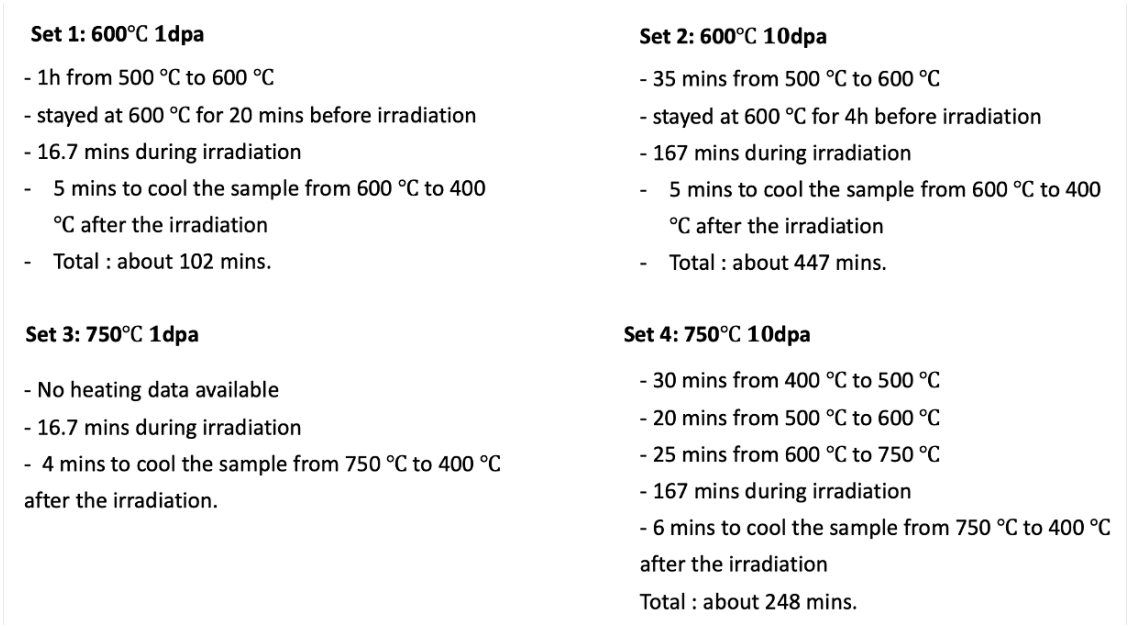


Figure 3.3: Detailed duration at each temperature. Heating and cooling rates are not available.

the specimen during irradiation. The temperature variation was within 10 °C of the design values.

In this study, SRIM 2013 was used to determine the fluences required to achieve the desired damage levels. The damage profile was calculated using the 'Full-Cascades' mode with 10000 iterations, employing the damage energy method [59]. For Nickel (Ni), the effective displacement threshold was determined to be 40 eV [60]. It was observed that the measured implanted Ni profile deviated by approximately 700 nm towards the surface of 8 MeV Ni ions in pure Fe. This shift was attributed to the overestimation of the stopping power of Ni as implemented in SRIM 2013 [61]. To address this discrepancy, we applied a correction factor to modify the predicted ion profile in SRIM. In our investigation, we chose a correction factor 1.5 for this purpose as suggested in Ref.[61]. Fig. 3.4 shows the SRIM calculated damage profile for the Ni alloys. The desired dose was 1 dpa and 10 dpa at a mid-range depth of 1 μm from the surface.

3.2.2 Nanoindentation

Hardness testing is a valuable technique used to evaluate the increase in hardness and estimate the yield strength based on empirical correlations associated with radiation

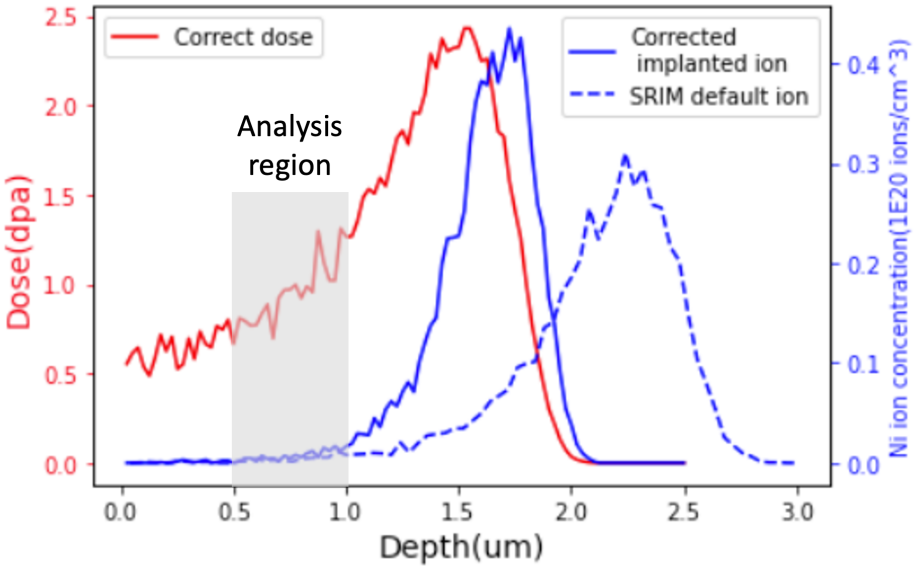


Figure 3.4: SRIM estimated profiles of 8 MeV Ni ion with fluence of 2×10^{15} ions/nm^2 in Ni target. The correction factor is 1.5.

embrittlement at low temperatures and helium embrittlement at high temperatures. The presence of radiation-induced defects, such as dislocations, precipitates and helium bubbles, serves as obstacles that impede the dislocation movement, resulting in an increased yield stress and reduced ductility [62]. Hardness is calculated by a simple equation:

$$H = P/A \tag{3.1}$$

where P refers to the peak load, A is the projected area of the indentation impression, which is equal to the maximal contact area.

Nanoindentation provides an efficient method for measuring the hardness of irradiated samples due to its small sampling volume requirement. However, there are four inevitable effects that occur in nanoindentation of heavy ion irradiated samples:(1) indentation size effect(ISE) where the hardness decreases with the increasing indentation depth; (2) pileup effect which is pronounced in relatively soft materials with the high ratio of elastic modulus and yield strength (E/σ_y)and low work hardening capacity [63]; (3) damage gradient effect(DGE) due to the heterogeneous damage profile of heavy ion irradiation; (4) soft substrate effect (SSE) due to the shallow irradiation depth of heavy ions. The first two is common phenomenon in all nanoindentation testing while the other two artifacts often occurs in ion irradiated or film/substrate materials.

Nix-Gao model is widely applied to correct the ISE and extract the estimated bulk-equivalent hardness H_0 [64].

$$\frac{H}{H_0} = \sqrt{1 + \frac{h^*}{h}} \tag{3.2}$$

where H is the measured hardness, H_0 is the hardness in the infinite depth, h is the indentation depth and h^* is the characteristic length dependent on the given material and the indenter geometry. Notably, the plastic zone within irradiated materials extends 5-10 times beyond the actual indent, implying that a wide dose range is sampled even with a shallow indentation [65]. To address this, Kasada et al. [8] employed a film/substrate model to estimate the 'true' hardness of the irradiated region alone. They achieved this by plotting a bilinear curve of H^2 vs. $1/h$ as shown in Fig.3.5. In this paper, the depth of irradiation

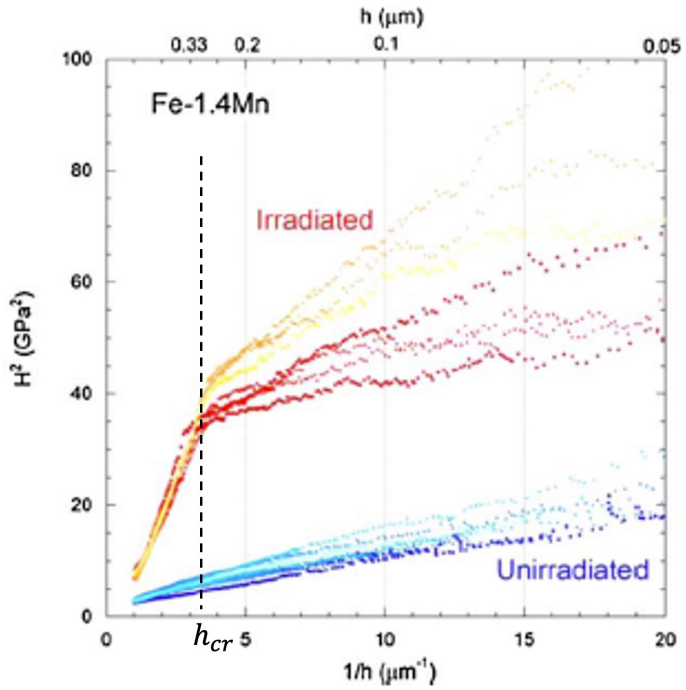


Figure 3.5: Example of bi-linear fitting: Plot of H^2 versus $1/h$ for Fe-1.4Mn before and after 6.4 MeV Fe^{3+} ion irradiation at 290 °C [8]

layer is about 2 μm, corresponding to the available region for estimating H_0^{irr} is from 200 nm to 400 nm.

In this study, the nanoindentation testing was performed at room temperature with a KLA nano-indenter with a Berkovich tip at IAMM. Before testing, indenter tip calibration was performed on a fused silica sample using the Oliver-Pharr method [66]. The indentation direction was vertical to the sample irradiated surface. The continuous stiffness measurement (CSM) was carried out with 0.05/s strain rate and 2 nm oscillation at 45 Hz. Twenty-five indents were performed as at least a 5 x 5 square matrix pattern for each sample, including irradiated and unirradiated Ni-based superalloys, to get the average depth profile of hardness with a peaking loading penetration depth of 1000 nm. The distance between adjacent indents was set as 40 μm to avoid the interference from adjacent indents. All nanoindentation data obtained below 100 nm were excluded due to unsolvable indentation size effects [67] and reverse indentation size effects [8].

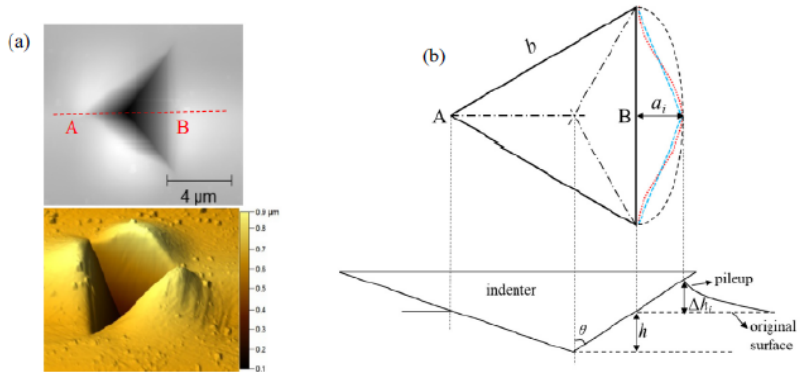


Figure 3.6: (a) The AFM image of a 1000 nm indent of 300 h aged Fe18Cr [9]. (b) The schematic diagram of the indent and the cross section. the semi ellipse with short axis a_i refers to the estimated contact periphery of the indenter with material [10]. The red dotted line shows the sinusoidal approximation of the pileup periphery. The blue dashed line shows the pileup shape with an equivalent area to the sinusoidal shape [9].

3.2.3 Atomic force microscopy

Atomic force microscopy (AFM) Cypher AFM at IAMM was employed to examine the three-dimensional topography of a sample surface with high resolution at the nanoscale level. The air topography technique was chosen to scan an area measuring 20 μm x 20 μm around the indents, using a scanning rate of 1 Hz and capturing 128 lines per figure. To enhance accuracy and minimize surrounding noises and artifacts, a mask-applied histogram method was implemented before recording the pileup height on each side of the residual indents. This measurement was crucial for correcting the contact area of the indentation impression A_c, as shown in Fig. 3.6(a) and expressed in Equ.3.3. The more accurate hardness can be obtained by this pileup correction.

$$A_c = A + 1.65\sqrt{A}\sum \Delta h_i \tag{3.3}$$

where Δh_i is the peak pileup height measured from each side of the indent.

3.2.4 Atom probe tomography

Atom Probe Tomography (APT) enables high-resolution three-dimensional maps depicting the distribution of atoms in the sample from two-dimensional histograms through data

reconstruction. Additionally, this technique provides precise and accurate quantitative measurements of elemental concentrations within nanoscale region of materials. By harnessing the power of APT, scientists can delve into the intricate atomic structures of materials, unlocking valuable insights for various scientific and engineering applications.

APT specimens were prepared by a standard lift-out process with a Ga beam in the FEI Nova 200 dual-beam scanning electron microscope at the Center for Nanophase Materials Sciences (CNMS) of the Oak Ridge National Laboratory (ORNL). Two specific detection depths were chosen: (1) a depth of 500 nm and (2) a depth of 3000 nm below the platinum protection layer. These depths were targeted to investigate the mid-range irradiated and pristine regions, respectively. Samples were analyzed using a LEAP 4000X HR model APT. The temperature was carefully cooled to 31.5 K to avoid evaporation between pulses and reduce noises. The evaporation of tips was laser pulsed with an energy range of 50-60 pJ and a pulse repetition rate of 200 kHz. The rate was set between 0.005 and 0.01 atoms per pulse for detection purposes.

The data reconstruction was operated by the Integrated Visualization and Analysis Software(IVAS) 3.8.16. Each detection depth was probed utilizing one to two tips, each containing approximately 8 to 17 million atoms. Other vital parameters were the image compression factor(1.65) and the detector efficiency of the atom probe (0.36) for this study. The determination of elements relies on their respective mass-to-charge ratios, expressed in units of Dalton (Da). When two isotopes share an identical mass-to-charge ratio, it becomes unfeasible to differentiate the individual contributions of these isotopes within a single peak on the mass spectrum. This occurrence is called isotope peak overlapping, which always leads to imprecise chemical composition measurements. For example, in Haynes 214, Cr atoms exhibit isotopes with mass values of 50, 52, 53, and 54 atomic mass units (amu), whereas Fe atoms have isotopes with masses of 54, 56, 57, and 58 amu. On the other hand, aluminum (Al) atoms possess only a single isotope with a mass of 27 amu. Both Fe and Cr atoms are likely to be detected at a charge state of 2+, resulting in a peak overlap occurring at 27 Da when mixed with aluminum (Al) in the analysis.

A correction factor based on the natural abundance of each isotope is introduced for precise quantification of chemical composition. If the peak at 27 Da was initially assigned

to Al, the correction factors for Cr and Fe can be calculated as follows,

$$F_{Cr} = \frac{A_{\mathrm{Cr50}} + A_{\mathrm{Cr52}} + A_{\mathrm{Cr53}} + A_{Cr54}}{A_{Cr50} + A_{Cr52} + A_{Cr53}} = 1.024 \tag{3.4}$$

$$F_{Fe} = \frac{A_{\mathrm{Fe54}} + A_{\mathrm{Fe56}} + A_{\mathrm{Fe57}} + A_{Fe58}}{A_{Fe56} + A_{Fe57} + A_{Fe58}} = 1.062 \tag{3.5}$$

where A represents the natural abundance of each isotope, denoted by the atom name and mass in subscripts. The corrected concentrations of Cr, Fe, and Al are calculated with:

$$C_{Cr-c} = C_{Cr-uc} \times F_{Cr} \tag{3.6}$$

$$C_{Fe-c} = C_{Fe-uc} \times F_{Fe} \tag{3.7}$$

where C_{Cr-c} and C_{Cr-uc} are the corrected and uncorrected Cr concentrations, respectively. The same naming style applies to Fe and Al. Given that the total concentration of three elements should remain consistent before and after correction, as illustrated in Equ.3.8, the corrected Al concentrations can be written as follows.

$$C_{Al-c} + C_{Cr-c} + C_{Fe-c} = C_{Al-uc} + C_{Cr-uc} + C_{Fe-uc} \tag{3.8}$$

$$C_{Al-c} = C_{Al-uc} - C_{Cr-uc}\,(F_{Cr} - 1) - C_{Fe-uc}\,(F_{Fe} - 1) \tag{3.9}$$

3.2.5 Transmission electron microscopy

Transmission electron microscopy (TEM) is a widely used technique in materials science for understanding the relationship between microstructure and macro-mechanical properties. The quantitative analysis of defects, such as dislocations, precipitates, and cavities, is essential for understanding the properties of various types of materials for nuclear applications.

The TEM specimens for the ion-irradiated Ni-based superalloys were prepared with focused ion beam (FIB) techniques, utilizing the advanced capabilities of the Zeiss Auriga dual-beam scanning electron microscope at IAMM. A suite of Transmission Electron Microscopy (TEM) instruments was employed for comprehensive microstructure characterization. These included the Thermo Fisher Scientific Spectra 300 and Zeiss Libra 200 S/TEM at IAMM, the FEI Talos F200X, and the JEOL 2100F at ORNL. Electron beam diffraction (EBSD) was employed to verify the positioning of the lamella lift-out near the target zone axes, primarily <001> zone axes, using the Thermo Fisher Helios PFIB dual-beam scanning electron microscope at IAMM. Minor adjustments were made to tilt the specimens after loading them into the TEM for further characterization.

The dislocation loops in the FCC materials were characterized using scanning transmission microscopy (STEM) and conventional TEM under a two-beam condition. Under STEM bright field (BF) conditions, theoretically all types of dislocation loops are visible along the <001> zone axis for FCC materials [68]. However, due to irradiation-induced stress, these loops may undergo deformation and tend to interact with other loops, leading to the formation of dislocation networks during their evolution. To accurately investigate the distorted loops, two-beam TEM analysis is necessary to determine their Burgers' vector and habit planes.

Figure 3.7 provides an illustrative example of the procedure used to quantify the dislocation density. Ham first proposed a method in the 1960s for calculating network dislocation density in a dislocation network within a thin film, as described in Equ. 3.10 [69].

$$\rho = \frac{2N}{Lt} \tag{3.10}$$

where N is the number of intersections, L is the total length of a set of random lines in the measured area, and t is the thickness of TEM sample. To simplify the determination of the total line length L, Meng et al. introduced a meshed grid to replace the original set of random lines [70]. The difference in dislocation density calculated based on the random lines and meshed grid was about 5 %.

The precipitates were analyzed using STEM-energy dispersive X-ray spectroscopy (STEM-EDS) and dark field (DF) techniques in conventional TEM. STEM-EDS provides high-resolution imaging and chemical composition information simultaneously, and it can capture all orientated precipitates in a single image. However, in cases where the precipitate sizes are very small and the number density is high, the elemental mapping can become noisy, making it difficult to directly distinguish precipitates from the background. In such situations, the DF image serves as a valuable complementary method to visualize precipitates and collect statistical information about them.

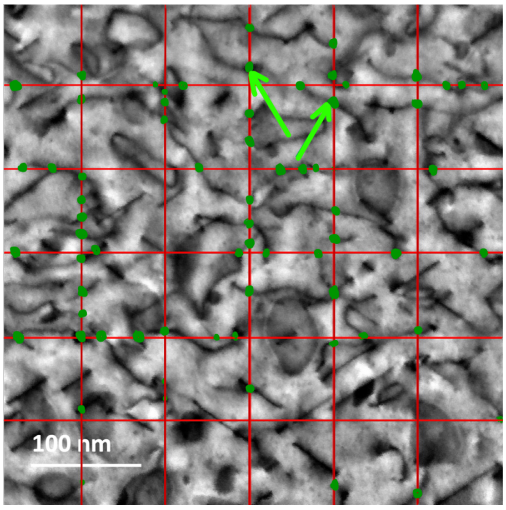


Figure 3.7: The magnified region of implanted ion region with red meshes to calculate the dislocation network density in irradiated Haynes 282 (600 °C, 10 dpa). Tiny dots in green are the intersections between the dislocation network and mesh grids.

Chapter 4

Results

4.1 Phase stability under ion irradiation

4.1.1 $\gamma' - Ni_3(Al, Ti)$

4.1.1.1 Haynes 282

The STEM-EDS technique was applied to analyze the distribution of elements within the sample, profiling from the surface to a depth of approximately 3 μm to investigate the evolution of precipitates under varying radiation damage levels. As an illustrative example, Fig. 4.1 presents the resulting depth dependence for EDS mapping of Ti-enriched precipitates in Haynes 282 irradiated at 600 °C to a dose of 10 dpa, and Fig. 4.2 displays the corresponding number and size distribution of observed Ti-enriched precipitates. These two figures showcase how we track the overall trends in precipitate evolution. Precipitates were categorized into distinct groups with a bin depth interval of 200 nm, and precipitates situated at the boundary of two bins were assigned to the bin where they first appeared. It is worth noting that regardless of whether we characterize the precipitates with enriched elements (e.g., Ti) or depleted elements (e.g., Cr) if the elements within precipitates show strong contrast with the matrix, the statistical counting results will be consistent. In this case, the deviations in size and number density were less than 1 %.

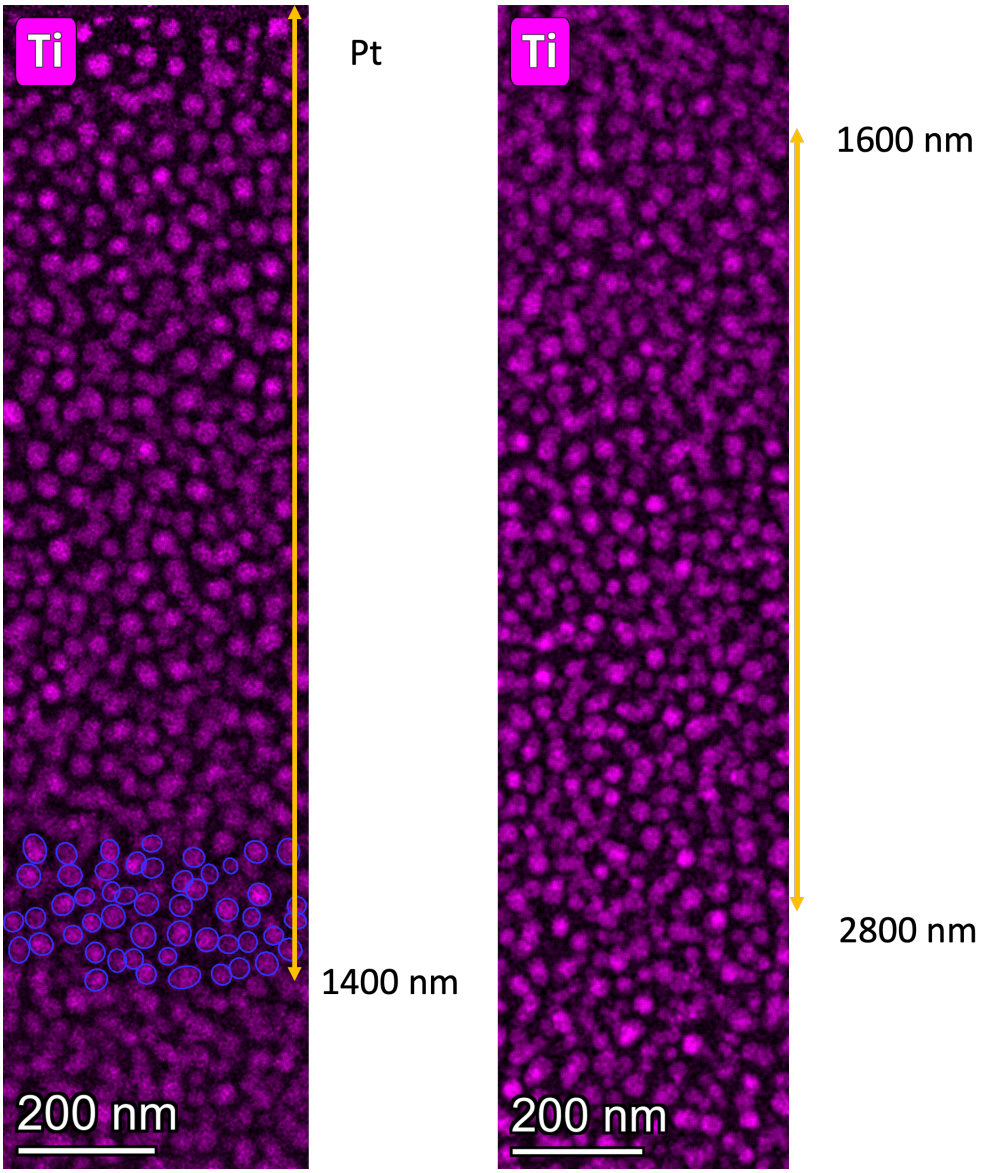


Figure 4.1: Titanium EDS maps highlighting the precipitate distribution in aged Haynes 282 irradiated by Ni ions to a midrange dose of 10 dpa at 600 °C: Profiling from the surface (Pt protective layer) to 3μm depth. Annotated in blue ellipsoids, we provide a representative example, illustrating one group with depths between 1200 nm and 1400 nm, for a comprehensive understanding of precipitate distribution.

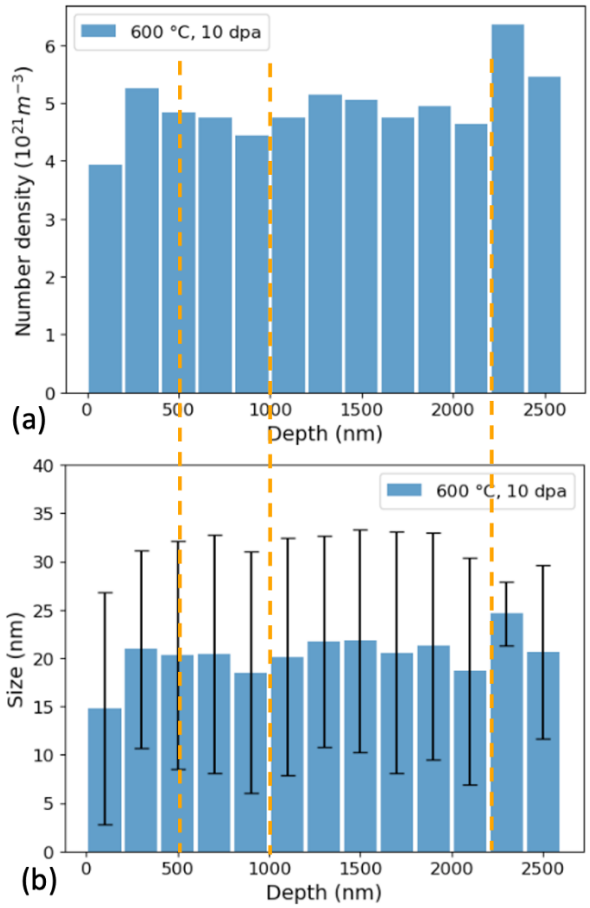


Figure 4.2: The statistical depth dependence of γ' precipitates in irradiated aged Haynes 282 (600 °C, 10 dpa).

We conducted the same analysis for the three other investigated conditions, as illustrated in Figure A.3 in the Appendix A.2.1. Fig. 4.3 presents a comprehensive overview of the statistical distribution for size and number density of γ' precipitates in Haynes 282 across varying irradiation conditions. When combined with the results presented in Appendix A.2.1 Table A.1, it becomes evident that neither precipitate size nor number density exhibits a clear dose or irradiation temperature dependence; all of the precipitate parameters remain more or less unchanged (within experimental uncertainties and the precipitate size range of Haynes 282 with two-step standard aging treatment in the relevant references [71, 72, 73]) irrespective of exposure temperature, dose, and whether the region was irradiated or unirradiated. It is essential to note that the primary source of error in number density arises from the estimation of TEM sample thickness, which is about 25 %. When including statistical counting errors, the total relative number density error amounts to roughly 26 %. The relative error in size distribution stands at approximately 15 %, which introduces large uncertainty when used in volume fraction calculations. Consequently, we provide only an approximate value for volume fraction estimation.

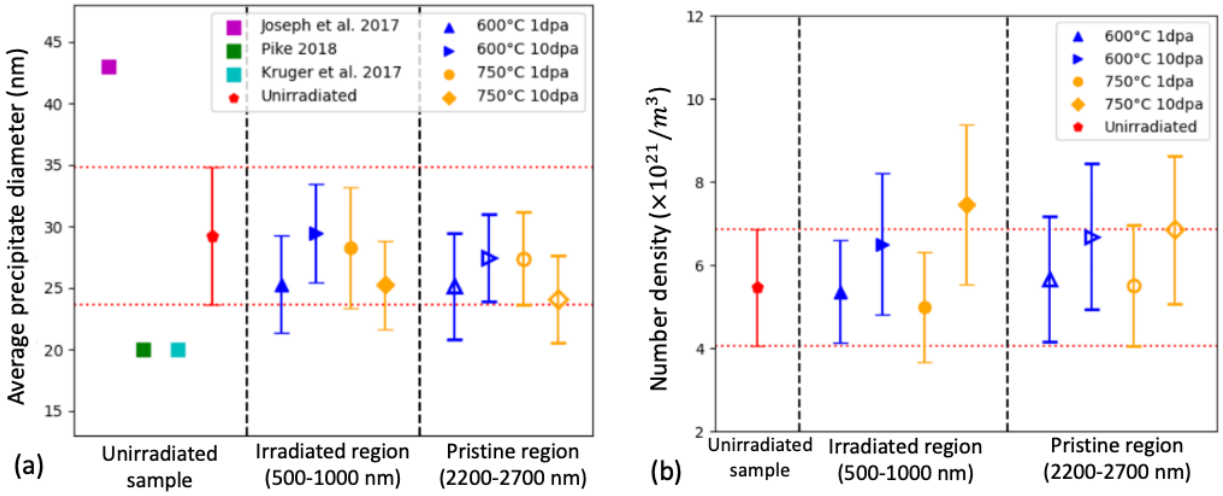


Figure 4.3: The summary of a statistical distribution (a) precipitate size and (b) number density of γ' precipitates in Haynes 282 under various conditions. The solid circles represent the data calculated from irradiated regions, and the hollow circles are based on the pristine regions in the same irradiated sample.

In subsequent parts of this paper, our analysis focused on the irradiated region spanning from 500 to 1000 nanometers in depth to minimize being affected by ion irradiation-induced artifacts. The data of the pristine region was measured beyond 2.2 μm.

4.1.1.2 Haynes 214

Figure 4.4 shows the distribution of $Ni_3Al - \gamma'$ precipitates in the irradiated region after exposure to 600 °C for 1 and 10 dpa doses. The γ' precipitates were uniformly distributed within the top 1.3 μm of the irradiated region. From 1.5 μm to 2 μm, corresponding to the peak damage/implanted ion region, γ' precipitates continued to grow, even though their number density appeared lower compared to other regions. The γ' precipitates also grew in the pristine region, even after a short thermal exposure of 16 minutes at 600 °C, as shown in Fig.4.5(a), although the precipitate signal was weaker. Additional reflections of γ' precipitates were observed in both the irradiated region and pristine region along the [001] zone, as seen in Fig. 4.5(b) and (c). Larger but fewer γ' precipitates grew in 750 °C. Fig. 4.6 presents a comprehensive overview of the statistical distribution for size and number density of γ' precipitates in Haynes 214 across varying irradiation conditions. The corresponding precipitate information is listed in the Appendix A.2.1 Table. A.2. We observed a higher number density but smaller γ' precipitates in Haynes 214 irradiated at 750 °C with a dose of 1 dpa, compared to the 10 dpa sample, which might suggest that Ostwald ripening occurred, where larger precipitates grow at the expense of smaller ones. However, the 600 °C samples did not clearly observe this trend. In the 600 °C, 1 dpa sample, many precipitates were likely missed during manual counting due to weak contrast and blurry boundaries in the early stages, which may have led to an underestimated number density. Additionally, as shown in Fig. 3.3, the holding time in the furnace waiting for a good vacuum status before irradiation varied between samples, resulting in unplanned thermal exposure that may have greatly affected the intended experimental conditions.

4.1.1.3 Summary of γ' phase stability

The γ' precipitates in Haynes 282 and Haynes 214 demonstrated strong resistance to irradiation-induced ballistic mixing under the current irradiation conditions. The high

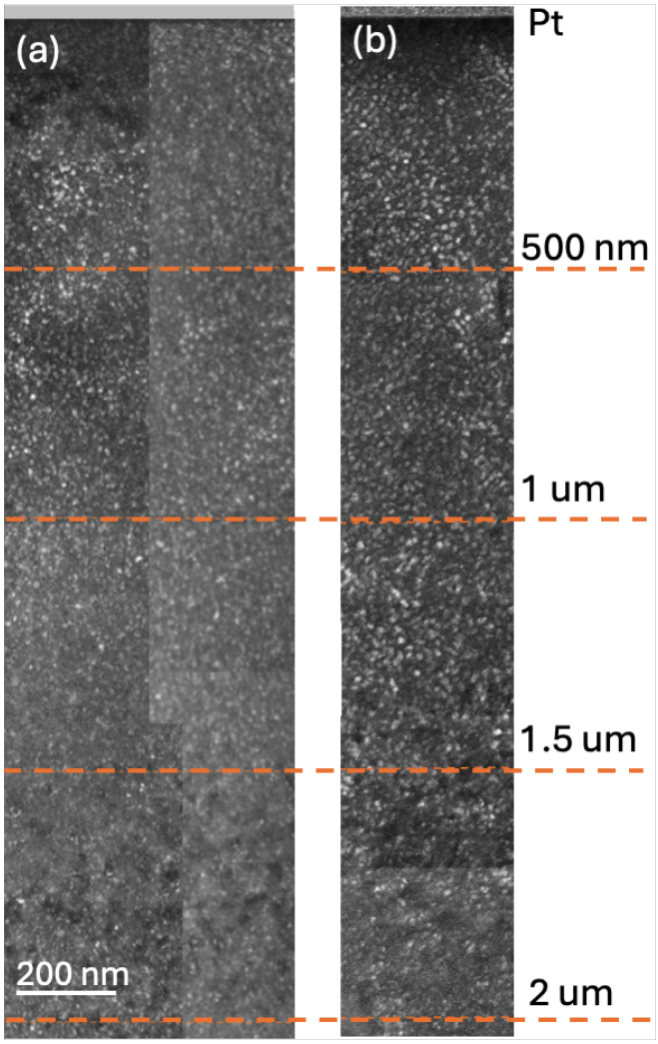


Figure 4.4: TEM dark field images of Haynes 214 irradiated at 600 °C with a dose of (a) 1 dpa and (b) 10 dpa, captured along zone [011].

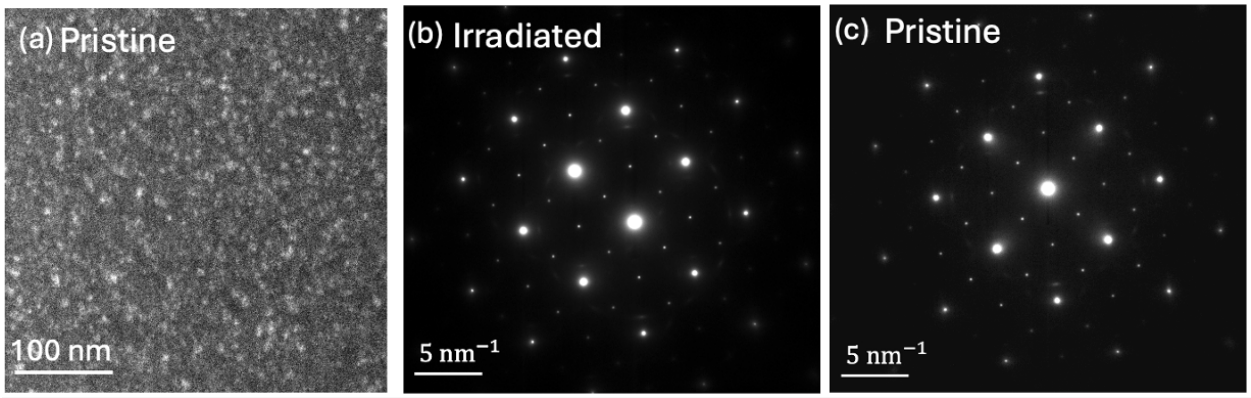


Figure 4.5: Micrographs of Haynes 214 irradiated at 600 °C with a mid-range dose of 1 dpa: (a) The magnified TEM dark field image captured from the pristine region; (b) and (c) are electron diffraction patterns from the irradiated region and pristine region, respectively.

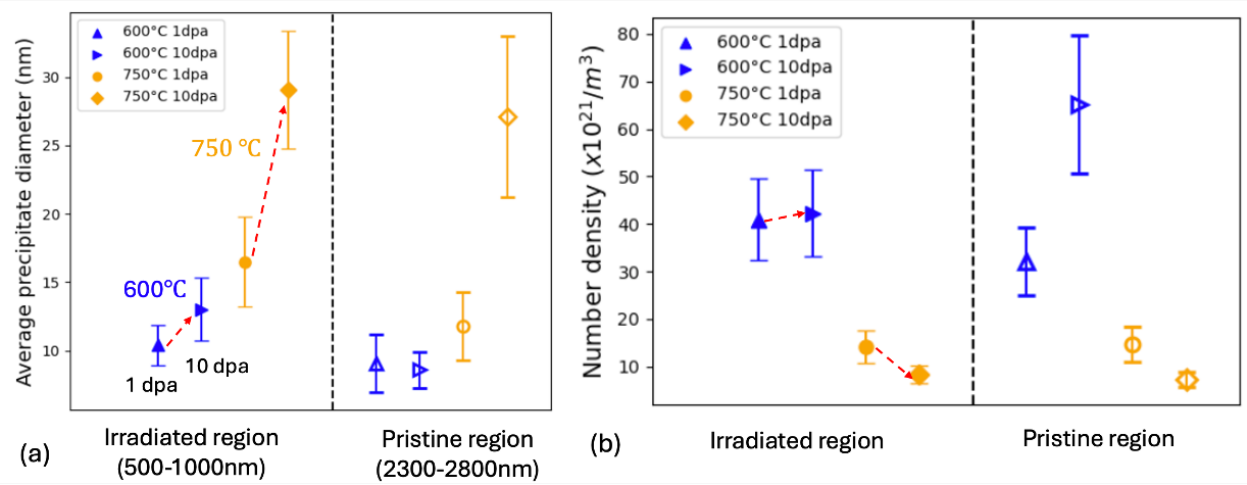


Figure 4.6: The summary of a statistical distribution (a) precipitate size and (b) number density of γ' precipitates in Haynes 214 under various conditions. The solid circles represent the data calculated from irradiated regions, and the hollow circles are based on the pristine regions in the same irradiated sample.

diffusivity of solute atoms within the precipitates may contribute to radiation-enhanced diffusion and thermal recovery to avoid dissolution. Since Haynes 282 is specifically designed to contain γ' precipitates, whereas Haynes 214 is intended to operate without them, Haynes 282 exhibits superior structural integrity under irradiation.

4.1.2 Ni_2(Mo, Cr, W) precipitates

4.1.2.1 Aged Haynes 244 STD

Figure 4.7(a) shows a TEM dark-field image of the Ni_2(Mo, Cr, W) precipitate distribution in aged Haynes 244 after irradiation at 600 °C to a dose of 1 dpa. The precipitates display sharp contrast within the top 500 nm, maintaining their original shape in the radiation-safe analysis region between 500 nm and 1 μm depth. A clear transition is observed in Fig. 4.7(b), from well-defined precipitate boundaries to more diffuse contrast. Precipitate-enriched elements, such as Mo, diffuse into the matrix, while Cr and Fe diffuse more uniformly with increasing depth. Many precipitates dissolve in the implanted ion region, resulting in a lower number density than in other regions. Besides, W atoms did replace a certain amount of Mo and Cr during thermal aging, forming Ni_2(Mo, Cr, W) precipitates, although the segregation level is not as pronounced as that of Mo. The 10 dpa sample exhibits the same tendency as the 1 dpa sample, as shown in Fig.A.4 in Appendix A.2.2. Almost no precipitates are visible in the implanted ion region, between 1.5 μm and 2 μm, suggesting significant ballistic mixing and dissolution occurred. The precipitates cannot recover thermally, likely due to limited diffusivity or chemical composition changes resulting from the higher Ni content in this region.

Figure 4.8(a) shows the elemental mapping of aged Haynes 244 irradiated at 750 °C to a mid-range dose of 10 dpa. The Ni_2(Mo, Cr, W) precipitates retained their original shapes, with no clear evidence of diffusion mixing, even in the peak dose region. The corresponding elemental concentrations are plotted in Figure 4.8(b). Considering potential errors from the STEM-EDS measurements and regional concentration differences, the Mo, Cr, and W content in the Ni_2(Mo, Cr, W) precipitates in the irradiated region remained

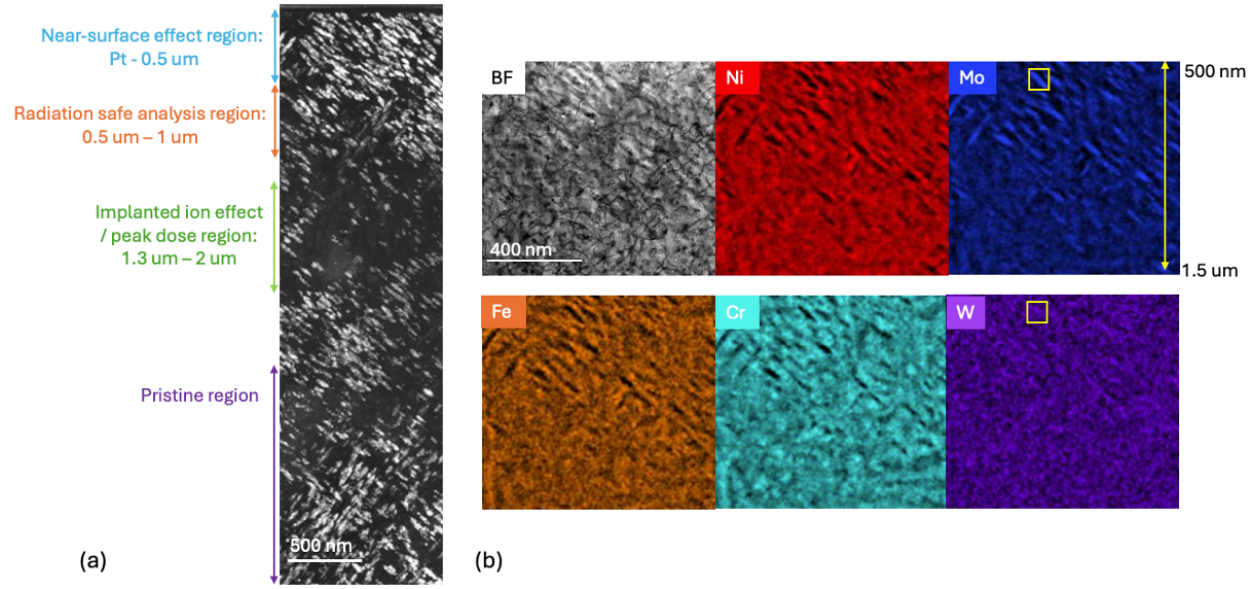


Figure 4.7: (a) Dark-field image showing the precipitate distribution in aged Haynes 244 irradiated by Ni ions to a midrange dose of 1 dpa at 600 °C. Profiling extends from the surface (Pt protective layer) to a depth of approximately 4 µm; (b) Detailed STEM-EDS analysis reveals that the element distribution varies with radiation damage as a function of depth. The yellow rectangle highlights the W atoms enriched in the precipitates.

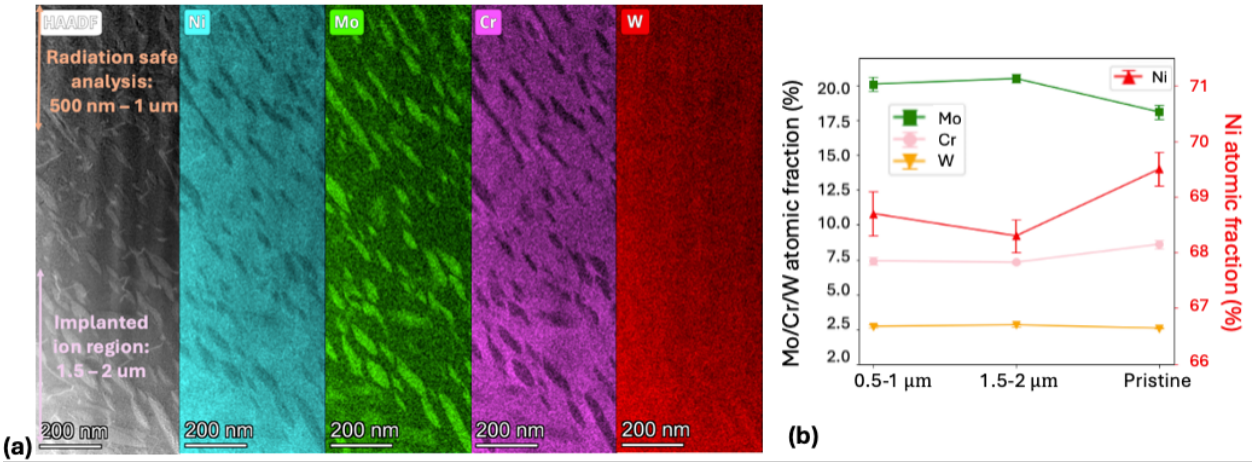


Figure 4.8: (a) STEM-EDS mapping of aged Haynes 244 irradiated at 750 °C with a mid-range dose of 10 dpa; (b) the corresponding atomic fraction of key elements in Ni_2(Mo, Cr, W) at different depths.

relatively unchanged compared to the pristine region. There was no noticeable radiation-induced effect on the distribution of Ni_2(Mo, Cr, W) precipitates, and fluctuations in the number density fell within the margin of error.

Figures 4.9(a) and (b) further confirm the presence of a competitive relationship among different variant types, leading to heterogeneous distributions. Additional quantification across different grains may help to mitigate this variability. As previously mentioned, estimating the number density remains a big challenge. While STEM-HAADF can reveal all variants—unlike TEM dark-field images, which typically show only two or three—it is limited to specific conditions. These conditions include precipitates with well-defined contours, minimal interference from other features, and the need to adjust detector angles carefully. In theory, STEM-EDS should be able to detect all precipitates, but in practice, contrast differences between variants are often observed. This is likely caused by differences in variant orientation, which affect detector efficiency due to varying X-ray emission angles or changes in the interaction volume between the precipitates and the transmitted electrons. Consequently, some variants may be present but exhibit weak intensity in the elemental maps, making them difficult to distinguish. Employing multi-grain samples and using multiple zone axes for observation could provide more comprehensive information on the precipitates, which are costly and time-consuming. Therefore, a more accurate and efficient method for estimating number density from limited data is needed. After analyzing all available data, especially the precipitates in pristine regions in the STEM-HAADF images, we observed a correlation between the precipitate number density and the area ratio, defined as the ratio of pixels covered by precipitates to the total pixels in the image.

When all variants are visible, the area ratio ranges from 0.30 to 0.35. Based on this, we assume that all variants occupy approximately 30 % of the total image area in the aged Haynes 244 samples. In this study, we estimate the density of the number mainly using dark field images. We first measure the area ratio $r_{covered}$ in the pristine region to get the correction ratio $c_{area} = 0.3/r_{covered}$, and then apply the correction ratio c_{area} in the irradiated region. The precipitate number densities N_{total} is adjusted based on this assumption from the measure number density $N_{measured}$, that is $N_{total} = c_{area} \times N_{measured}$. The information of corrected precipitate size and number density is listed in the Appendix A.2.2 Table. A.3.

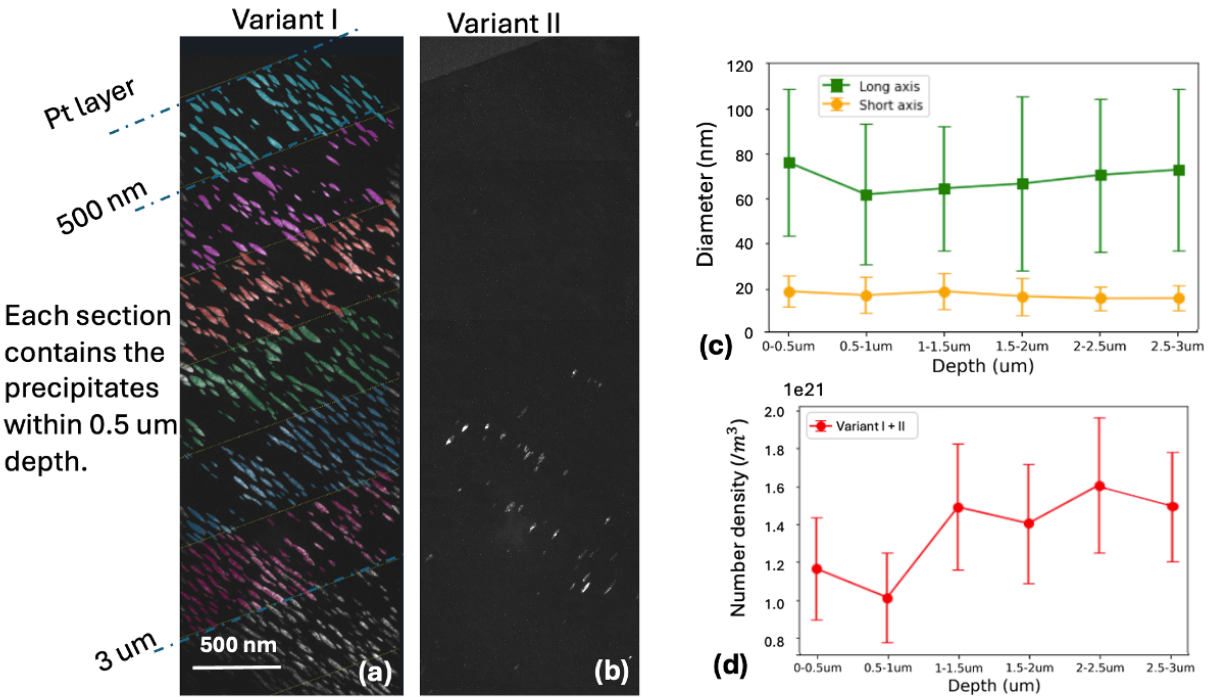


Figure 4.9: Dark field images of (a)Variant I and (b) variant II taken along zone [001] axis of 750 °C, 10 dpa irradiated aged Haynes 244 sample; (c) and (d) are the corresponding depth dependence of the precipitate size and number density distribution.

Overall, aged Haynes 244 exhibited good phase stability under high-temperature (750 °C) and high-dose (10 dpa) irradiation, while precipitates dissolved under low-temperature (600 °C) irradiation, even at a dose as low as 1 dpa.

4.1.2.2 Solutionized Haynes 244 SHT

In the Fig.4.10(a), apparent precipitate growth is observed in the irradiation-safe analysis region at the depth from 500 nm to 1 μm in the 600 °C, 1 dpa Haynes 244SHT, driven by radiation-enhanced diffusion. The diffraction pattern from the irradiated region exhibits sharp, long-range ordering reflections from the Ni_2(Mo, Cr) precipitates. In contrast, the diffraction pattern from the pristine region shows similar long-range ordering reflections but with an additional diffraction ring indicative of nanocrystalline. However, distinguishing between the precipitates and noise in the camera image is challenging via the TEM dark field technique.

Therefore, the precipitate growth was verified using atom probe tomography. In the pristine region, Mo-enriched clusters are visible on the 18 at.% Mo iso-concentration surface, as shown in Fig. 4.11. The atomic composition and radius of these clusters were determined from the proxigram at the cluster-matrix interface. The composition of the Mo-enriched clusters, 64Ni-10Cr-22Mo at.%, aligns with the Ni_2(Mo, Cr) precipitates. The approximate radius of the 15 largest precipitates in the pristine region is about 1.5 nm, which is near the resolution limit of TEM, leading to uncertainty and difficulty in observing them via TEM.

The precipitate size continued to grow with increasing doses at 600 °C. In three randomly selected grains, Ni_2(Mo, Cr) precipitates were observed along the [001] zone axis, as shown in Fig. 4.12. The number density varied across the grains, reflecting competition between variants and their heterogeneous distribution, as previously discussed for aged Haynes 244. This variation in number density and precipitate size could result in significant differences in precipitate strengthening within the material.

Significant solute segregation was observed from the APT atom maps of various elements of 600 °C, 10 dpa 244 SHT, as shown in Fig. 4.13(a). Elemental depletion, particularly of W and Al, is evident in the top left corner, highlighted by the red rectangle. The corresponding region in the Mo iso-concentration surface is identified as a Mo-enriched

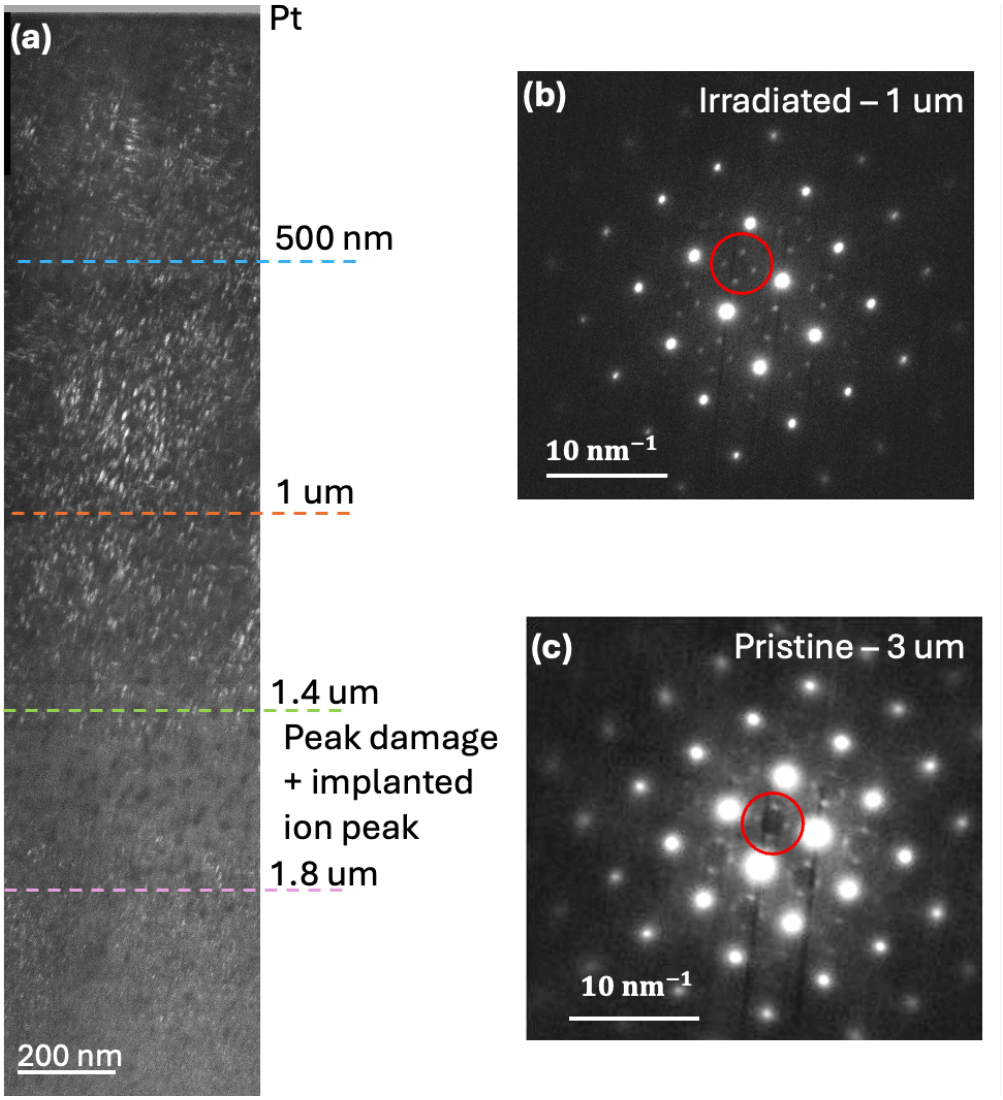


Figure 4.10: TEM micrographs of 244SHT irradiated at 600 °C with a mid-range dose of 1 dpa; (b) and (c) are the corresponding electron diffraction patterns of the irradiated region and pristine region, respectively.

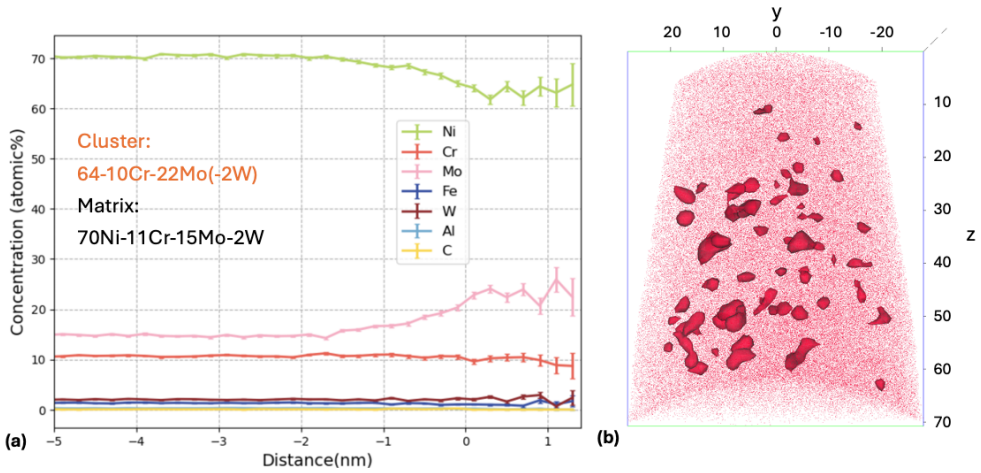


Figure 4.11: APT analysis of Haynes 244 SHT irradiated to 1 dpa at 600 °C: (a) atomic concentrations and (b) 18 % Mo iso-concentration surfaces obtained from the pristine region.

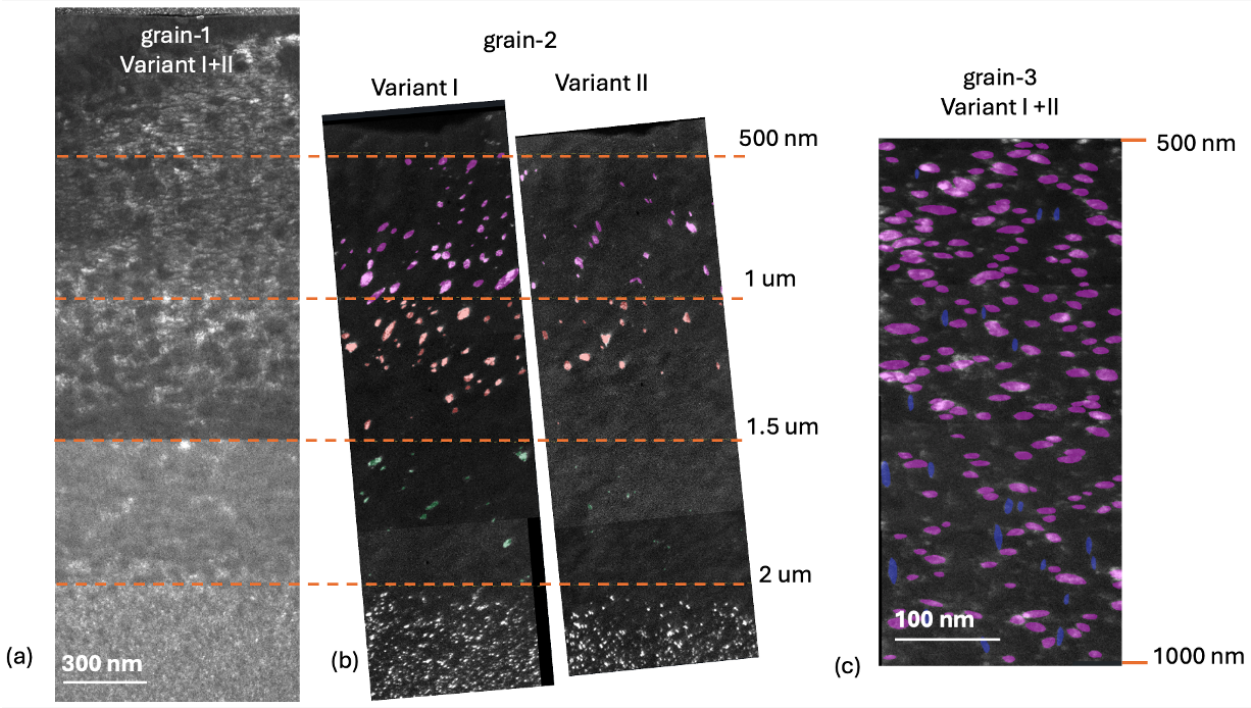


Figure 4.12: Dark-field images of different grains selected from irradiated 244 SHT at 600 °C with a mid-range dose of 10 dpa. (b) and (c) are annotated images.

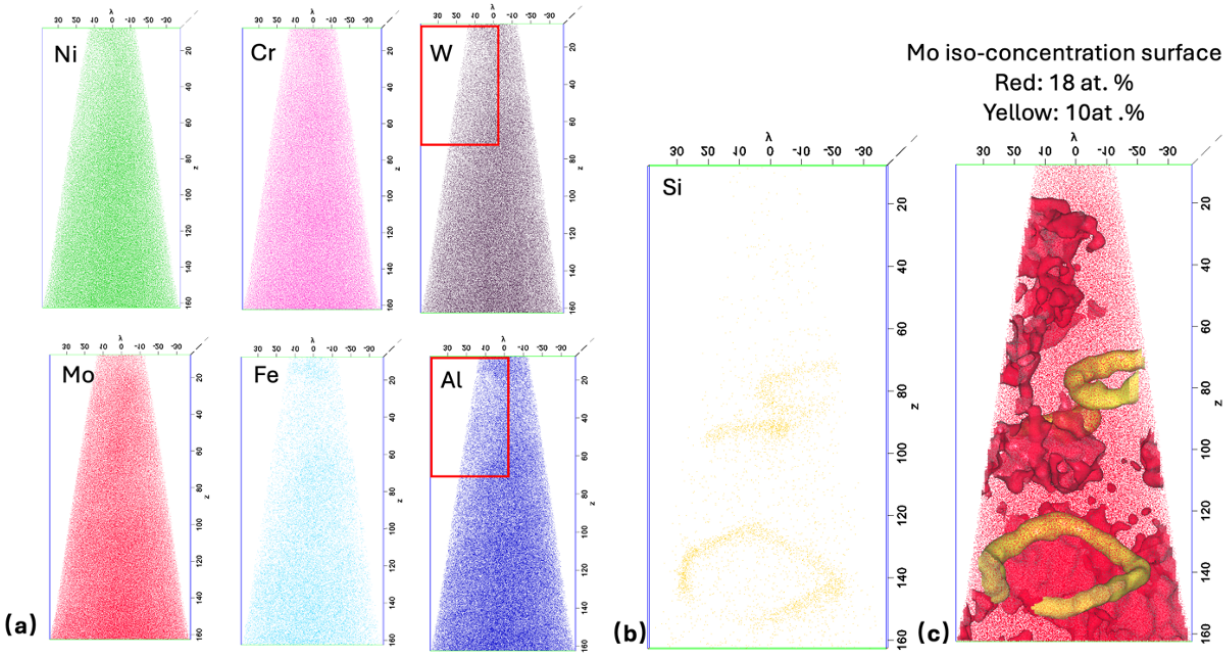


Figure 4.13: (a) APT atom maps of various elements in the irradiated region of 244 SHT after irradiation at 600 °C to a mid-range dose of 10 dpa; (b) Si distribution and (c) Mo iso-concentration surface of the same region.

precipitate, confirmed to be Ni_2(Mo, Cr) based on its atomic composition of 67Ni-11Cr-18.5Mo at.% derived from the proxigram at the matrix-precipitate interface. The large Ni_2(Mo, Cr)precipitates don't have clear boundaries, which may correlate with the patchy and discontinuous contrast seen in TEM dark field images. In Fig.4.14(a), no obvious concentration increment of W can be observed around the Ni_2(Mo, Cr) precipitates, which is unlike the enrichment of Ni_2(Mo, Cr, W) precipitates formed during the standard thermal aging process. From the plot of nearest neighbor distribution of W in order 10 as shown in Fig4.14(b), the experimental data just overlapped on the randomized data, suggesting no obvious segregation occurred, probably due to the slow diffusion rate of W. One hypothesis is that Ni_2(Mo, Cr) precipitates form during the early stages of precipitation, with W atoms gradually substituting some Cr or Mo atoms over prolonged isothermal aging and forming Ni_2(Mo, Cr, W) precipitates in the standard-aged 244 STD. In contrast, Al shows a strong tendency to cluster. However, the bulk concentration of Al is too low to form a crystalline structure (e.g. $L1_2$), or be detected via TEM diffraction patterns. Besides, radiation induced

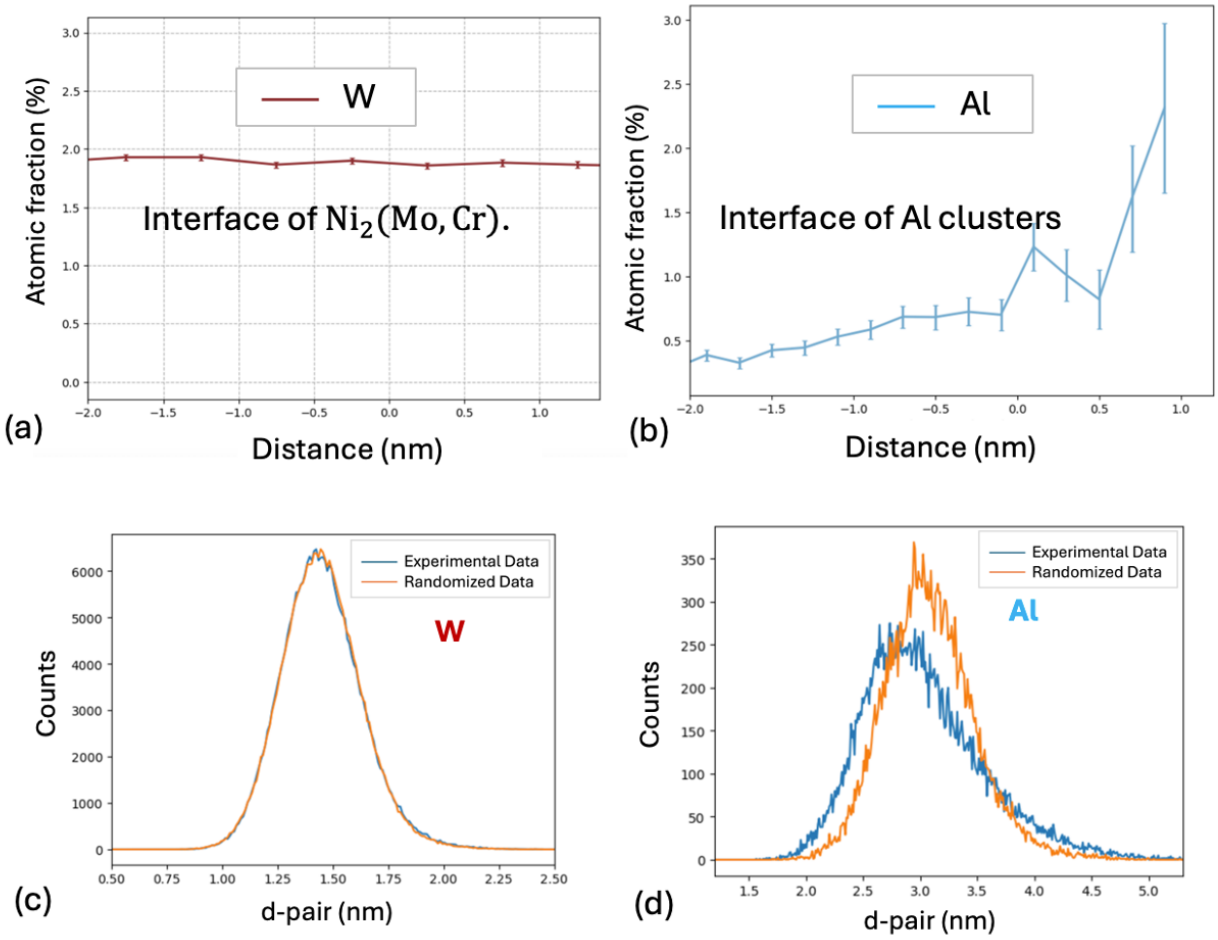


Figure 4.14: Concentration of (a) W and (b) Al at interfaces of Ni_2(Mo, Cr) precipitates and Al enriched clusters with matrix, respectively; Nearest neighbor distribution of (c) W and (d) Al in order of 10.

dislocation loops are Si enriched, which have been observed in many APT studies of irradiated materials [74, 75].

Fig.4.15(a) shows the STEM bright filed image of 244 SHT, following the irradiation to 1 dpa at 750 °C, where only a few stacking faults are visible. No additional reflections from long-range ordered $Ni_2(Mo, Cr)$ phases are present. However, a peak at the $1\frac{1}{2}0$ reciprocal lattice position in the corresponding electron diffraction, captured in the irradiated region, indicates that a local short-range ordering occurred in the disordered γ matrix [54, 76]. In both irradiated and pristine regions characterized by APT, the Pearson coefficients μ of element frequency distribution analysis for each element remain below 0.1, indicating uniform distribution and the absence of significant segregation during short-term irradiation. Both APT and TEM results confirm that no clustering occurred in either the irradiated or pristine regions of the 750 °C, 1 dpa Haynes 244SHT sample, which is likely because the irradiation temperature is close to the critical transformation temperature ($\sim$ 775 °C [54]), which requires more time for nucleation in the kinetic ordering transformation from short-range ordering to long-range ordering [54, 55, 76].

In contrast to the low-dose (1 dpa) Haynes 244SHT irradiated at 750 °C, numerous precipitates formed in both the irradiated and pristine regions of the 10 dpa sample, except

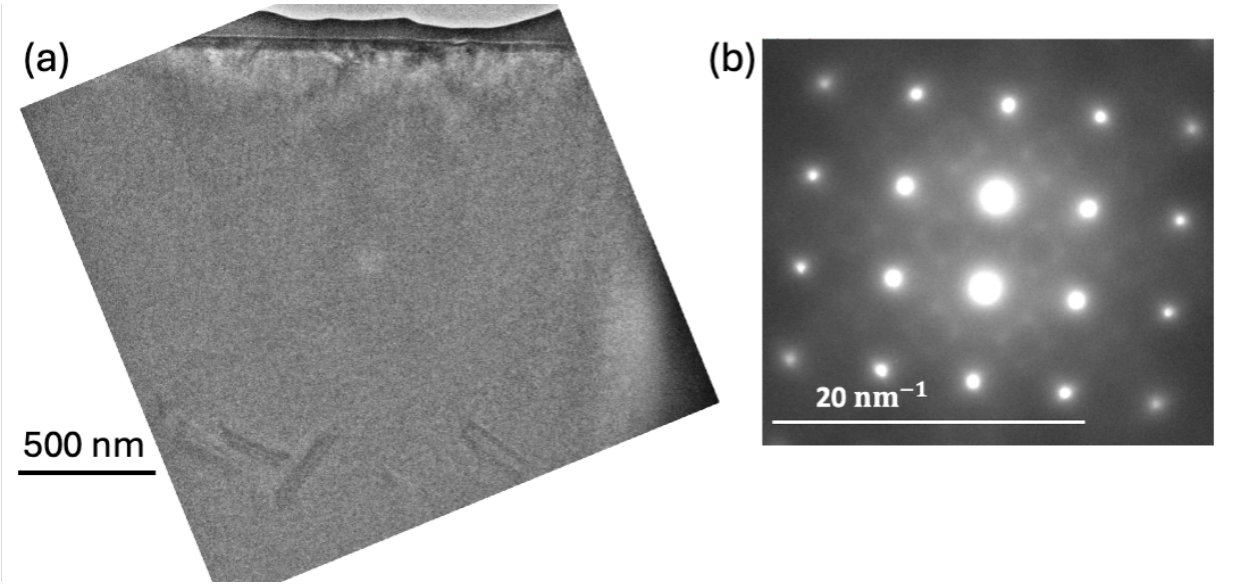


Figure 4.15: (a)STEM bright field image and (b) the electron diffraction of 244SHT irradiated at 750 °C with a mid-range dose of 1 dpa.

in the implanted ion region, as shown in Fig.4.16. In this region, the injected ions may have altered the local chemical composition, suppressing precipitation, or strong ballistic mixing in the radiation damage peak may have dissolved the precipitates. Since it is unclear which mechanism is predominant, data from the radiation-safe analysis region (located at a depth of 500–1000 nm beneath the Pt protective layer) was used to assess radiation effects while minimizing artifacts from ion irradiation. The precipitates were large but sparse in the radiation-safe analysis region where irradiation-enhanced diffusion dominated. In contrast, they were small but dense in the pristine region, suggesting that the coarsening mechanism could be Ostwald ripening. The detailed summary of precipitates is listed in the Appendix A.2.2 Table. A.4.

4.1.2.3 Summary of Ni_2(Mo, Cr, W)/Ni_2(Mo, Cr) phase stability

Ni_2(Mo, Cr, W) are sensitive to both radiation damage and thermal effects. At 600 °C, these precipitates in pre-aged Haynes 244STD partially dissolved or shrunk at low doses, and were completely dissolved in the implanted ion region. In contrast, at 750 °C, Ni_2(Mo, Cr, W) precipitates in the aged sample demonstrate remarkable stability, with size and number

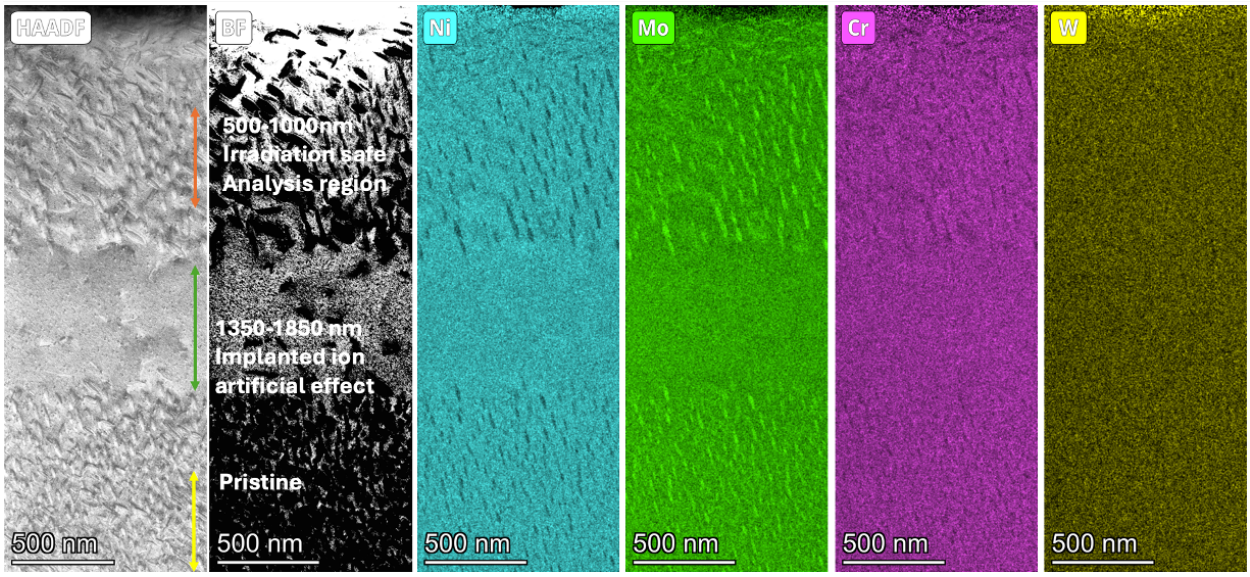


Figure 4.16: STEM-EDX results of irradiated Haynes 244-SHT (750 °C, 10 dpa). The first two are the high-angle annular dark field (HAADF) image and bright field image; the others are the Ni, Mo, Cr, and W EDX maps.

density remaining consistent post-irradiation. For solutionized Haynes 244SHT samples, the Ni_2(Mo, Cr) grew in both irradiated regions and pristine regions subjected to long time high temperature exposure except for 750 °C, 1 dpa sample. In the irradiated regions, precipitates appear larger but are relatively sparse. Unlike the pre-aged samples, no W segregation was observed in precipitates in the solutionized samples, likely due to the slow diffusion rate of W.

4.1.3 Other secondary phases

4.1.3.1 $Cr_{23}C_6$

In Fig.4.17(c), a new diffraction pattern is observed in the irradiated region of Haynes 214 irradiated at 750 °C, with a mid-range dose of 1 dpa. Despite using the smallest objective lens in the Spectra 300, five reflection spots are still selected, as shown in the red circle in Fig.4.17(c). Blocky precipitates exhibit stronger contrast compared to the spherical γ' precipitates. The yellow rectangle in Fig.4.17(a) and (b) exemplify how precipitates might be closely related to dislocation lines, though not all dislocations nucleate precipitates, as indicated by the purple rectangle. The magnified images and corresponding STEM-EDS mapping are plotted in Fig.4.18, suggesting the new secondary phase is Cr and C enriched. Since EDS technique is not sensitive to light atoms like carbon, atom probe tomography (APT) is applied for more accurate chemical quantification.

The atomic distribution of major elements at the depth from 500 to 800 nm in irradiated Haynes 214 (750 °C, 1 dpa) is depicted in Fig.4.19. The atomic composition of the cluster is identified as 85Cr-5Ni-10C, which is close to the $Cr_{23}C_6$ carbides. The carbon concentration is likely underestimated via the APT technique, commonly due to the laser evaporation mode with a relatively high pulse energy. The phase identification of $Cr_{23}C_6$ is further verified in the Appendix A.2.3.

Under four different irradiation conditions in Haynes 214, dense dislocation lines and $Cr_{23}C_6$ carbides were only observed in 750 °C, 1 dpa sample. By rotating the zone axis from [001] to [103] zone, the precipitates continued to overlap with the dislocation lines. Although the rotation angle is only about 18.5°, the tendency of Cr carbides to attach on

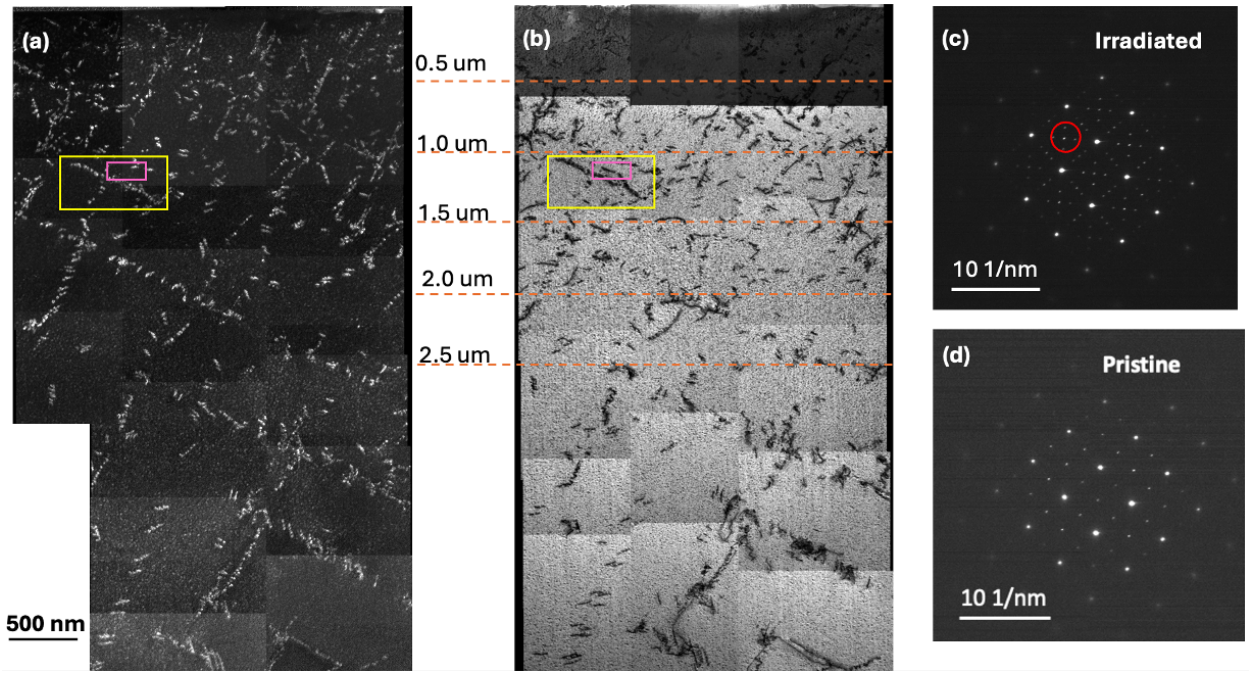


Figure 4.17: (a) TEM dark field image with a 10 μ m objective aperture along [001] zone axis, as highlighted by the red circle in (c); (b) STEM bright field image showing dislocation distribution; (c) and (d) show electron diffraction patterns, captured from the irradiated and pristine regions, respectively.

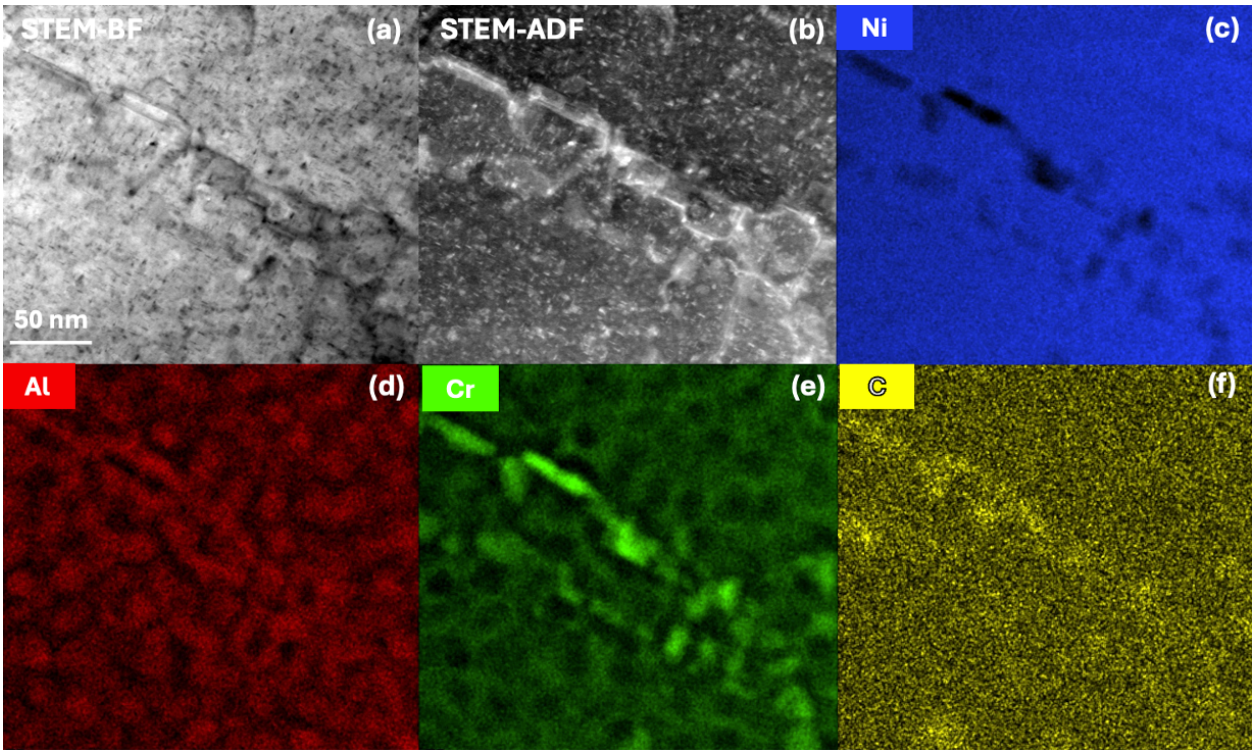


Figure 4.18: (a)STEM bright field image, (b)STEM HAADF, and (c)-(f) EDS results of various elements.

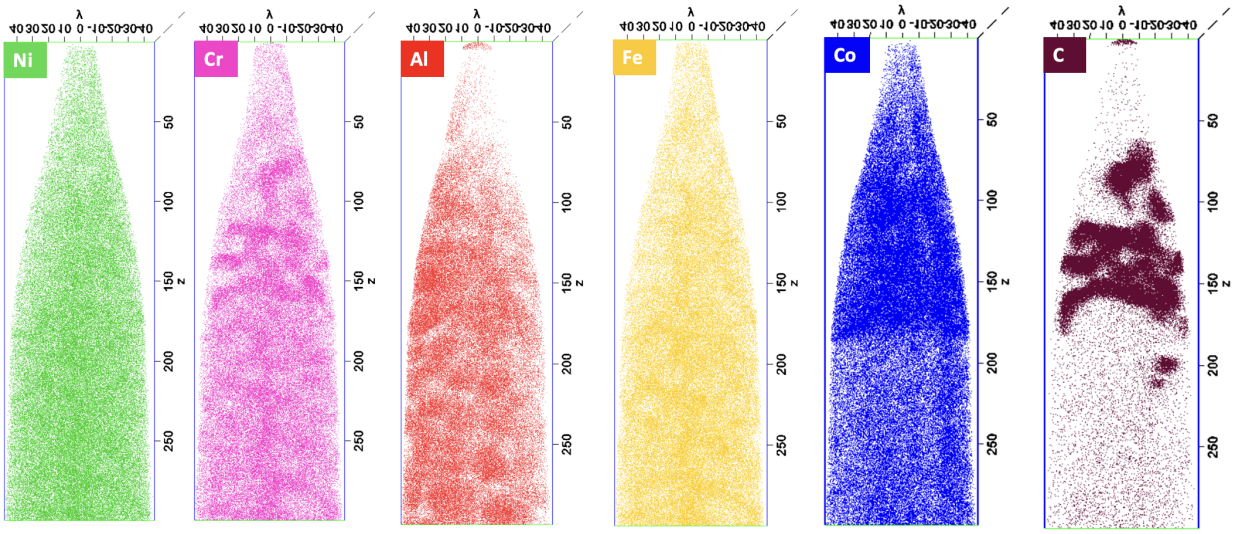


Figure 4.19: APT atom maps of Haynes 214 following irradiation to 1 dpa at 750˚in the irradiated region at a depth of 500 nm from the sample surface, showing the presence of two distinct precipitates.

dislocations remained evident. This observation can be further verified by preparing a TEM lift-out along zone $< 013 >$ to increase the available rotation space in α/β tilting in TEM, allowing for a more comprehensive analysis of the dislocation-precipitate relationship. Since the heating data for this sample is missing, it remains unclear whether the initial dislocation lines were not fully annealed in this sample before the irradiation started. Without this information, it is difficult to determine the mutually complementary symbiotic relationship between dislocation lines, carbides, temperature, irradiation, and thermal exposure time.

4.1.3.2 μ phase and M_6C

In Hastelloy C-276, the electron diffraction pattern remained unchanged across all irradiation conditions, whether captured from the irradiated or pristine regions, suggesting that the $\gamma-$disordered FCC structure remained the dominant phase within the matrix, as exampled in Fig.4.20(b). We focused on a small area of radiation-safe analysis region of Hastelloy C-276 with a midrange dose of 10 dpa at 600 °C, as shown in Fig.4.20. Radiation-induced element segregation was observed only at dislocations where Ni was enriched, and Cr, Mo were depleted. This element distribution confirms that no secondary Mo-enriched phase, including Ni_2(Mo, Cr), μ, and carbides, were produced due to irradiation-enhanced diffusion.

Since no precipitation was observed within the matrix, the grain boundaries were rapidly examined in the 10 dpa samples, as shown in Fig.4.21. No precipitates were observed along the grain boundaries in the 600 °C sample, and minimal elemental segregation (particularly of Ni) was observed, likely due to radiation-induced mixing. In the 750 °C, 10 dpa sample, Mo-enriched precipitates were found to form along grain boundaries heterogeneously. Additionally, changes in grain boundary morphology were evident in the irradiated region, with precipitates dissolving at the peak damage region and diffusing into the matrix in other irradiated areas. Considering that secondary phases in the matrix could increase susceptibility to stress corrosion cracking and negatively impact mechanical properties [77], Hastelloy C-276 exhibits superior metallurgical stability compared to other Ni-Cr-Mo alloys under high-temperature conditions, both with and without irradiation exposure.

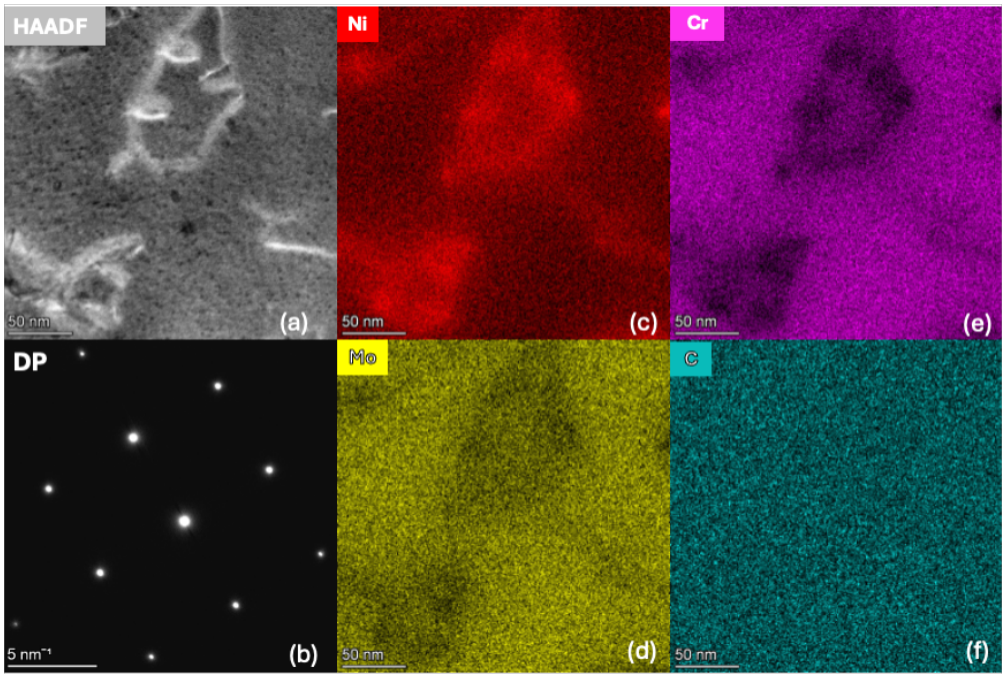


Figure 4.20: (a) BF-STEM and (b) SAED images of the region at a depth of 650 nm to 900 nm in Hastelloy C-276 to a midrange dose of 10 dpa at 600 °C, and (c)-(f) detailed STEM-EDS results showing the distribution of various elements.

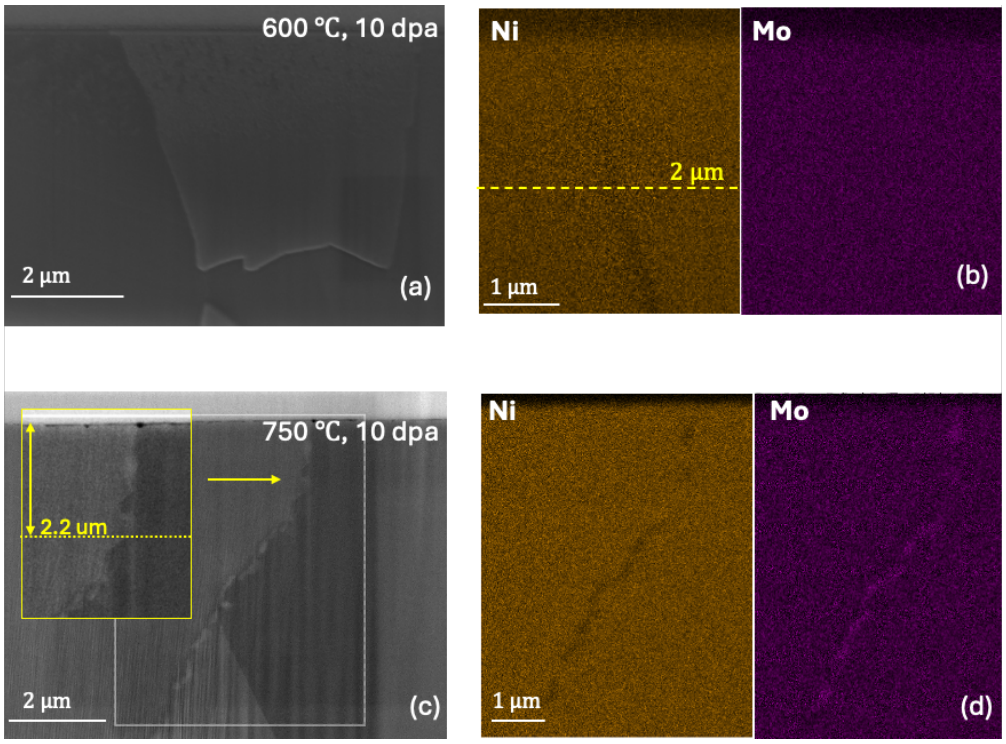


Figure 4.21: (a) and (c) are the SEM images, (b) and (d) are the EDS mappings for grain boundaries in Hastelloy C-276 irradiated at 600 °C and 750 °C, respectively, with a mid-range dose of 10 dpa.

4.1.4 Dislocation evolution

Radiation-induced dislocations were observed exclusively in the samples irradiated at 600 °C. Figure 4.22 shows a TEM cross-section overview of the overall dislocation distribution in irradiated Haynes 282 (600 °C, 10 dpa), compared with the SRIM profiles for dose and implanted ions. The depth profile reveals distinct microstructural regions with varying dislocation characteristics. Generally, in the near-surface region (0-500 nm), the density of dislocation loops was noticeably lower compared to other irradiated areas. The point defects can easily escape or annihilate at the free sample surface. Moving into the "radiation-safe" analysis region (500-1000 nm), we observed a prevalence of $< 111 >$ type faulted loops along with some $< 011 >$ perfect loops. During long-time high-temperature irradiation, the dislocation microstructure experienced the simultaneous formation of new $< 111 >$ loops and the growth of existing ones. Notably, faulted loops might undergo unfaulting processes, transforming into perfect loops through interactions with $< 112 >$ Shockley partial dislocations. Some loops undergoing a transformation process were captured in this region. In the transition region (1-1.5 μm), we observe $< 111 >$ faulted loops as the dominant dislocation type, similar to the radiation-safe analysis region. However, the density of these loops was notably higher due to the increased radiation doses. In the implanted ion region (1.5-2 μm), the dislocation structures evolved into larger loops and complex dislocation tangles. This region marked the initiation of dislocation network formation, primarily driven by loop interactions. The bombarding ions are deposited near the region of peak displacement damage, resulting in a localized surplus of interstitial atoms and disrupting the balance of vacancy supersaturation.

In this study, we focus on the region 500–1000 nm beneath the sample surface, designated as the irradiation-safe analysis region, to minimize artifacts from near-surface and implanted ion effects [15, 48, 6]. The dislocation distributions of materials irradiated at 600 °C, within this depth range, are shown in Figures 4.23 to 4.24. No radiation-induced dislocation loops were observed in this region of irradiated Haynes 214. Thus, the summarized STEM-BF image of Haynes 214 is excluded here. The detailed information of dislocation loop size, number density and dislocation line density is listed in the tables A.1 to A.4 in the Appendix.

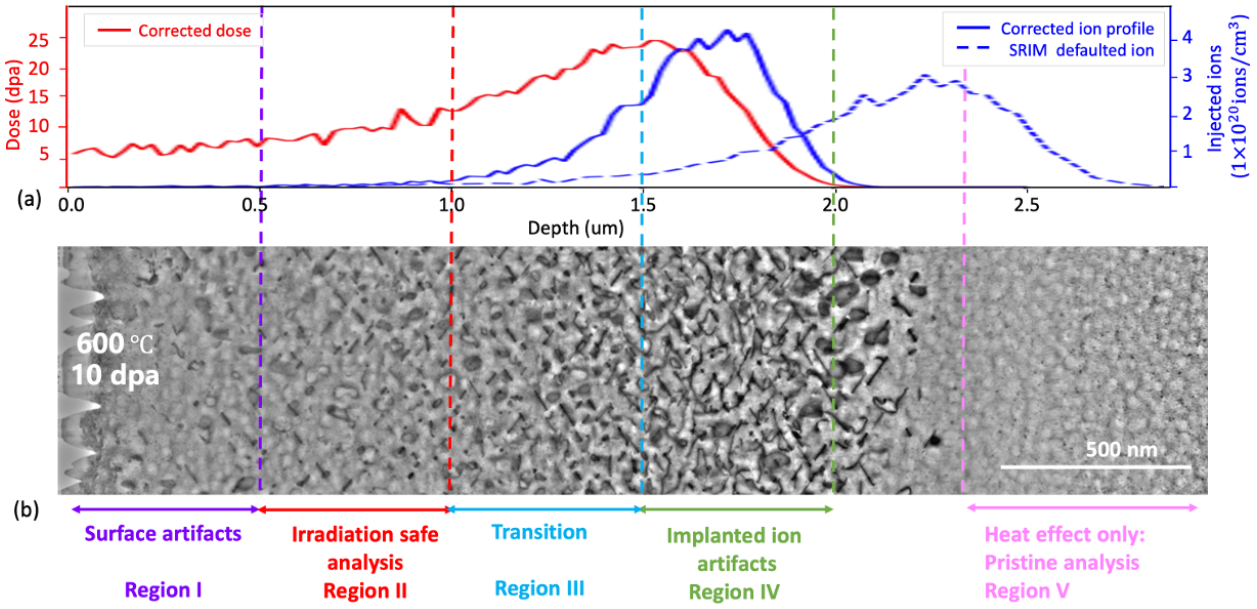


Figure 4.22: Comparison of (a) calculated SRIM profile and (b) experimental dislocation distribution of irradiated Haynes 282 (600 °C, 10 dpa).

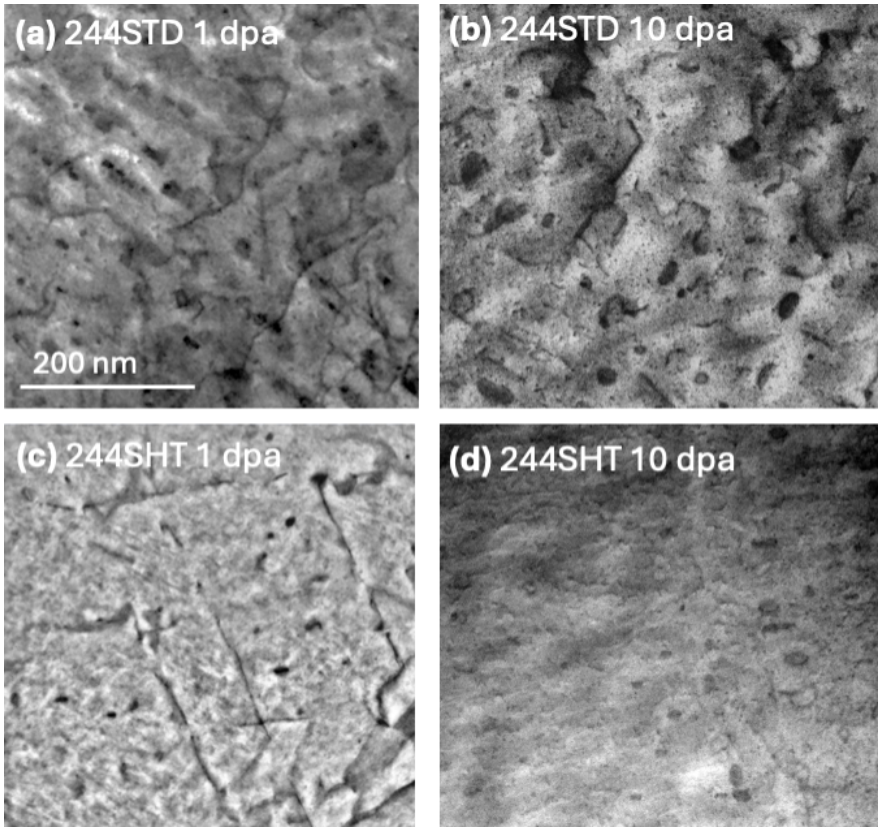


Figure 4.23: Bright-field STEM (BF-STEM) images of Haynes 244 irradiated at 600 °C: (a–b) aged STD samples and (c–d) solutionized SHT samples, with (a, c) at 1 dpa and (b, d) at 10 dpa.

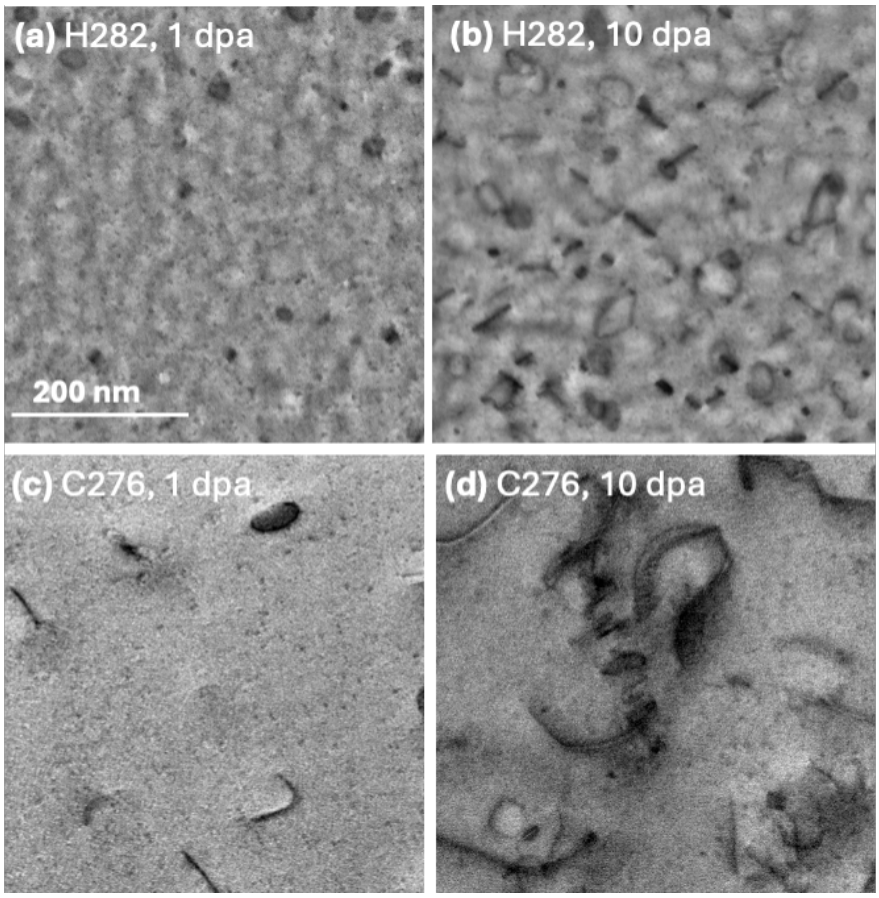


Figure 4.24: BF-STEM images of samples irradiated at 600 °C: (a–b) aged Haynes 282 and (c–d) Hastelloy C-276, with (a, c) at 1 dpa and (b, d) at 10 dpa.

Surprisingly, our observations revealed that radiation-induced dislocation loops were closely associated with or encircled the γ' precipitates in irradiated Haynes 282, as illustrated in Figure 4.25. These precipitates served as strong sinks that attracted point defects, implying that γ' precipitates can facilitate the recombination of point defects. They can also potentially trap helium atoms produced during neutron nuclear reactions in actual reactor operations and other detrimental solutes, preventing their migration toward grain boundaries. Further investigations into the interaction between precipitates and radiation-induced dislocations are required in future work.

4.2 Nanoindentation hardness

Nix-Gao fitting and the pileup correction via atomic force microscopy (AFM) are applied to get the bulk equivalent hardness. Data from the indent depth from 200 nm to 400 nm with a bilinear fitting is used to get the bulk equivalent hardness from the irradiated region, and depth from 200 to 1000 nm with a single linear fitting is used to derive the hardness of the unirradiated sample. The summary of pileup-corrected H_0 and h^* are are listed in Tables from A.5 to A.8 in the Appendix A.3.

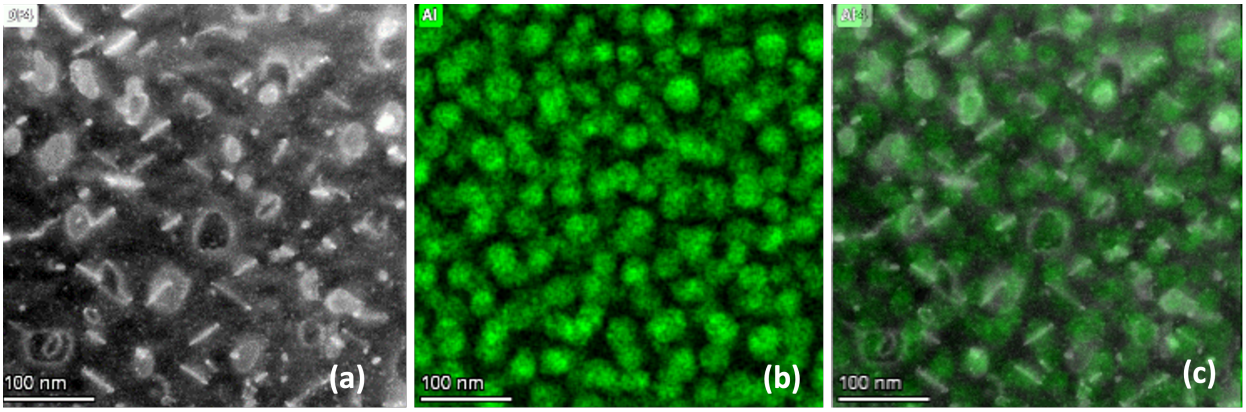


Figure 4.25: The STEM-EDS results of irradiation safe analysis region in irradiated Haynes 282 (600 °C, 10 dpa): (a) STEM dark field image, (b) aluminum (Al) elemental mapping and (c) overlapping of (a) on (b).

The hardness profile of irradiated aged Haynes 282 is illustrated in Fig.4.26(b). Only slight hardening (no statistically significant difference compared to unirradiated bulk equivalent hardness) was observed after ion irradiation.

The bulk equivalent hardness H_0 of Haynes 214, derived from pileup-corrected nanoindentation data, is presented in Fig.4.27. The H_0 of Haynes 214 gradually increased with the growth of γ' precipitates, further confirms that Haynes 214 is not suitable for long-term operation within the tested temperature range, as the continuous precipitate growth could lead to undesirable changes in mechanical properties over time.

The bulk equivalent hardness of aged Haynes 244 derived from pileup-corrected nanoindentation is plotted in Fig.4.28. Only slight softening was observed after irradiation, with no statistically significant difference in hardness compared to the unirradiated bulk sample, except in the 750 °C, 1 dpa sample. Although high-temperature thermal annealing reduced the intrinsic dislocation network density, the primary contributor to the lower hardness may be the smaller and fewer precipitates existing in this sample before irradiation due to the heterogeneous precipitate growth. Although all irradiated bulk samples were cut randomly from the same plate, it cannot be guaranteed that each sample contained an equivalent volume fraction of precipitates following the aging treatment. Overall, aged Haynes 244 demonstrated excellent stability in its mechanical properties under irradiation.

The bulk equivalent hardness of solutionized Haynes 244, derived from pileup-corrected nanoindentation data, is presented in Fig.4.29. Significant hardening was observed after irradiation in most cases, except for the 750 °C, 1 dpa sample, which remained in the solutionized state without noticeable precipitation. A detailed analysis of how microstructural evolution impacts these mechanical property changes will be provided in the next chapter.

Overall, a reduction in characteristic depths h^* was observed after irradiation, indicating diminished sensitivity to the indentation size effect in the irradiated samples. Additionally, a larger bulk-equivalent hardness H_0, corresponding to the lower h^*, was consistently observed across all selected Ni alloys, as shown in Fig.4.30.

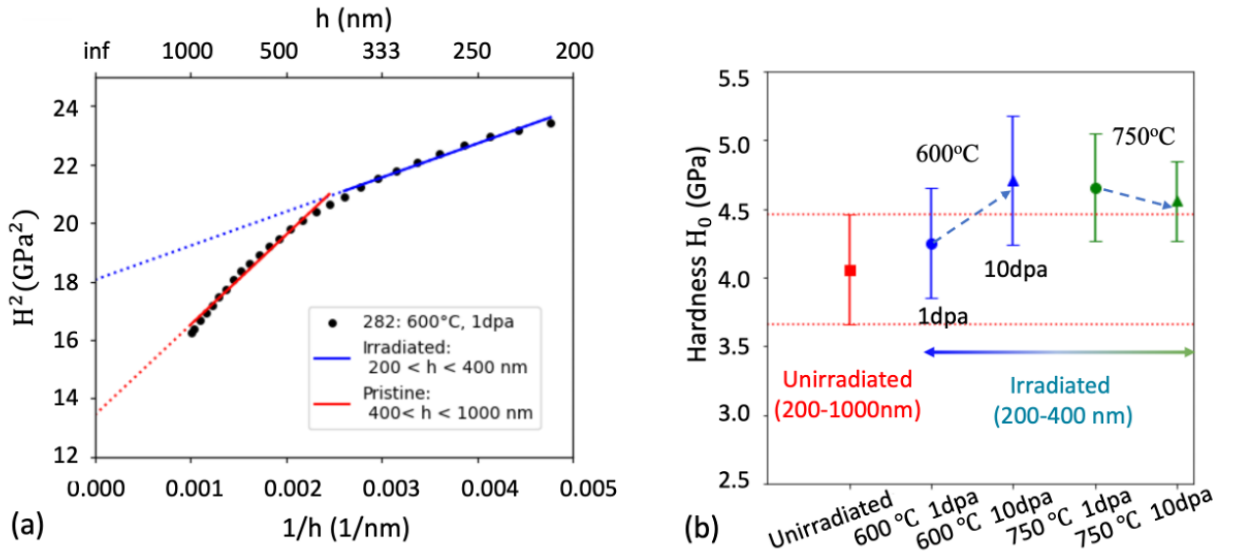


Figure 4.26: (a) An example of the Nix-Gao fitting of the depth-dependent hardness of irradiated aged Haynes 282 (600 °C, 10 dpa); (b)The bulk equivalent hardness H_0 after pileup correction of various conditions.

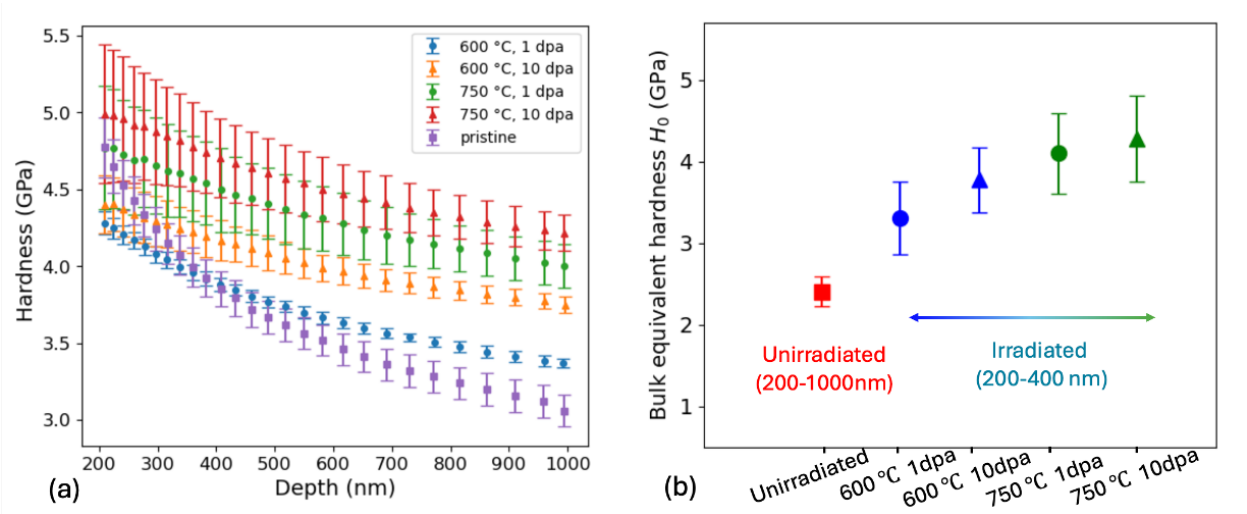


Figure 4.27: (a) Hardness vs. depth, and (b)the bulk equivalent hardness H_0 after pileup correction of Haynes 214 under various conditions.

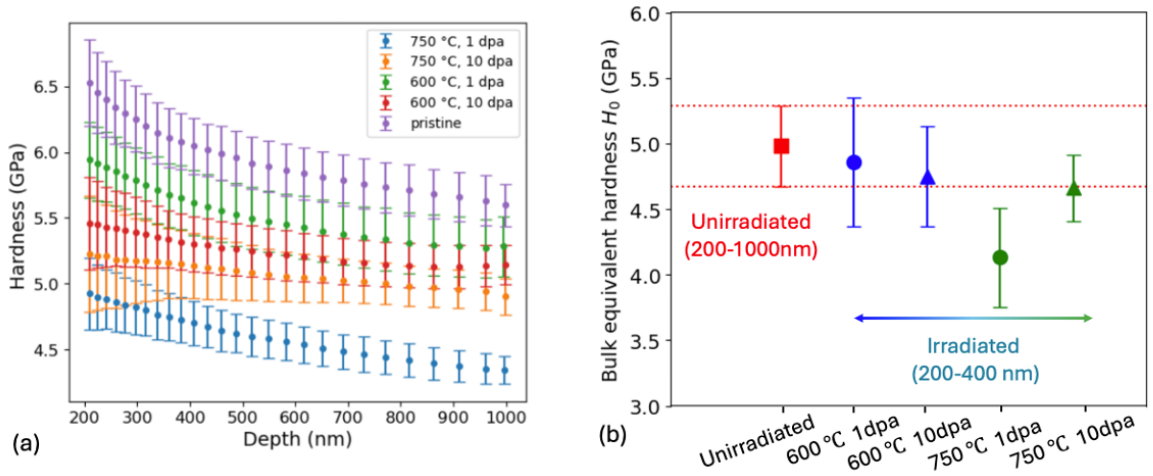


Figure 4.28: (a) Hardness vs. depth, and (b)the bulk equivalent hardness H_0 after pileup correction of Haynes 244 STD under various conditions.

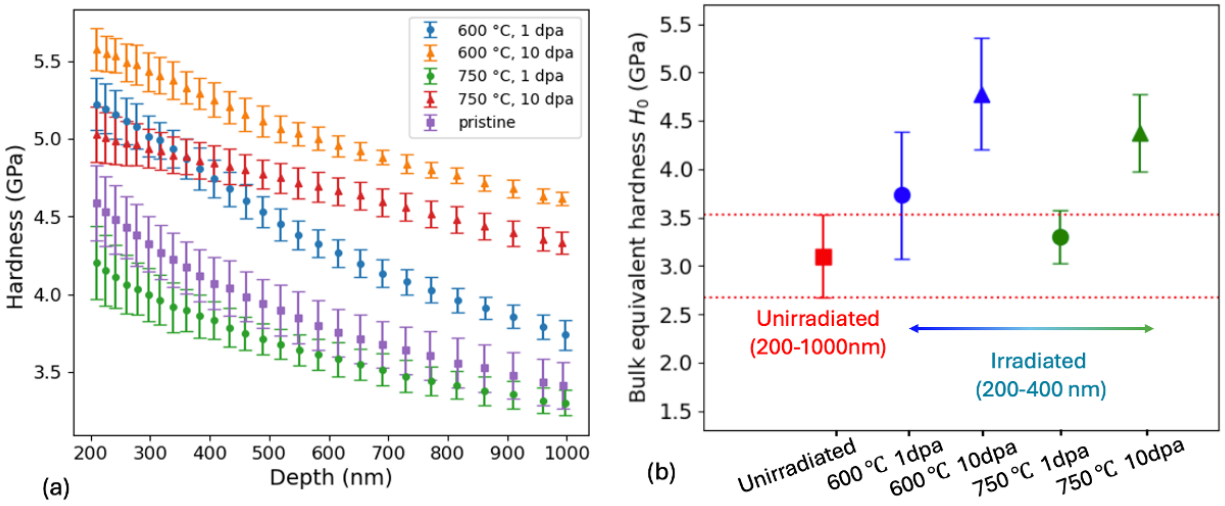


Figure 4.29: (a) Hardness vs. depth, and (b)the bulk equivalent hardness H_0 after pileup correction of Haynes 244 SHT under various conditions.

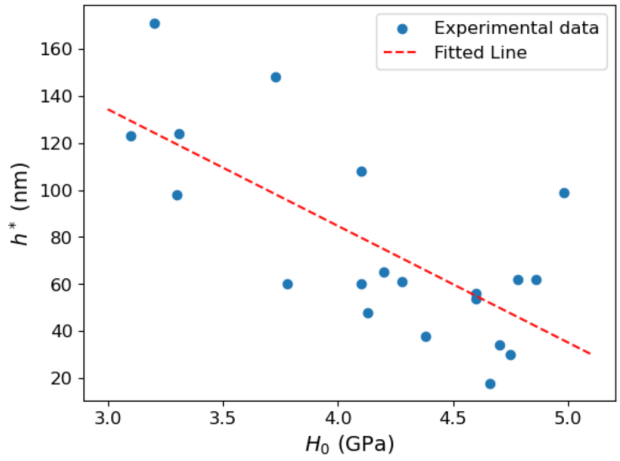


Figure 4.30: Plot of h^* values versus H_0 for all measured Ni alloys.

Chapter 5

Discussion

5.1 Correlation between microstructure and mechanical properties

Understanding the behavior of structural materials under high temperature irradiation conditions is imperative for advancing their durability and reliability of nuclear materials in the evolving landscape of nuclear reactor technologies. In this study, the microstructure is correlated to the mechanical properties obtained via the nano-hardness test on nickel-based superalloys. Tabor first proposed that a linear relationship between Vickers hardness H_V and flow stress at a strain of approximately 0.08 [78],

$$H_V = C\sigma_{0.08} \tag{5.1}$$

where $C = 2.9 - 3.0$, $\sigma_{0.08}$ and H_v are both expressed in MPa. Cahoon et.al found a good relation between 0.2% offset yield strength σ_y and hardness H for different heat treatment conditions including tempered, aged or cold worked conditions by including adjustments for strain hardening as expressed below [79],

$$\sigma_y = \frac{H_V}{C}(0.1)^n \tag{5.2}$$

Where n is the strain hardening coefficient. To determine the value of n, we utilized the experimental stress-strain data within the plastic region (strain from 2 % to 10 %) of selected nickel based superalloys [80, 81, 82], and fitted them with Equ. 5.3,

$$\sigma = K\varepsilon^n \tag{5.3}$$

where σ and ε is the true stress and true strain, respectively, and K is a constant. We employed a curve fitting technique to obtain the strain hardening coefficient, n. The n values of unirradiated materials are listed in Table. 5.1. The strain hardening coefficient typically exhibits an apparent decrease in irradiated metals from a simplistic analysis of engineering tensile stress-strain curves (particularly for irradiation temperatures below 40 % of the absolute melting temperature). However, the strain hardening coefficient obtained from true stress vs. true strain tensile curves produces a value comparable to the unirradiated n value [83, 84]. For the estimation of work hardening effects on the calculated yield strength vs the 8% flow stress corresponding to the indentation experimental conditions, we assume the value of n for the high temperature irradiation conditions is comparable to the unirradiated value if there is no apparent secondary phase changes.

An ideal geometric factor of 0.0945 exists between Vickers hardness (units of kgf/mm^2) and pileup-corrected bulk equivalent hardness H_0 obtained from Berkovich nanoindentation tests (units of MPa) [9]. Since $1kgf/mm^2$ is equal to 9.81 MPa, the ratio of the Vickers hardness to nanoindentation pileup-corrected H_0 where both hardness values use SI units (MPa) is written below:

$$H_V^{\text{nano}} = 0.927H_0 \tag{5.4}$$

Table 5.1: Key parameters of selected nickel based superalloys

	Aged Haynes 244 (STD)	Solutionized Haynes 244 (SHT)	Haynes 214	Haynes 282
Strain hardening coefficient n	0.2073 [80]	0.2495 [80]	0.2827[81]	0.1631 [82]
Shear modulus G (GPa)	85 [85]	85 [85]	83 [86]	82 [53]
Poisson's ratio	0.31 [85]	0.31 [85]	0.31	0.32 [53]
Grain size (μm)	65	200	125	65
$\sigma_{\text{grain size}}$ (MPa)	41.4	33.0	35.9	41.4

This slight difference in geometry factor is mainly due to historical reasons where Vickers hardness is based on the actual contact area of the indenter, whereas hardness is conventionally defined as the load divided by the projected contact area. In this case, we select C as 3 and apply Equ.5.2 to calculate the yield strength σ_y from the pileup-corrected bulk equivalent hardness:

$$\sigma_y = \frac{0.927 H_0}{3}(0.1)^n \tag{5.5}$$

Another method for estimating the yield strength from hardness is also based on Tabor's equation (Equ. 5.1), which corresponds to 3.27 $H_V(kgf/mm^2) = \sigma_{0.08}$ (MPa). However, the yield strength σ_y is expected to be slightly lower than 8%, with the correlation factor for σ_y and H_V being less than 3.27. After reviewing various studies on the relationship between the yield stress (MPa) vs. hardness (kgf/mm^2) with a non-zero intercept, Zhu et al. finally selected a factor of 3, which yields the corresponding relationship between the yield strength σ_y and the pileup-corrected bulk equivalent hardness H_0 as written below: [9, 87]:

$$\sigma_y = 0.285 H_0 \tag{5.6}$$

where σ_y and H_0 are both in the unit of MPa. We will compare these two equations (Equ.5.5 and 5.6) with the predicted yield strength derived from microstructure features in the later session.

This study considered strength contributions from the base metal strength (pure nickel), grain boundary strengthening, solute hardening, precipitates (including γ', Ni_2(Mo, Cr, W) and $Cr_{23}C_6$), dislocation loops, and dislocation lines. The room temperature yield strength of pure nickel σ_{Ni} is about 63 MPa [88]. The solution strengthening contribution σ_{ss} is calculated with the Equ.5.7 as written below,

$$\sigma_{ss} = \left(\Sigma k_i^2 c_i\right)^{1/2} \tag{5.7}$$

where k_i is strengthening constant, in the unit of MPa atomic fraction$^{-1/2}$, as listed in Table.5.2 [89].

Table 5.2: Strengthening constants for solution strengthening in Nickel

	Cr	Mo	W	Ti	Al	Co	Fe	C
Strength constant (MPa at.fraction$^{-0.5}$)	337	1015	977	775	225	39.4	153	1061

The calculated yield strength contribution of solution strengthening is mainly based on the nominal chemical composition of the solution annealed samples. The average grain size and corresponding yield stress increment due to Hall-Petch grain boundary hardening [90], σ_{grain}, calculated using Equ. 5.8, are listed in the Table.5.1.

$$\sigma_{grain} = 21.8 + \frac{0.158}{\sqrt{\text{grain size}}} \tag{5.8}$$

where σ_{grain} and grain size are presented in the unit of MPa and m, respectively.

For other strengthening components, the dispersed barrier hardening (DBH) model is selected to predict the yield strength increment contribution resulting from arbitrary obstacles with an average glide plane spacing of $L \sim \sqrt{Nd}$ by impeding the motion of gliding dislocations, as depicted in Equ.5.9 [91, 92].

$$\sigma_{DBH} = M\alpha Gb\sqrt{Nd} \tag{5.9}$$

where $M = 3.06$ is the Taylor factor for FCC polycrystalline metals, G is the shear modulus of the matrix as listed in Table.5.1, $b = 0.253$ nm is the glide dislocation Burgers vector magnitude[93], d and N is the diameter and the number density of defects, respectively, α is the defect barrier strength (typically from 0.25 to 1, depending on obstacle size and type [94]). The defect barrier strength of loops α_{loop} is selected from the fitting curve of the calculated size-dependent strength factor at room temperature for Frank loops [93]. The dislocation line α_{line} is set as 0.56 and replaced the $\sqrt{Nd}$ with the square root of the network density $\sqrt{\rho}$ [95].

Precipitate strengthening during dislocation-precipitate interactions in alloys is governed by two distinct mechanisms. The dislocation shearing mechanism operates for small coherent precipitates, while the Orowan mechanism dominates for larger coherent or incoherent precipitates [93]. Since γ' precipitates are fully coherent with the matrix, many previous

studies have described the dislocation-precipitate interactions in Haynes 282 as primarily following the shearing mechanism [93, 45, 96]. The yield strength increment is the combination of coherency hardening, modulus mismatch hardening, and order strengthening [96]. Tan et al. proposed the equation for the strength factor calculation as written below,

$$\alpha_{ppt}^{shearing} = \frac{0.816\gamma_{cp}d}{\mu b^2(1-0.816d\sqrt{Nd})} + 1.7\left(\frac{d}{b}\right)^{1.5}\varepsilon^{1.5} + 0.0044\left(\frac{d}{b}\right)^{1.275}\left(\frac{\Delta\mu}{\mu}\right)^{1.5} \tag{5.10}$$

where γ_{cp}, ε and $\Delta\mu$ represent the interfacial energy, lattice parameter mismatch, and shear modulus mismatch of the $\gamma-$matrix and $\gamma'-$precipitates. γ_{cp} is 0.102 J/m^2 [93]. The lattice mismatch $\varepsilon \approx 2/3\Delta a/a$ is around 0.003 at the temperature range between 600 °C and 750 °C [97]. The shear modulus of $\gamma'-$precipitates at room temperature are measured to be 79 GPa [98]. In this way, the yield strength contribution of precipitation hardening is up to 780 MPa, and the calculated $\alpha_{ppt}^{shearing}$ is 1.02 for the unirradiated, aged Haynes 282, slightly surpassing the prescribed strength factor limit of 1. Moreover, the contribution of coherency strengthening (the second term of $\alpha_{ppt}^{shearing}$) is significantly undervalued. This underestimation comes from the calculation derived from $\Delta\sigma_y^{co} = 2.6M\mu\varepsilon^{1.5}\sqrt{\frac{0.816df}{b}} = 34$ MPa. Notably, this equation is tailored for small coherent precipitates in unaged alloys. No analytical approximation of the critical resolved shear stress is available for large coherent precipitates, capable of bending the dislocation through large angles [96]. According to Fig.4.25(c), almost all of the dislocation loops are surrounding or are attached on γ' precipitates, suggesting that the Orowan mechanism is more suitable for this case. Thus, the strength contribution for large spherical precipitates is given as:

$$\sigma_{ppt}^{Orowan-spherical} = \frac{0.135M\mu b\sqrt{Nd}}{(1-\nu)^{1/2}(1-0.816d\sqrt{Nd})}\ln\left(\frac{0.816d}{r_0}\right) \tag{5.11}$$

where $\nu = 0.319$ is the Poisson's ratio [53]; r_0 is the dislocation core radius within the range $b < r_0 < 4b$, a parameter unaffected by the dislocation's surrounding environment [96]. In this study, we chose 2.5 b as the fitted core radii. The calculated yield stress contribution of γ' precipitates due to the Orowan mechanism is 653 MPa, and the corresponding barrier

strength factor is 0.84 (i.e., slightly below the Orowan limit). Thus, for the γ' precipitates in this study, the large precipitates (size > 25 nm) in Haynes 282 and 750 °C, 10 dpa Haynes 214, we select Orowan bowing mechanism to predict the yield strength contribution. In contrast, the shearing mechanism is selected for the small precipitates in other Haynes 214. However, unlike γ' precipitates, which have been extensively studied in numerous research, the investigation of Ni_2(Mo, Cr, W) precipitates is still in its early stages. Key parameters, such as interfacial energy and shear modulus mismatch, have yet to be reported. Additionally, the lattice mismatch between the FCC crystal structure and the orthorhombic crystal structure remains unexplored. Thus, we applied the Orowan bowing mechanism for all precipitates in Haynes 244, which may overestimate the yield strength contribution for those small coherent precipitates in solutionized Haynes 244 irradiated at 600 °C to a dose of 1 dpa. The yield strength contribution for large thin-plate shaped precipitates $\sigma_{ppt}^{Orowan-plate}$ is written as [93]:

$$\sigma_{ppt}^{Orowan-plate} = \frac{0.271 M \mu b A}{(1-\nu)^{1/2}(16-\pi t A)} \ln\left(\frac{0.637 D}{r_0}\right) \tag{5.12}$$

with $A = \sqrt{16\pi N D} + 4ND^2 - \pi^2 NDt$, where D and t are the diameter and thickness of the thin plate.

Zhu et al. recently noted that the traditional method of linear addition for estimating hardening changes to the unirradiated strength implicitly assumes linear superposition of the individual hardening components, which in general is an incorrect assumption. They noted that it is generally necessary to amalgamate all hardening components to accurately assess the overall strength, as opposed to only considering the change in microstructural features [87]. The proposed approach first categorizes all obstacles into weak ($\alpha < 0.25$) and strong ($\alpha > 0.25$) groups. Subsequently, a root sum square superposition method is employed for each weak and strong group, and their grouped strengths are combined using a linear superposition technique, as shown in Equ.5.13 [99, 100, 101],

$$\sigma_y = \sqrt{\sum \sigma_{\text{weak}}^2} + \sqrt{\sum \sigma_{\text{strong}}^2} \tag{5.13}$$

where σ_{weak} and σ_{strong} refer to different types of weak and strong obstacles, respectively. The base metal strength contributions from pure Ni and solid solution strengthening are categorized within the weak barrier group, and others are strong components based on their α values.

$$\sigma_{predicted} = \sqrt{\sigma_{N_i}^2 + \sigma_{ss}^2} + \sqrt{\sigma_{grain}^2 + \sigma_{ppt}^2 + \sigma_{line}^2 + \sigma_{loop}^2} \tag{5.14}$$

The detailed predicted yield strength contribution for each components and the correlation between the model-predicted yield strengths and the measured strengths derived from nanoindentation and Vickers hardness test based on the Equ.5.5 and 5.6 are shown in the following subsections.

5.1.1 Haynes 282

The detailed numerical values of measured yield strengths converted from nanoindentation are listed in Table 5.3. The major contribution to solution strengthening in Haynes 282 comes from Cr and Mo, which remained dissolved within the matrix after a two-step aging process. To calculated yield strength contribution of solution strengthening of aged samples, we simply assumed that Ti and Al atoms underwent nucleation into precipitates. Since the indentation depth of Vickers hardness is much larger than the irradiated region, Vickers hardness can only provide the measured yield strength of unirradiated Haynes 282 in the solutionized (572 MPa) and aged (847 MPa) condition, respectively, calculated with Cahoon method. As reported in the literature, the yield strength obtained from tensile tests of unirradiated annealed solutionized Haynes 282 is recorded at 384 and 605 MPa with a slight cold work hardening of 10 % [102]. The measured yield strength derived from Vickers hardness testing falls within this range. However, it is noteworthy that the yield strength measured from tensile tests of unirradiated two-step aged Haynes 282 is approximately 715 MPa [102]. This disparity may be attributed to differences in the dislocation density between our laboratory-aged samples and those processed by Haynes Inc., where the aging process was initiated immediately after solution annealing. Overall, the yield strength prediction shows good agreement with experimental data as plotted in Fig. 5.1.

Table 5.3: Summary of the strengthening contribution, the superposed model strengths, and the measured strength converted from nanoindentation results for Haynes 282

Haynes 282	Pristine SHT	Pristine aged	600 °C, 1 dpa	600 °C, 10 dpa	750 °C, 1 dpa	750 °C, 10 dpa
σ_{ss}(MPa)	313	285	285	285	285	285
σ_{weak}(MPa)	322	295	295	295	295	295
α_{ppt}		0.83	0.96	0.73	0.87	0.82
σ_{ppt}(MPa)		644	710	637	655	710
σ_{loop}(MPa)			168	351		
σ_{line}(MPa)	334	125	71		100	
σ_{strong}(MPa)	337	665	741	925	669	744
$\sigma_{predicted}$(MPa)	659	959	1036	1031	967	1013
$\sigma^{Zhu}_{measured}$(MPa)	912	1254	1322	1362	1302	1228
$\sigma^{Cahoon}_{measured}$(MPa)	679	934	985	1014	970	915

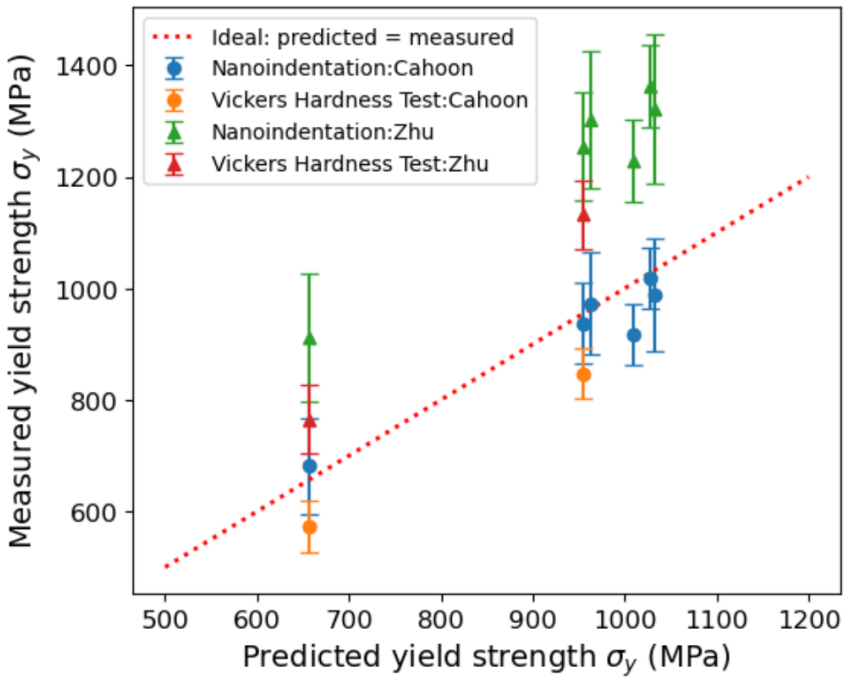


Figure 5.1: Comparison of the model-predicted strength with the measured strength converted from nanoindentation and Vickers hardness for unirradiated and ion irradiated Haynes 282.

5.1.2 Haynes 214

The detailed numerical values of measured yield strengths converted from nanoindentation are listed in Table 5.4. The primary contribution to solution strengthening in Haynes 214 comes from Al, Cr, and C. It is assumed that 20% of three elements nucleated into γ' precipitates and $Cr_{23}C_6$ during the precipitation process, based on the estimated remaining concentrations measured by atom probe tomography. As mentioned in the Results chapter for irradiated Haynes 214, no dislocation loops were observed in the irradiation-safe analysis region. The radiation-induced supersaturation of vacancies likely promotes vacancy-atom exchange diffusion of Al, rather than being captured by loops. High number density of $Cr_{23}C_6$ carbides were only observed in 750 °C, 1 dpa sample. The aligned thin-plate model was applied due to the blocky shape of carbides, and the yield strength increment due to the carbide is 381 MPa with the obstacle strength α value of 0.55. Currently we calculate the yield strength increment separately for dislocation lines and carbides, which may lead to an overestimation, as the carbides are attached to the dislocation lines. Haynes 214 is a strain-rate sensitive material [81]. In this case, we chose an n value of 0.2827, derived from the true stress-strain curve tested at room temperature with a strain rate of 0.01 /s [81], which corresponds to the closer strain rate used in the nanoindentation test (0.05 /s).

Aside from the 750 °C, 1 dpa sample, another significant discrepancy between the predicted yield strength and the value measured via nanoindentation using the Cahoon method occurred at 750 °C, 10 dpa, as shown in Fig.5.2 in the Appendix A.3. This discrepancy may be attributed to the large uncertainty in nanoindentation at shallow indent depths in this sample, as illustrated in Fig. 4.27 (a). Moreover, one reported values for the critical parameters, the interfacial energy γ_{cp} between γ and γ', varies from 0.0089 J/m^2 [103] to 0.154 J/m^2[104]. This wide range can lead to substantial differences in yield strength predictions. For example, using a low interfacial energy value of 0.0089 J/m^2, the strength factor of precipitates in irradiated samples was less than 0.25, except in the case of the 750 °C, 10 dpa sample (0.36), where the strengthening effects are significantly underestimated. Another concern is the difference in n values between the solution-annealed and aged conditions, while no stress-strain curve is available for the aged Haynes 214. This

Table 5.4: Summary of the strengthening contribution, the superposed model strengths, and the measured strength converted from nanoindentation results for Haynes 214

Haynes 214	Pristine	600 °C, 1 dpa	600 °C, 10 dpa	750 °C, 1 dpa	750 °C, 10 dpa
σ_{ss}(MPa)	162	160	160	148	160
σ_{weak}(MPa)	177	176	176	165	176
α_{ppt}		0.27	0.38	0.44	0.84
σ_{ppt}(MPa)		362	570	427	798
σ_{line}(MPa)	140			296	
σ_{strong}(MPa)	172	376	579	652	863
$\sigma_{predicted}$(MPa)	349	553	755	817	1040
$\sigma^{Zhu}_{measured}$(MPa)	687	943	1077	1168	1220
$\sigma^{Cahoon}_{measured}$(MPa)	388	533	609	661	690

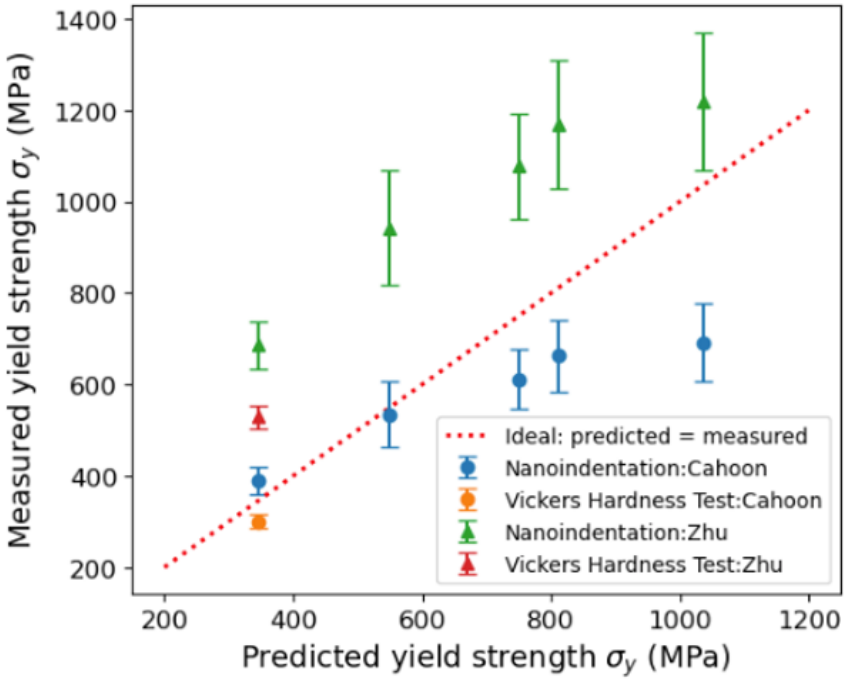


Figure 5.2: Comparison of the model-predicted strength with the measured strength converted from nanoindentation and Vickers hardness for unirradiated and ion irradiated Haynes 214.

absence of a more suitable n value could partly explain the larger discrepancy between the measured and predicted values at higher hardness levels—essentially, in conditions with a high detected volume fraction of precipitates.

5.1.3 Haynes 244

The detailed numerical values of measured yield strengths converted from nanoindentation of Haynes 244 STD are listed in Table 5.5.The main solid-solution strengthening element in Haynes 244 is Mo. According to the atomic concentration of Mo in the matrix measured by the STEM-EDS, 80 % to 90 % Mo remained within the matrix after aging treatment. Thus, we assume that 20 at.% Mo atoms nucleate into the precipitates. Since no distinct difference in the Mo concentration was observed between the irradiated and pristine regions, the yield strength increment due to solid-solution strengthening in Haynes 244 (STD) is consistently estimated at 408 MPa. The strength factor of Ni_2(Mo, Cr, W) precipitates were 1.27 and 1.09 in the pristine and 600 °C, 1 dpa samples, respectively, using with the aligned thin-plate model. However, the maximum allowable strength factor is one (impenetrable Orowan obstacle). Thus, in this study, we use the calculated strength factor when the α value is less than 1; otherwise, we we set the strength factor to 1. Unlike Haynes 282 and 214, where the yield strength derived from bulk-equivalent hardness using the Cahoon method closely aligns with predictions, the Zhu method appears to be more suitable in this case as shown in Fig. 5.3. However, the 0.2 % yield stress of aged Haynes 244 is reported to be 836 MPa tested at room temperature with a strain rate of 10^{-4} /s [80], which is lower than both the predicted value and the yield strengths derived using either Cahoon's or Zhu's method. One possible explanation is that the contribution from the precipitates may have been overestimated. Figure. 5.4 shows an example of patchy contrast in precipitates of aged Haynes 244, which might suggest a complex internal structure of precipitates. Currently, we consider the Ni_2(Mo, Cr, W) as non-shearable large particles and estimate the stress increment using the Orowan bowing mechanism. However, the regions highlighted in yellow rectangles in Fig. 5.4 suggest that dislocations may be shearing through the precipitates in these areas. This indicates that Ni_2(Mo, Cr, W) precipitates might be shearable and the strength factor would be lower than the values calculated using the Orowan mechanism.

Table 5.5: Summary of the strengthening contribution, the superposed model strengths, and the measured strength converted from nanoindentation results for aged Haynes 244

Haynes 244 STD	Pristine STD	600 °C, 1 dpa	600 °C, 10 dpa	750 °C, 1 dpa	750 °C, 10 dpa
σ_{ss}(MPa)	408	408	408	408	408
σ_{weak}(MPa)	415	415	415	415	415
α_{ppt}	1	1	0.73	0.61	0.97
σ_{ppt}(MPa)	850	799	354	286	735
σ_{loop}(MPa)		136	192		
σ_{line}(MPa)	664	731	560	516	381
σ_{strong}(MPa)	1084	1096	698	600	835
$\sigma_{predicted}$(MPa)	1499	1511	1113	1015	1250
$\sigma^{Zhu}_{measured}$(MPa)	1419	1385	1328	1177	1328
$\sigma^{Cahoon}_{measured}$(MPa)	955	932	893	792	893

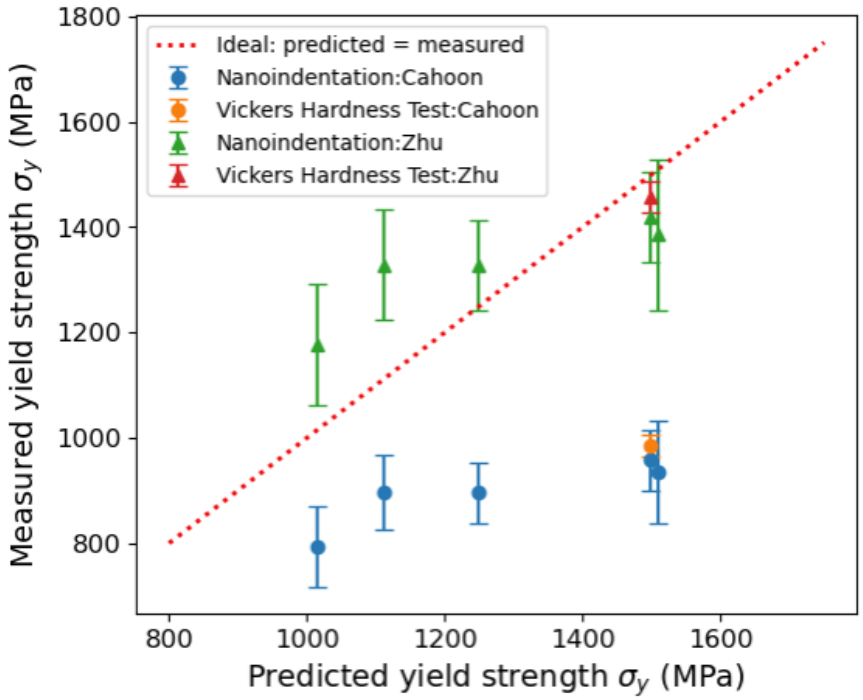


Figure 5.3: Comparison of the model-predicted strength with the measured strength converted from nanoindentation and Vickers hardness for unirradiated and ion irradiated aged Haynes 244.

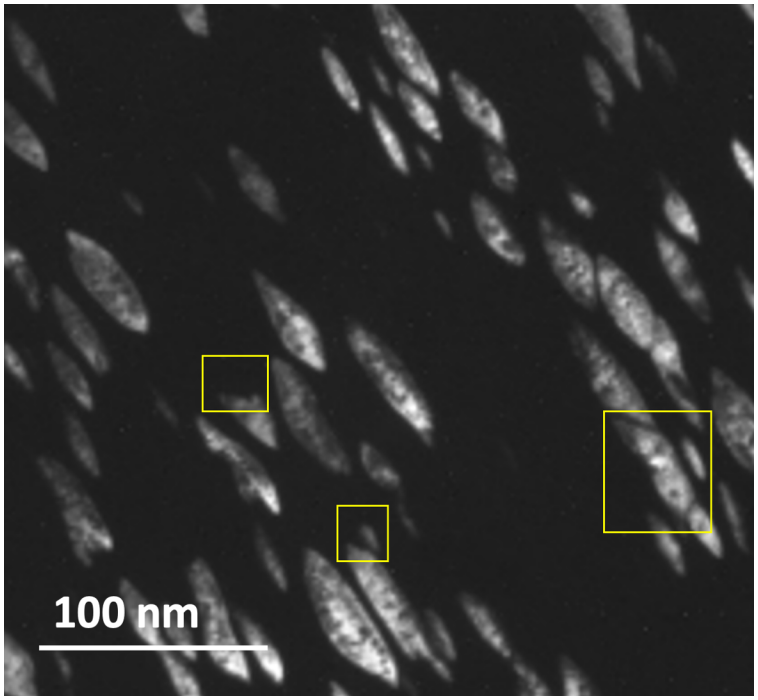


Figure 5.4: Dark field image of aged Haynes 244 along the [001] zone axis. The yellow rectangles highlight regions where dislocation shearing may have occurred.

The detailed numerical values of measured yield strengths converted from nanoindentation of Haynes 244SHT are listed in Table 5.6 and the correlation between the model-predicted yield strengths and the measured strengths derived from nanoindentation and Vickers hardness tests are plotted in Fig.5.5. Since many precipitates grew during the irradiation, we only apply n = 0.2495 for solid-solution condition samples (unirradiated and 750 °C, 1 dpa). Other samples are used with n = 0.2073 as aged samples. The yield strength derived from Vickers hardness using Cahoon's method is 360 ± 18 MPa, which is close to the reported 0.2 % yield stress tested at room temperature with a strain rate of 10^{-4} /s [80]. However, the prediction for solutionized Haynes 244 with precipitation growth during irradiation is more challenging. As mentioned in the results section, the tiny precipitate size, which is close to the limit of TEM resolution, makes it difficult to accurately measure the precipitate number density and area ratio using TEM images. Therefore, the correction based on the assumed area ratio of 0.3 in the pristine region is not applicable to solution-annealed Haynes 244. Moreover, significant variations in precipitate size and number density were observed across different grains, especially in the 600 °C, 10 dpa sample. The strength factor

Table 5.6: Summary of the strengthening contribution, the superposed model strengths, and the measured strength converted from nanoindentation results for solutionized Haynes 244 SHT

Haynes 244 SHT	Pristine SHT	600 °C, 1 dpa	600 °C, 10 dpa	750 °C, 1 dpa	750 °C, 10 dpa
σ_{ss}(MPa)	441	408	408	441	408
σ_{weak}(MPa)	445	413	413	445	413
α_{ppt}		0.55	0.81		1
σ_{ppt}(MPa)		576	895		681
σ_{loop}(MPa)		65	43		
σ_{line}(MPa)	77	354			
σ_{strong}(MPa)	123	686	901		688
$\sigma_{predicted}$(MPa)	568	1099	1314	541	1100
$\sigma^{Zhu}_{measured}$(MPa))	883	1063	1362	940	1254
$\sigma^{Cahoon}_{measured}$(MPa)	539	717	919	574	866

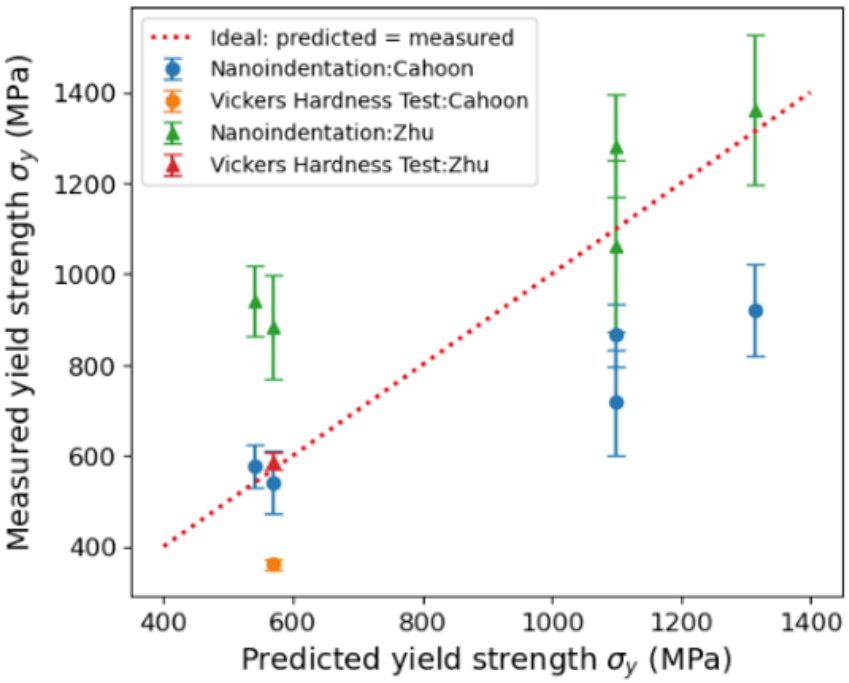


Figure 5.5: Comparison of the model-predicted strength with the measured strength converted from nanoindentation and Vickers hardness for unirradiated and ion irradiated solutionized Haynes 244.

ranged from 0.54 to 1, resulting in yield strength contributions varying from 301 MPa to 994 MPa. In this study, we use the average precipitate size and number density to correlate with the macro-scale mechanical properties. We must admit that a large discrepancy in the yield strength increment could not be avoidable due to the heterogeneous precipitate distribution. Moreover, when the precipitate size is small, precipitates could be sheared by the dislocations. The critical diameter of the thin-plate-shaped particles, at which maximum strengthening, ranges from 8 nm to 30 nm [105]. Thus, the dislocation-precipitate interaction mechanism could change under different irradiation conditions. For 750 °C, 10 dpa, which precipitate sizes are close to those in the standard aged samples. The uncertainty discussed about the Haynes 244 STD also exists. Although Zhu's method looks fit more like Haynes 244 STD, it could be caused by the overestimated prediction values.

In this study, we investigated four sets of samples and compared the predicted yield strength values from microstructural analysis with the derived yield strength from mechanical testing. We found that the Cahoon method aligns well when the predicted values are lower, while Zhu's method is closer to higher predicted values. The Cahoon method is highly dependent on the strain hardening coefficient (n), which varies with different strain rates or testing methods (e.g., quasi-compressive vs. tensile testing [106, 107]). On the other hand, Zhu's method is more straightforward and works effectively when the material is near a fully work-hardened condition. However, the yield strength may be overestimated if the material has yet to undergo complete work hardening. Further research is needed to fully understand the applicability and limitations of these two methods across different conditions.

5.2 Phase stability and precipitate size prediction under irradiation conditions

5.2.1 γ' precipitates

The present study has led to new findings showing the remarkable stability of γ' precipitates in the Haynes 282 nickel-base superalloy and a strong precipitation tendency in Haynes 214 under ion irradiation at high temperatures to 750 °C.

In the past few decades, many studies have been carried out regarding the irradiation stability of γ' precipitates, which are the primary strengthening source in many commercial nickel-based superalloys. In general, it is observed that γ' disordering and/or ballistic dissolution occurs below a critical temperature and above a threshold dose. For example, it was reported that γ' precipitates became completely disordered in Inconel 718 for doses around 0.6 dpa subjected to mixed irradiation with high energy protons and spallation neutrons below 72 °C [108] and γ' precipitates completely dissolved after a dose of 10 dpa at room temperature under heavy ion irradiation [43]. Below 250 °C, the superlattice reflection of γ' precipitates in the electron diffraction pattern disappeared after 3 dpa doses, and the precipitates partially dissolved in irradiation to 10 dpa dose [43, 109, 110]. The reported critical temperature of ordering/disordering $T_c^{o/d}$ varies from 267 to 500 °C [43, 44]. Meanwhile, an early study on 5 MeV Ni ion irradiated Inconel X-750 reported γ' precipitates disordering still occurred at temperatures as high as 550-650 °C after 2 dpa [111]. Thus, the $T_c^{o/d}$ greatly depends on the dose rate, chemical composition of the matrix, Ti/Al ratio of precipitates, precipitate size, and the degree of coherency of precipitates [44, 43, 5, 45, 46]. Above $T_c^{o/d}$, the irradiated precipitates typically display a steady state of partial disordering, where the intensity of superlattice reflection is slightly reduced compared with the initial unirradiated state, but the superlattice spots do not disappear, regardless of the increasing doses. Moreover, helium atoms were reported to have a positive effect on retarding the disordering and dissolution process of γ' and γ'' precipitates in Inconel 718 subjected to irradiation with 3.5 MeV Fe^+ and 370 keV He^+ at 200 °C [112]. During Fe ion irradiation at 1 dpa, the superlattice diffraction spots of γ' and γ'' precipitates vanished. The precipitates lost coherency, and no clear precipitate shapes could be observed in centered dark field images. In contrast, under He irradiation at doses up to 10 dpa, the superlattice of precipitates maintained slight intensity and precipitates only partially dissolved back into solution [110]. Similarly delayed disordering of γ' precipitates was observed in Inconel X-750 subjected to simultaneous dual-beam irradiation of helium and nickel self-ions at 400°C [113]. When helium atoms trap vacancies and form cavities, more interstitials survive the annihilation and promote a dynamic reordering process. Dual-beam conditions (combining helium and heavy ions) are more relevant for neutron irradiation than single heavy ion irradiation

conditions. The enhanced reordering contributes to improved stability of precipitates in dual-beam scenarios, highlighting the potential of γ' precipitates in practical applications within nuclear reactor environments. In Fig.4.25, it is evident that dislocation loops surround the γ' precipitates, suggesting such precipitates possess strong sink strength. Helium atoms produced via (n,α) reactions are likely to be trapped by the γ' precipitates, preventing the migration of helium atoms towards grain boundaries. The complex synergistic relationship between helium and precipitates will be explored in future research. At temperatures ranging from 513 to 636 °C, pre-existing γ' precipitates in Ni alloy PE 16 underwent redistribution towards sinks, such as dislocation network, leading to the formation of a skeletal structure of γ' under fast neutron irradiation in EBR-II [39, 5]. Comparable findings of initial γ' precipitates redistribution were observed in Ni-Al alloys when exposed to irradiation with Ni ions, at 550 °C with a dose rate of 10^{-2} dpa/s [5]. Large pre-existing γ' (25 nm) dissolved, and new γ' precipitates nucleated on a very fine scale, ultimately reaching uniform size across all precipitates. Conversely, γ' precipitates kept good stability at 500 °C under 1 MeV Kr^{+} ion irradiation with a dose rate of 0.001 dpa/s [44]. The γ' precipitates in a $FeCoNiCrTi_{0.2}$ high entropy alloy irradiated with 6.4 MeV Fe^{3+} ions to ∼5 dpa were fully disordered at 400-500 °C and partially disordered at 600 °C. Some solute mixing was observed at the precipitate-matrix interface but overall the precipitate size and density were stable [**?**]. In Fe-Cr-Ni alloys, γ' precipitates also exhibited notable stability at 593 °C under fast neutron irradiation up to $1.7 \times 10^{22} n/cm^2 (\sim 8\text{dpa})$, while a propensity for cellular-shaped precipitate transformation spherical shape emerged under 3 MeV Ni-ion irradiation at 750 and 600 °C with a dose rate of 0.005 dpa/s up to 100 dpa. In our studies of Haynes 282 exposed to $\sim 10^{-3}$ dpa/s Ni ion irradiation at 600°C or 750°C, no discernible dissolution or redistribution of γ' precipitates was evident.

5.2.2 Ni_2(Mo, Cr, W) precipitates

It is reported that that the long-range ordered Ni_2(Mo, Cr) phase homogeneously precipitates within the matrix of Hastelloy C-276, without preferential precipitation at the grain boundaries, at temperatures ranging from 300 °C to 650 °C [114]. However, in this study, no such precipitation was observed within the matrix, which is consistent with some previous

studies, such as the absence of a hardening phase in Hastelloy C-276 after 240 hours of aging treatment [115]. Gdowski et al. also suggested that the critical temperature of transformation from short range to long range in this alloy is about 600 °C [116, 77]. Below the critical transformation temperature, ordering occurs prior to the precipitation of intermetallic phases. Interestingly, Ni_2(Mo, Cr) does precipitate in Hastelloy C-22HS, whose nominal composition is Ni-21Cr-17Mo (wt%), closely resembling the Hastelloy C-276 with Ni-16Cr-16Mo(wt%). A high number density of Ni_2(Mo, Cr) precipitates were produced during the two-step aging process, including 705 °C/16 hours/furnace cooling and 605 °C/32 hours/air cooling [117]. Pai et al. provided a prediction for the solvus temperature T_f of Ni_2(Mo, Cr) phase in Ni_2(Mo, Cr) alloys, given by the equation $T_f = 625.8 + 217.4x_{Mo/Cr} - 70x^2_{Mo/Cr}$, where x is the Mo/Cr ratio and T_f is in the unit of °C. Following this equation, T_f^{22HS} is 707.7 °C and T_f^{C-276} is 723.9 °C, where Hastelloy C-276 even has a higher solvus temperature of Ni_2(Mo, Cr) phase. Considering that the highest temperature for formation of Ni_2(Mo, Cr) is about 37 °C lower than its solvus temperature [118], Ni_2(Mo, Cr) is likely to be formed at 600 °C. In addition to the Mo/Cr ratio, the total atomic fraction of Mo and Cr, denoted as X_{Cr+Mo}, matters. According to TEM observations, the formation boundary of Ni_2(Mo, Cr) precipitates in Ni_2(Mo, Cr) alloys shifts with changes in X_{Cr+Mo}[119]. The upper limit of formation temperature rises with the increasing X_{Cr+Mo}. For Hastelloy C-276, where the X_{Cr+Mo} is 29.8 at%, the formation boundary corresponds to around 635 °C [119]. This temperature exceeds the current irradiation temperature of 600 °C, not to mention that there also exists 1.4 at% of W, which can substitute for Mo, potentially forming Ni_2(Mo, Cr, W) precipitates. W substitution may increase both the formation temperature and solvus temperature. Thus, some other factors might impact the ordering mechanism in Ni-Cr-Mo alloys, leading to the low transition of Hastelloy C-276, and needs more investigation. Given that the potential for this phase to be vulnerable to stress corrosion cracking, induce notable lattice distortion, and generate significant internal stresses that negatively affect mechanical properties, Hastelloy C-276 demonstrates superior metallurgy stability compared to many other Ni-Cr-Mo alloys, such as Haynes 242 [54], Haynes 244 [120], Hastelloy N [121] under high temperature with/without irradiation exposure.

5.2.3 μ phase and Mo-enriched carbides

In Hastelloy C-276, M_6C carbides are highly prone to form over a broad temperature range, from 550 °C to 870 °C, even within a short duration, such as just 10 minutes at 870 °C [75, 122, 123, 124]. μ phase requires relatively higher temperature (more than 650 °C for precipitation) [124, 115, 77]. Typically, both carbides and μ phase initially nucleate heterogeneously at grain boundaries, forming discrete precipitates. As time progresses, a continuous layer forms along grain boundaries, with the precipitates growing perpendicular to the boundary. Over prolonged exposure, μ phases further intermix with carbides within the matrix. In this study, we only observed the Mo-enriched precipitation along some grain boundaries and the matrix remained disorder γ phase.

According to the simplified diffusion controlled precipitate growth, the particle size can be predicted by the following equation [125, 126]:

$$r \simeq \beta\sqrt{Dt} \tag{5.15}$$

Where β is the growth rate coefficient, correlated to the difference of solute concentration in precipitate and matrix, we simply consider it a constant; D is the diffusivity of Mo, and t is diffusion time. Under the thermal aging condition, the thermally activated diffusivity of Mo in Ni, D_{th}^{Mo}, can be written in the form of the Arrhenius equation $D_{\mathrm{th}}^{Mo} = D_0^{Mo} \exp\left(-\frac{Q^{Mo}}{k_{\mathrm{B}}T}\right)$, where D_{th}^{Mo} and Q^{Mo} is the diffusion pre-factor and diffusion activation energies of Mo in Ni, respectively. The detailed relevant parameters are listed in Table. 5.7.

Liu reported the presence of the μ phase and M_6C phase within the matrix at 700 °C after 2160 hours of thermal exposure [122]. Similarly, Hodge noted the formation of both phases at 800 °C after 100 hours of aging [124]. Akhter observed the μ phase within the grain at 850 °C after just 5 hours [115]. The values of $\sqrt{Dt}$ are all within the same range, varying from 2.6×10^{-7} to 5.6×10^{-7} m. Although we can only estimate the diffusivity of Mo solutes within the matrix and are unable to simulate the nucleation of secondary phases at the grain boundaries during the early stages, the simplified model still shows good agreement with experimental observations. This suggests that the model effectively captures the critical diffusion behaviors and can be used to estimate the precipitation time by diffusivity, even

Table 5.7: Material parameters related diffusivity used in this work

Parameters	Value	Reference
Activation energy of Ni self-diffusion, Q^{Ni}	2.91 eV	[127, 42]
Ni self-diffusion pre-factor, D_0^{Ni}	$0.92 \times 10^{-4} m^2/s$	[127, 42]
Lattice parameter of Ni, a_0	0.352 nm	[42]
Boltzmann constant, k_B	8.617×10^5	
Attempt frequency for vacancy exchange, μ_0	$0.5 \times 10^{13}/s$	[42]
Geometrical correlation factors of vacancies, f_v	0.78	[51, 42]
Annihilation radius for vacancies/interstitial at sinks, $r_{vs} = r_{is}$	a_0	[51, 42]
I-V recombination radius, r_{iv}	$1.94a_0$	[128]
Vacancy migration energy in Ni, E_{mv}^{Ni}	1.04 eV	[129]
Vacancy formation energy in Ni, E_{fv}^{Ni}	1.79 eV	[129]
Interstitial migration energy in Ni, E_{mi}^{Ni}	0.14 eV	[130]
Interstitial formation energy in Ni, E_{fi}^{Ni}	4.69 eV	[130]
Activation energy of Mo thermal activated diffusion in Ni, Q^{Mo-Ni}	3.13 eV	[131]
Pre-factor of Mo diffusion in Ni, D_0^{Mo-Ni}	$4.32 \times 10^{-4} m^2/s$	[131]

without accounting for more complex nucleation processes. Under the irradiation conditions, the total diffusivity D^* can be calculated using the equation provided below,

$$D^* = D_{\text{mix}} + D_{\text{red}}^{Mo} + D_{\text{th}}^{Mo} \tag{5.16}$$

where diffusivity due to atomic mixing $D_{\text{mix}} = 1/12 a_0^2 \eta K$ [132, 3], the lattice parameter of matrix is $a_0 = 3.572 \mathring{A}$ [42], K denotes the dose rate (10^{-3} dpa/s), and η is the replacement per displacement atomic mixing constant (RPA) derived from experimental data or MD simulations, set to a value of 100 for our heavy ion irradiation conditions [133].

According to the point defect balance equations [3], the vacancy concentration C_v^{rad} at steady state can be expressed as follows,

$$C_v^{rad} = \sqrt{\frac{K_0 D_i}{K_{iv} D_v} + \frac{D_i^2 S^2}{4 K_{iv}^2}} - \frac{D_i S}{2 K_{iv}} \tag{5.17}$$

Where K_0 denotes the effective point defect production rate. For those materials irradiated at temperatures where vacancies are mobile, the thermally-activated correlated defect recombination corrections to DPA (CRC-DPA) should be employed as the parameter

for assessing defect production [134], leading to $K_0 = 0.1K$ in this case. The vacancy diffusion coefficient $D_{\mathrm{v}} = a_0^2 \upsilon_0 \exp\left(-E_{\mathrm{mv}}^{Ni}/k_B T\right)$, where υ_0 denotes the vacancy jump frequency, E_{mv}^{Ni} represents the vacancy migration energy [42], and k_B is the Boltzmann constant. The interstitial diffusion coefficient D_{v} is calculated in the same way. K_{iv} denotes the interstitial-vacancy recombination rate coefficient, $K_{iv} = 4\pi r_{iv} (D_{\mathrm{i}} + D_{\mathrm{v}})$, where r_{iv} is the spontaneous recombination radii of Frenkel pairs in Ni. S denotes sink strength. In this case, S is $1.5 \times 10^{13}/m^2$ in Hastelloy C276 prior to the irradiation.

The irradiation enhanced diffusivity of Mo in Ni matrix, D_{rad}^{Mo}, can be treated as [135],

$$D_{red}^{Mo} = D_{th}^{Mo} \frac{C_v^{rad}}{C_v^{eq}} \tag{5.18}$$

where C_v^{eq} is the concentration under thermal equilibrium condition.

The calculated diffusion coefficients of Ni in aged Haynes 282 under thermal and 10^{-3} dpa/s self-ion irradiation are plotted in Fig.5.6. The total diffusivity coefficients are $2.76 \times 10^{-18}\,\mathrm{m}^2/\mathrm{s}$ and $1.33 \times 10^{-17}\,\mathrm{m}^2/\mathrm{s}$, at temperatures of 600 °C and 750 °C, respectively. The corresponding pure thermal diffusivity is $3.70 \times 10^{-22}\,\mathrm{m}^2/\mathrm{s}$ and $1.64 \times 10^{-19}\,\mathrm{m}^2/\mathrm{s}$, respectively. This suggests that the radiation-enhanced diffusion is predominant at both temperatures and could help accelerate the diffusion-controlled precipitate growth. Using Equation 5.15 and Liu's data (700 °C, 2160 hours) as a reference, since 700°C falls within the irradiation temperature ranges, the equivalent times for μ phase and/or M_6C precipitates to form in the matrix are calculated to be 20.8 hours at 600 °C and 4.3 hours at 750 °C, which explains why no precipitation was observed within the grains during the up-to-160-minute high-temperature irradiation in this study.

5.2.4 Models to predict precipitate evolution under irradiation

5.2.4.1 Modified NHM Model

The Nelson-Hudson-Mazey (NHM) model is widely used to predict precipitate stability by assessing radiation-induced dissolution and radiation-enhanced diffusion [5]. However, the original NHM model exhibits limitations, including overestimating the solute concentration

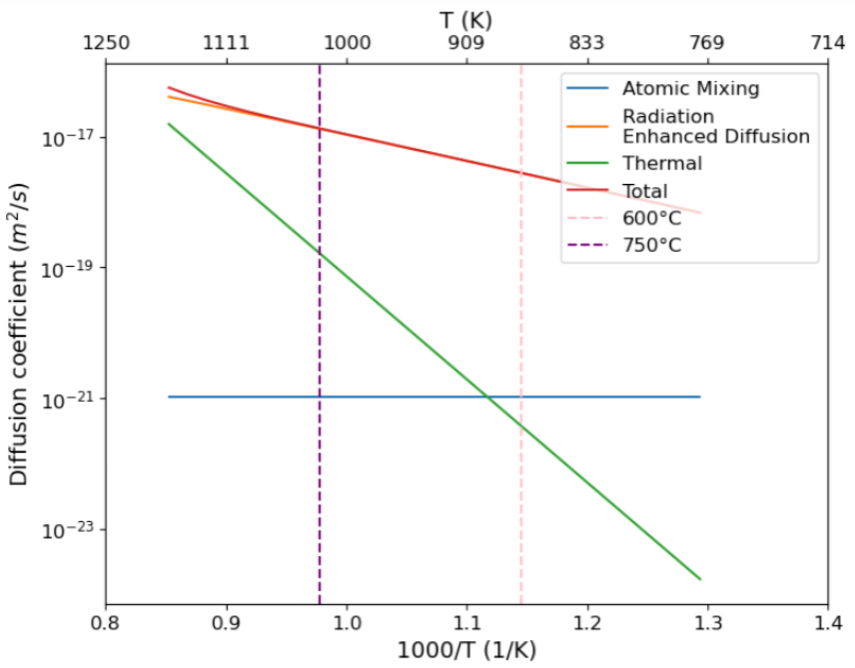


Figure 5.6: The diffusion coefficients for Mo in Ni matrix under Ni ion irradiation at a steady state are presented as functions of reciprocal temperature, considering a damage rate of 10^{-3} dpa/s.

within matrix and the steady-state vacancy concentration. Addressing these shortcomings, Zhao et al. proposed science-based modifications to the NHM model, leading to more accurate estimations of precipitate size evolution under particle irradiation [136]. The modified equations for precipitate growth and dissolution are written in Equ.5.19 and Equ.5.21, respectively.

$$\frac{dV}{dt} = 4\pi D_{red} cr/p \tag{5.19}$$

where $\frac{dV}{dt}$ is the volume changing rate. D_{red} is the radiation enhanced diffusivity of solute. r is the precipitate radius. c and p is the atomic fraction of solute in the matrix and precipitates, respectively. The boundary condition of constant solute concentration is:

$$p \times \frac{4}{3}\pi r^3 n + c \times \left(1 - \frac{4}{3}\pi r^3 n\right) = C \tag{5.20}$$

where n is the number density of precipitates and C is the total solute concentration.

$$\frac{dV}{dt} = -\frac{4\pi r^2 \phi}{N_{at}} \tag{5.21}$$

where N_{at} is the atomic density of the matrix sample.The recoil flux of solute atoms from precipitates to matrix ϕ can be approximated as $f_m K$, where f_m is the multiplication factor (in the magnification of $10^{16} - 10^{17}$atoms/cm^2) [136]. K is the dose rate of 0.001 dpa/s. The disordering dissolution, where each cascade intersection with the surface leads to the dissolution of a volume of precipitates, is neglected in Equ.5.21. Overall, the revised equation to calculate the changing rate of precipitate radius is written below [136].

$$\frac{dr}{dt} = -\frac{f_m K}{N_{at}} + \frac{D_{red} C}{rp} \times \frac{3}{3 - 4\pi n r^3} - \frac{Dred}{rp} \times \frac{4\pi r^3 np}{3 - 4\pi r^3 n} \tag{5.22}$$

One of the main limitations of the NHM model is that it does not account for changes in precipitate number density during growth. As a result, it is not well-suited for cases where precipitates grow through Ostwald ripening. To address this, we began with aged Haynes 282, which contains some large precipitates and exhibits a relatively stable number density unaffected by irradiation. The γ' precipitates are enriched in Al and Ti. Although precipitate growth is diffusion-controlled and governed by the slowest element, Al and Ti have comparable diffusivities in Ni [137]. Therefore, Ti diffusivity is selected as the representative value. The solute concentration in the matrix C and the atomic concentration of solute in precipitate p are 0.057 and 0.25, respectively, representing the combined concentrations of Al and Ti atoms. Since the diffusion pre-factor D_0^{Ti-Ni} and activation energy Q^{Ti-Ni} of Ti solutes in Ni matrix may vary depending on the Al/Ti ratio and total concentration, we chose the values most closely matching the composition of Haynes 282, where D_0^{Ti-Ni} and Q^{Ti-Ni} are $3.9 \times 10^{-4} m^2/s$ and 2.37 eV [137], even though the diffusivity changes due to composition is relatively small.

After a two-step aging process before the radiation, the radius and number density of γ' precipitates in Haynes 282 is 14.5 nm and $5.1 \times 10^{21}/m^3$. TEM observations revealed that irradiation did not significantly alter the size or number density of the γ' precipitates. As shown in Fig. 5.7, the precipitate size remained unchanged under pure thermal exposure at 600 °C. However, under thermal exposure at 750 °C for 10,000 seconds (approximately

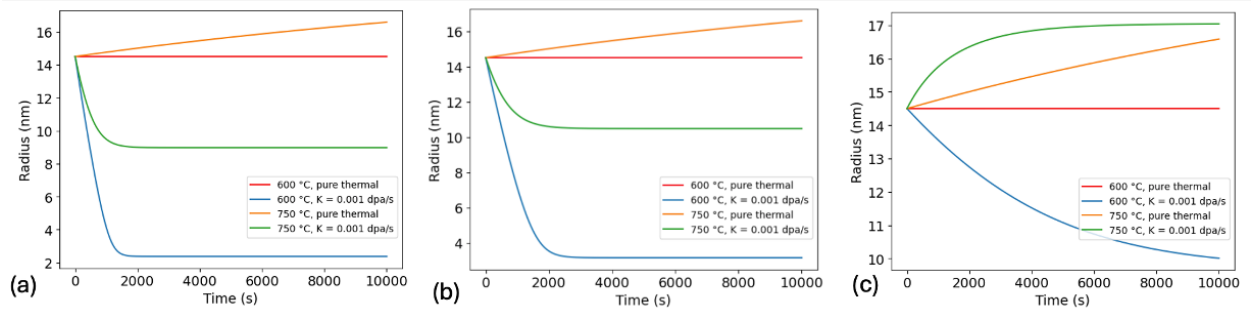


Figure 5.7: Calculated γ' precipitate radius as a function of time in Haynes 282 at 600 and 750 °C with different ballistic dissolution factor: (a) $f_m = 1.17 \times 10^{17} atoms/cm^2 \times dpa$, (b) $f_m = 8 \times 10^{16} atoms/cm^2 \times dpa$, and (c) $f_m = 1.4 \times 10^{16} atoms/cm^2 \times dpa$.

167 minutes), the precipitate radius increased to 16.6 nm. However, the precipitate size dramatically decreased under ion irradiation if we first chose f_m as $1.17 \times 10^{17} atoms/cm^2 \times dpa$ as the ballistic dissolution factor [136] as shown in Fig.5.7(a). The final simulated precipitate radii for 10 dpa samples were 2.4 nm and 9.0 nm for 600 °C and 750 °C, separately, suggesting that the ballistic mixing effect may be overestimated at this f_m value. By adjusting the ballistic dissolution factor to $f_m = 0.8 \times 10^{17}$ atoms/cm^2·dpa, as recommended for recombination-dominant conditions [136], the final precipitate radii increased to 3.3 nm and 10.6 nm for 600 °C and 750 °C with doses to 10 dpa, respectively. In contrast, using $f_m = 1.4 \times 10^{16} atoms/cm^2 \times dpa$, the corresponding radii was 10.0 nm and 17.0 nm for the same temperatures and dose. Regardless of the selected ballistic dissolution factor, the simulated precipitate radius under 600 °C irradiation appears under-estimated, probably due to the underestimated Ti diffusivity. The Ti diffusion pre-factor and activation energy were based on testing results between 900 and 1200 °C, which may not fully cover the lower temperature behavior [137].

The standard aged Haynes 244 has a disk-shaped, while the modified NHM model only works for the spherical particles. Thus, we calculated the equivalent radius r_{eq} using the Equ. 5.23, as written below:

$$r_{eq} = \frac{\pi}{4} d^2 t \tag{5.23}$$

where d and t are the diameter and thickness of the Ni_2(Mo, Cr, W) precipitates, separately. The equivalent radii before irradiation is 27.4 nm. The Mo concentration was 22 at.% (p)and 15.5 at.% (C) within precipitates and matrix, respectively. We tested the different

Table 5.8: Summary of TEM results and NHM simulated precipitate size in aged Haynes 244 under different irradiation conditions

			Irradiated region		Pristine region	
			600 °C, 10 dpa	750 °C, 10 dpa	600 °C, 10 dpa	750 °C, 10 dpa
TEM		Diameter (nm)	52.1	61.7	59.0	72.7
		Thickness (nm)	23.1	17.1	17.4	15.7
		Equivalent radius (nm)	22.7	23.0	22.5	24.9
NHM Simulation	$f_m = 0$				27.4	33.8
	$f_m = 1.4 \times 10^{16}$		31.8	37.7		
	$f_m = 8.0 \times 10^{16}$		17.4	26.0		
	$f_m = 1.17 \times 10^{17}$		13.8	22.2		

ballistic dissolution factors and listed the corresponding equivalent radii in the Table. 5.8. As mentioned in the results for aged Haynes 244, the 750 °C, 1 dpa sample is notably distinct from the others. Excluding this sample, the equivalent average precipitate radius under pure thermal exposure ranged from 22.6 nm to 27.9 nm based on TEM observations. In contrast, the simulated equivalent precipitate radius under 750 °C thermal exposure for 10,000 seconds reached 33.8 nm, which is larger than the TEM data, as shown in Fig. 5.8. This suggests that the solute diffusivity of Mo at 750 °C could be slightly overestimated. As reported in [136], using a ballistic dissolution factor of $f_m = 1.4 \times 10^{16} atoms/cm^2 \times dpa$ leads to overestimated steady-state radii in ion-irradiated conditions, while $f_m = 1.17 \times 10^{17} atoms/cm^2 \times dpa$ neglects in-cascade recombination, resulting in smaller precipitate sizes. The factor $f_m = 8 \times 10^{16} atoms/cm^2 \times dpa$ appears to fit both aged Haynes 244 and Haynes 282 best. Moreover, the actual growth of Ni_2(Mo, Cr, W) precipitates in a Ni matrix may encounter varying strain fields, suggesting that assuming spherical, isotropic growth might not be suitable for Haynes 244. The precipitate growth rate term in the modified NHM model could be refined to account for the precipitate shape in future study, as described by Ham's mechanism [125].

5.2.4.2 LSW model

One of the main limitations of the NHM model is that it cannot adjust the number density of precipitates during their growth, making it particularly unsuitable for cases where nucleation is a key factor. This limitation becomes especially problematic when dealing with solution-annealed samples, e.g., Haynes 214, that start without existing precipitates. We observed a

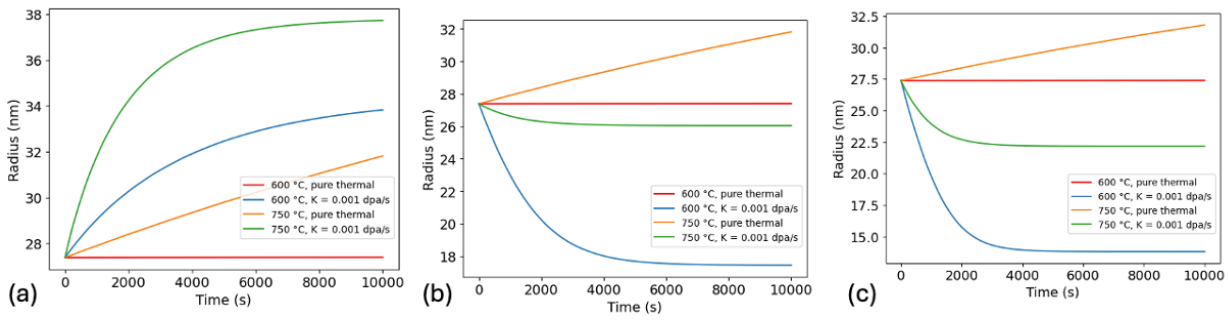


Figure 5.8: Calculated Ni_2(Mo, Cr, W) precipitate radius as a function of time in Haynes 244 STD at 600 and 750 °C with different ballistic dissolution factor: (a) $f_m = 1.17 \times 10^{17} atoms/cm^2 \times dpa$, (b) $f_m = 8 \times 10^{16} atoms/cm^2 \times dpa$ and (c) $f_m = 1.4 \times 10^{16} atoms/cm^2 \times dpa$.

higher number density but smaller γ' precipitates in Haynes 214 irradiated at 750 °C with a dose of 1 dpa, compared to the 10 dpa sample. This phenomenon, known as Ostwald ripening, involves the growth of larger precipitates at the expense of smaller ones. It typically occurs when a secondary phase nucleates and grows from a supersaturated solution, leading to coarsening over time. Lifshitz, Slyozof, and Wagner (LSW) developed the theory of Ostwald ripening [138, 139]. Many researchers kept developing based on LSW theory and extended the theory to non-zero volume fraction Q. The corresponding growth law follows [140]:

$$R(t) = \left[R^3(0) + K(Q)t\right]^{1/3} \tag{5.24}$$

where $R(0)$ represents the average radius of the spherical precipitates at the onset of coarsening, while $R(t)$ denotes the average radius as a function of time t during the coarsening process. $K(Q)$ is the coarsening rate, which increases monotonically with the volume fraction Q [140]. In this study, we utilize a modified version of the Lifshitz-Slyozov-Wagner (LSW) theory, known as the LSEM model, which has been validated as a good fit for the experimental particle size distribution of γ' precipitates in Ni-Co-Al alloys [141, 103]. The primary distinction between LSW theory and LSEM lies in the treatment of particle interactions. LSW theory assumes that particles remain fixed in space and grow independently. In contrast, LSEM allows for the possibility of particle encounters and coalescence due to diffusion fields, leading to a more dynamic interaction between particles during coarsening.

The coarsening rate constant K(Q) of LSEM is written as:

$$K(Q) = \frac{6\gamma_{cp}\Omega C_e D_{eff}\bar{r}'^3}{R_B T Y} \tag{5.25}$$

where γ_{cp} is the interfacial energy, equal to 0.102 J/m^2 [93] for γ' precipitates. Ω is the molar volume of precipitates, $6.85 \times 10^{-6} m^3/mol$, derived from the lattice parameters. C_e is equilibrium concentration of solute within the matrix. D_{eff} is the effective solute diffusivity, which changes with the sink strength from the growing precipitates. $R_B = 8.3135 J/(mol \cdot K)$ is the ideal gas constant. $\bar{r}'$ and Y are the parameters obtained from the LSEM analysis, depending on the volume fraction. The default value K(0) is determined by $\bar{r}' = 1$ and $Y = \frac{27}{4}$ when the volume fraction is zero [140]. The $K(Q)$ value is then selected based on the plotting of the function of the ratio of $K(Q)/K(0)$ with Q, as reported in the ref.[140].

If we simply assumed that D_{eff} is not related to the precipitate radius and considering the dissolution term from the NHM model, the precipitate radius evolution rate of the modified LSEM model is written below derived from Equ.5.24 and 5.25,

$$\frac{dR}{dt} = -f_m K \Omega + \frac{K(Q)}{3R^2} \tag{5.26}$$

For Haynes 214, the solute concentration of Al away from precipitates was about 0.08, measured by APT analysis. The diffusion pre-factor D_0^{Al-Ni} and activation energy Q^{Al-Ni} of Al solutes in Ni matrix was $2.3 \times 10^{-4} m^2/s$ and 2.31 eV [137]. $R(0)$ set as 0.1 nm. Although the observed volume fraction for 600 °C samples varies from about 1% to 5% under TEM observation, we assume a single volume fraction—the largest observed at that temperature—for each case. For 600 °C, the volume fraction Q is taken as 5 %, with the corresponding ratio of K(Q)/K(0) being 1.1. Similarly, for 750 °C, Q is assumed to be 10 %, with the corresponding K(Q)/K(0) ratio being 1.3. We selected $f_m = 8 \times 10^{16} atoms/cm^2 \times dpa$ as the ballistic dissolution in all analyses. If we use $f_m = 1.17 \times 10^{17} atoms/cm^2 \times dpa$, the predicted precipitate growth rate under pure thermal diffusion would exceed that under irradiation, which contradicts our experimental observations.

The detailed comparison between the TEM observation and modified LSEM prediction data about precipitate size and number density is listed in Table.5.9 and plotted in Fig. 5.9.

Table 5.9: The detailed comparison of precipitate size and number density between TEM observation and modified LSEM model in irradiation Haynes 214

Sample	Region	Diameter (nm)		Number density ($10^{22}/m^3$)	
		TEM	LSEM	TEM	LSEM
600 °C, 1 dpa	irradiated	10.4	56.4	4.1	0.05
	pristine	9.1	4.1	3.1	132.8
600 °C, 10 dpa	irradiated	13.0	92.7	4.2	0.01
	pristine	8.6	8.9	6.5	13.3
750 °C, 1 dpa	irradiated	16.7	19.3	1.4	2.6
	pristine	11.8	18.6	1.5	3.0
750 °C, 10 dpa	irradiated	29.1	43.6	0.8	0.2
	pristine	27.1	40.0	0.7	0.3

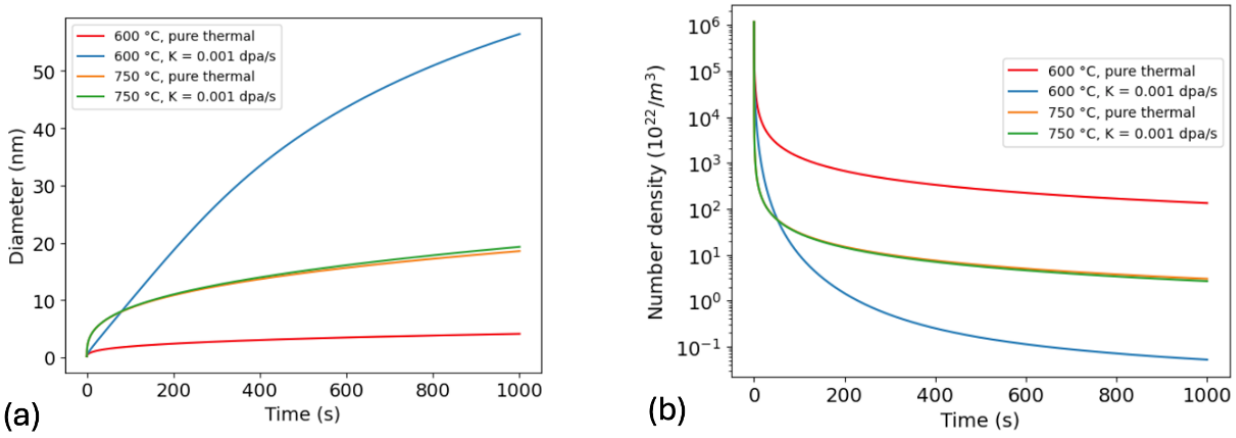


Figure 5.9: Calculated (a) diameters and (b) number density of γ' precipitate as a function of time in Haynes 214 at 600 °C and 750 °C

Verifying the kinetics of Ostwald ripening is always a challenging task, primarily because the theory is based on small volume fractions, which are difficult to accurately assess using TEM or other techniques. In the current simulation, the input volume fraction does not match the observed values from TEM analysis. The most significant deviation was noted in the irradiated region of 600 °C sample, where the simulated precipitate diameter was much larger than the TEM observations, while the number density was approximately two orders of magnitude higher than what was measured.

The relationship between simulated precipitate size and diffusivity over time for the 600 °C, 1 dpa sample is depicted in Fig. 5.10. A significant jump in precipitate size is observed due to the overestimated diffusivity from using the steady-state vacancy concentration at the beginning of irradiation. The current simulation setup has almost no nucleation period, which contradicts real-world conditions. Although the simulated size and number density deviate from the experimental data and the coarsening onset is too simplified, the overall precipitate growth rate remains slower than that predicted by the modified NHM model, as shown in Fig. 5.11. Unlike the LSEM model, the input number density for the modified NHM model is based on the final experimentally observed TEM data. It only takes 99 seconds for precipitates in irradiated Haynes 214 at 750 °C to reach the steady state diameter of the precipitate of 45 nm. While this restricted number density results in a predicted precipitate size relatively close to the experimental data, it remains about two times larger than the actual observed size.

Both the NHM model and the LSEM demonstrate limitations in accurately predicting precipitate evolution. Further modifications are needed to refine these models, or alternative approaches may need to be explored to improve the accuracy of precipitate growth predictions under such conditions. Due to the poor predictive performance of the modified LSEM model for the uniformly distributed spherical γ' precipitates in Haynes 214, no further predictions are made for solutionized Haynes 244, where requires a long time nucleation period. The Ni_2(Mo, Cr) precipitates exhibit a broad size distribution and non-spherical shapes, which further complicates the modeling process. Given the limitations of the LSEM model in handling such complex precipitate morphologies, its use in this context likely results in inaccurate predictions.

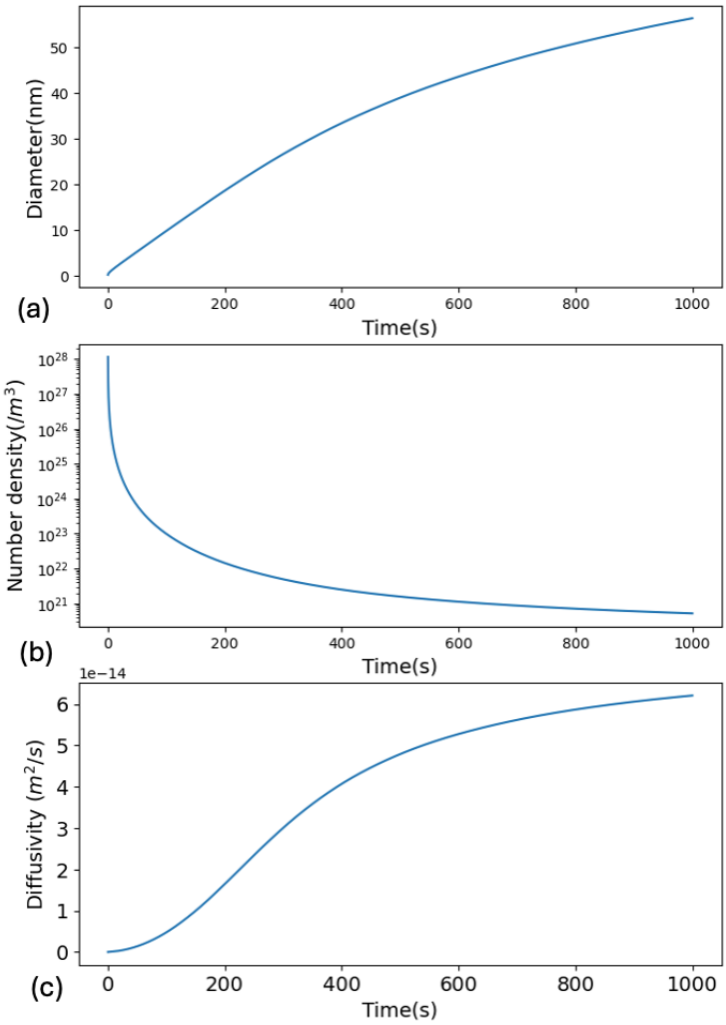


Figure 5.10: (a) Diameter, (b) number density of precipitates, and (c) diffusivity of Al solutes in Haynes 214 600 °C, 1 dpa sample, simulated by the modified LSEM model with a time step of 0.001 seconds.

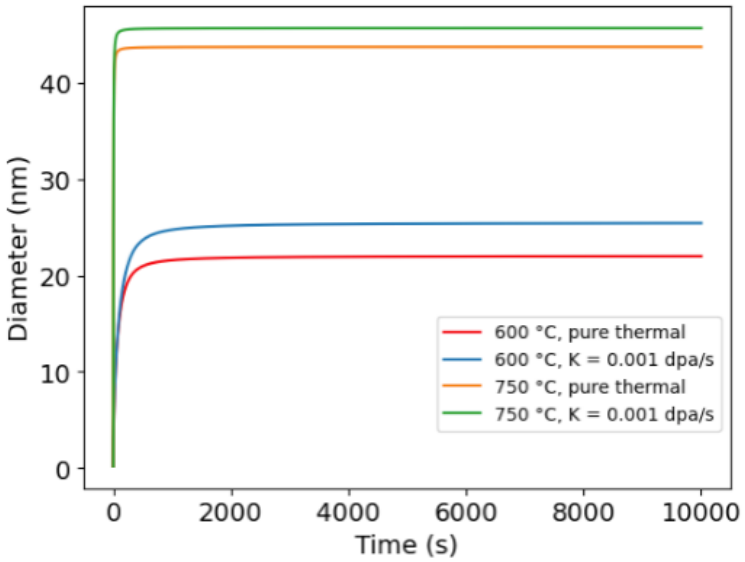


Figure 5.11: The γ' precipitate diameter as a function of time in Haynes 14 at 600 and 750 °C, simulated by the modified NHM model.

Chapter 6

Conclusions

This study delves into understanding the effects of alloy processing on the microstructure evolution and hardness changes of Ni-based superalloys (NBS) subjected to ion irradiation at different temperatures and doses. Our research goals encompass (1) investigating phase instabilities in extreme irradiation environments, (2) establishing correlations between yield strength predictions based on microstructure evolution and hardness measurements.

We have chosen several high-performance commercial Ni-base superalloys for this research, including solid solution-strengthened Haynes 244, Haynes 214, Hastelloy C-276, and precipitation-strengthened Haynes 244, and Haynes 282. The key observations and conclusions are listed below.

- The precipitation-strengthened Haynes 282 showed remarkable radiation resistance and thermal stability at 600 °C and 750 °C. No statistical difference in size and number density of $\gamma' - Ni_3(Al, Ti)$ precipitates was observed after irradiation. Radiation-induced dislocation loops only appeared in the 600 °C irradiation conditions. Implanted ions enhanced the growth of $1/3 < 111 >$ type loops and facilitated more $1/2 < 011 >$ type loop evolution into dislocation tangles. Despite dislocations being strong obstacles that impede dislocation movements and increase the sample hardness, γ' precipitates remained the primary strengthening source in irradiated Haynes 282.

- The primary strengthening phase in Haynes 244 alloys is $Ni_2(Mo, Cr, W)$, which is a long-range-ordered metastable phase with a Pt_2Mo type orthorhombic crystal

structure. Size correction was applied to the pristine precipitates, although the difference between the corrected and uncorrected values was relatively small compared to the standard deviation. After reviewing all data on Haynes 244, an assumption was made that the area ratio of all variants occupies approximately 30 % of the total image area in the aged Haynes 244 samples. This assumption was used to estimate the total number density of precipitates observed from STEM-EDS or TEM-DF images, providing a more comprehensive view of precipitate distribution and number density across the sample. Such precipitates are sensitive to both radiation damage and thermal effects. At 600 °C, Ni_2(Mo, Cr, W) precipitates in pre-aged samples partially dissolved or shrunk at low doses and completely dissolved in the implanted ion region. In contrast, at 750 °C, Ni_2(Mo, Cr, W) precipitates in the aged sample exhibit great stability, maintaining consistent size and number density after irradiation. For solid solution treated Haynes 244, the Ni_2(Mo, Cr) grew in both irradiation mid-range safe analysis regions and pristine regions subjected to long time high temperature exposure except for 750 °C, 1 dpa sample. The precipitates in the irradiated region are relatively sparse yet larger in size. Due to the slow diffusion rate of W, unlike the pre-aged samples, no W segregation was observed in precipitates in the solutionized samples. Interestingly, no precipitates were observed between 1.35 μm and 1.85 μm from the surface. The complex interactions among ballistic mixing, radiation-enhanced precipitation, and implanted ion effect need more investigation.

- $\gamma' - Ni_3Al$ precipitates were found to grow in both irradiated and pristine regions in Haynes 214. In contrast to the absence of precipitation in the ion-implanted region of solutionized Haynes 244, the γ' precipitates remained distributed in this region, though their number density was lower compared to other regions under 600 °C irradiation. Interestingly, no such depth-dependent statistical differences in size or number density were observed under 750 °C irradiation. Radiation-induced dislocation loops and networks were only observed in the implanted regions of the 600 °C samples. Dense intrinsic dislocation lines, likely originating from mechanical polishing, were solely observed in the unirradiated sample and the sample irradiated at 750 °C with a dose

of 1 dpa. A high number density of $Cr_{23}C_6$ carbides was exclusively observed in the irradiated region of the 750 °C, 1 dpa sample. These carbides are likely attached to the dislocation lines.

- No precipitation of Ni_2(Mo, Cr), μ phase, and Mo-enriched carbides were observed within the matrix of Hastelloy C-276. Due to the absence of precipitates as competitors, dislocations evolved more rapidly, forming larger loops and dislocation tangles. Although some precipitates nucleated at the grain boundaries, less element segregation at grain boundaries suggests that ballistic mixing makes the precipitate more uniform within the matrix. Given that the potential secondary phases in the matrix would increase the potential of stress corrosion cracking and negatively affect mechanical properties, Hastelloy C-276 demonstrates superior metallurgy stability compared to other Ni-Cr-Mo alloys under high temperatures with/without irradiation exposure.

- The superposition method and dispersed barrier hardening model were applied to predict the yield strength increment from various obstacles in the material. Two methods were used to derive the yield strength from nanoindentation hardness: Tan's method, which performed well when the hardness was low, and Zhu's method, which gave closer predictions to experimental data as the hardness increased or approached work-hardening conditions. Several key hyper-parameters significantly impacted the prediction accuracy, including the strain work hardening coefficient, shear modulus mismatch, and interfacial energy between the precipitates and the matrix. Overall, the yield strength predictions showed acceptable agreement with experimental data. However, further validation is required using additional data to verify the conversion model from hardness to yield strength.

- The modified NHM model and the Ostwald ripening LSEM model were employed to predict precipitate evolution under thermal exposure and irradiation conditions. A critical factor in these predictions is solute diffusivity. However, the available data on solute diffusivity in Ni-based matrices is limited, particularly at temperatures much below the solvus temperature. The pre-diffusion factor and activation energy reported in different studies vary significantly, sometimes resulting in more than two orders

of magnitude difference in calculated diffusivity. The modified NHM model performs well for samples with 'mature' pre-existing precipitates, where the number density remains relatively stable over time. However, for solution-annealed samples subjected to irradiation, the model struggles. The final density observed through TEM often significantly differs from the actual number density in the early stages of irradiation, causing the precipitates to grow too quickly and prematurely reach the steady-state size. This discrepancy highlights the need for improved modeling approaches or additional experimental data to capture precipitate evolution in such cases accurately. The modified LSEM model accounts for changes in the number density of precipitates during the growth period due to coalescence. However, overestimating the number density—resulting from assuming a fixed volume fraction—leads to excessively high solute diffusivity and unrealistic precipitate growth rates in the early stages. A more carefully tuned precipitate radius at the onset of coarsening is needed to improve accuracy. Other LSW models that can handle non-spherical precipitates should be explored, as they may offer a more realistic depiction of precipitate evolution, especially in alloys with complex precipitate morphologies.

[1] TT Claudson et al. Irradiation effects on high-temperature reactor structural metals, astm stp. *American Society for Testing and Material*, 380:156–170, 1965. xi, 6, 7

[2] KR Williams and SB Fisher. The void swelling of a γ-hardened alloy. *radiation effects*, 15(3-4):243–250, 1972. xi, 9, 10

[3] Gary S Was. *Fundamentals of radiation materials science: metals and alloys*. springer, 2016. xi, 12, 13, 84

[4] DS Gelles. *An Example of Precipitate Stability in Reactor-Irradiated Nimonic PE16*. ASTM International, 1979. xi, 13

[5] RS Nelson, JA Hudson, and DJ Mazey. The stability of precipitates in an irradiation environment. *Journal of Nuclear Materials*, 44(3):318–330, 1972. xi, 11, 12, 14, 15, 80, 81, 85

[6] O Tissot, Cristelle Pareige, E Meslin, B Décamps, and J Henry. Influence of injected interstitials on α precipitation in fe–cr alloys under self-ion irradiation. *Materials Research Letters*, 5(2):117–123, 2017. xi, 16, 17, 57

[7] Jie Song, Robert Field, Amy Clarke, Yao Fu, and Michael Kaufman. Variant selection of intragranular ni2 (mo, cr) precipitates (γ) in the ni-mo-cr-w alloy. *Acta Materialia*, 165:362–372, 2019. xii, 20, 21

[8] Ryuta Kasada, Yoshiyuki Takayama, Kiyohiro Yabuuchi, and Akihiko Kimura. A new approach to evaluate irradiation hardening of ion-irradiated ferritic alloys by nano-indentation techniques. *Fusion engineering and design*, 86(9-11):2658–2661, 2011. xii, 27, 28

[9] Pengcheng Zhu, Yajie Zhao, Shradha Agarwal, Jean Henry, and Steven J Zinkle. Toward accurate evaluation of bulk hardness from nanoindentation testing at low indent depths. *Materials & Design*, page 110317, 2021. xii, 29, 66, 67

[10] Kwadwo Kese and Zhi-Cheng Li. Semi-ellipse method for accounting for the pile-up contact area during nanoindentation with the berkovich indenter. *Scripta materialia*, 55(8):699–702, 2006. xii, 29

[11] Arthur F Rowcliffe, Louis K Mansur, David T Hoelzer, and Randy K Nanstad. Perspectives on radiation effects in nickel-base alloys for applications in advanced reactors. *Journal of Nuclear Materials*, 392(2):341–352, 2009. 1, 2, 3, 5, 6, 10, 11

[12] RM Boothby. Radiation effects in nickel-based alloys. 2012. 1, 2, 3, 4, 8, 9

[13] Thomas M Angeliu, John T Ward, and Jonathan K Witter. Assessing the effects of radiation damage on ni-base alloys for the prometheus space reactor system. *Journal of nuclear materials*, 366(1-2):223–237, 2007. 1, 6, 10

[14] Y Dai, GR Odette, and T Yamamoto. 1.06-the effects of helium in irradiated structural alloys. *Comprehensive Nuclear Materials*, 1:141–193, 2012. 2

[15] SJ Zinkle and LL Snead. Opportunities and limitations for ion beams in radiation effects studies: Bridging critical gaps between charged particle and neutron irradiations. *Scripta Materialia*, 143:154–160, 2018. 2, 15, 16, 57

[16] Michael G Fahrmann, S Krishna Srivastava, and Lee M Pike. Haynes 244 alloy–a new 760 c capable low thermal expansion alloy. In *MATEC Web of Conferences*, volume 14, page 17004. EDP Sciences, 2014. 2, 20

[17] Jérôme Serp, Michel Allibert, Ondřej Beneš, Sylvie Delpech, Olga Feynberg, Véronique Ghetta, Daniel Heuer, David Holcomb, Victor Ignatiev, Jan Leen Kloosterman, et al. The molten salt reactor (msr) in generation iv: overview and perspectives. *Progress in Nuclear Energy*, 77:308–319, 2014. 3, 4

[18] Kairos Power LLC. Metallic Materials Qualification for the Kairos Power Fluoride Salt-Cooled High-Temperature Reactor, 2021. URL https://www.nrc.gov/docs/ML2118/ML21181A387.pdf. 4

[19] Yannick Guérin, Gary S Was, and Steven J Zinkle. Materials challenges for advanced nuclear energy systems. *Mrs Bulletin*, 34(1):10–19, 2009. 4

[20] V Ignatiev and A Surenkov. Material performance in molten salts. In *Comprehensive nuclear materials*, pages 221–250. 2012. 4, 5

[21] Dianqiang Jiang, Dalin Zhang, Xinyu Li, Shibao Wang, Chenglong Wang, Hao Qin, Yanwen Guo, Wenxi Tian, GH Su, and Suizheng Qiu. Fluoride-salt-cooled high-temperature reactors: Review of historical milestones, research status, challenges, and outlook. *Renewable and Sustainable Energy Reviews*, 161:112345, 2022. 4, 5

[22] MW Rosenthal, PR Kasten, and RB Briggs. Molten-salt reactors—history, status, and potential. *Nuclear Applications and Technology*, 8(2):107–117, 1970. 4

[23] Andrew Worrall, Benjamin R Betzler, George Flanagan, David Eugene Holcomb, Jianwei Hu, Donald N Kovacic, A L Qualls, and Louise G Worrall. Molten salt reactors and associated safeguards challenges and opportunities. 2018. 4

[24] Joel McDuffee and Kenneth Thoms. A review of molten salt irradiation experiments. 2019. 4

[25] Steven J Zinkle and GS Was. Materials challenges in nuclear energy. *Acta Materialia*, 61(3):735–758, 2013. 4

[26] GS Was, D Petti, S Ukai, and S Zinkle. Materials for future nuclear energy systems. *Journal of Nuclear Materials*, 527:151837, 2019. 4

[27] WD Manly. Fundamentals of liquid metal corrosion. *Corrosion*, 12(7):46–52, 1956. 4

[28] JH DeVan and RB Evans III. Corrosion behavior of reactor materials in fluoride salt mixtures. Technical report, Oak Ridge National Lab.(ORNL), Oak Ridge, TN (United States), 1962. 4

[29] MA Stopher. The effects of neutron radiation on nickel-based alloys. *Materials Science and Technology*, 33(5):518–536, 2017. 5, 6, 7, 9

[30] O Benes, C Cabet, S Delpech, P Hosnedl, V Ignatiev, R Konings, D Lecarpentier, O Matal, E Merle-Lucotte, C Renault, et al. Assessment of liquid salts for innovative applications. *ALISIA Deliverable (D-50), European Commission, Euratom Research and Training Programme on Nuclear Energy*, 2009. 5

[31] HE McCoy et al. Intergranular cracking of structural materials exposed to fuel salt. *ORNL/TM-4782*, pages 128–136, 1972. 5

[32] VV Ignatiev, VM Novikov, AI Surenkov, and VI Fedulov. The state of the problem on materials as applied to molten-salt reactor: problems and ways of solution. *Pre-print IAE-5678/11, Moscow*, 1993. 5

[33] V Ignatiev and A Surenkov. Corrosion phenomena induced by molten salts in generation iv nuclear reactors. In *Structural Materials for Generation IV Nuclear Reactors*, pages 153–189. Elsevier, 2017. 5

[34] WJ Mills. Fracture toughness of two ni-fe-cr alloys. *Engineering Fracture Mechanics*, 26(2):223–238, 1987. 7

[35] Frank A Garner and Howard R Brager. Swelling of austenitic iron-nickel-chromium ternary alloys during fast neutron irradiation. In *Effects of Radiation on Materials: Twelfth International Symposium, ASTM STP*, volume 870, pages 187–201, 1985. 7

[36] FW Wiffen. *Response of Inconel 600 to simulated fusion reactor irradiation*. ASTM International, 1979. 8

[37] Herbert Schroeder. High temperature helium embrittlement in austenitic stainless steels-correlations between microstructure and mechanical properties. *Journal of Nuclear Materials*, 155:1032–1037, 1988. 8

[38] WK Appleby, DW Sandusky, and UE Wolff. Swelling resistance of a high nickel alloy. *Journal of Nuclear Materials*, 43(3):213–218, 1972. 8, 9

[39] RM Boothby. The microstructure of fast neutron irradiated nimonic pe16. *Journal of nuclear materials*, 230(2):148–157, 1996. 9, 12, 81

[40] WJS Yang. Grain boundary segregation in solution-treated nimonic pe16 during neutron irradiation. *Journal of Nuclear Materials*, 108:339–346, 1982. 10

[41] Rudy Konings and Roger E Stoller. *Comprehensive nuclear materials*. Elsevier, 2020. 11

[42] Xiao-Ya Chen, A-Li Wen, Cui-Lan Ren, Cheng-Bin Wang, Wei Zhang, He-Fei Huang, Zhi-Wen Chen, and Ping Huai. Theoretical prediction of radiation-enhanced diffusion behavior in nickel under self-ion irradiation. *Nuclear Science and Techniques*, 31(8): 79, 2020. 12, 84, 85

[43] Eric Camus, Christian Abromeit, Françoise Bourdeau, Nelja Wanderka, and Heinrich Wollenberger. Evolution of long-range order and composition for radiation-induced precipitate dissolution. *Physical Review B*, 54(5):3142, 1996. 15, 80

[44] He K Zhang, Zhongwen Yao, Marquis A Kirk, and Mark R Daymond. Stability of ni 3 (al, ti) gamma prime precipitates in a nickel-based superalloy inconel x-750 under heavy ion irradiation. *Metallurgical and Materials Transactions A*, 45:3422–3428, 2014. 15, 80, 81

[45] P Changizian, Z Yao, C Lu, F Long, and MR Daymond. Radiation effect on nano-indentation properties and deformation mechanisms of a ni-based superalloy x-750. *Journal of Nuclear Materials*, 515:1–13, 2019. 15, 69, 80

[46] P Changizian, A Brooks, Z Yao, and MR Daymond. Nano-scale mechanical properties and microstructure of irradiated x-750 ni-based superalloy. *Metallurgical and Materials Transactions A*, 49(2):498–514, 2018. 15, 80

[47] Stephen Taller, Gerrit VanCoevering, Brian D Wirth, and Gary S Was. Predicting structural material degradation in advanced nuclear reactors with ion irradiation. *Scientific reports*, 11(1):2949, 2021. 15

[48] Yan-Ru Lin, Arunodaya Bhattacharya, and Steven J Zinkle. Analysis of position-dependent cavity parameters in irradiated metals to obtain insight on fundamental defect migration phenomena. *Materials & Design*, 226:111668, 2023. 16, 57

[49] Peter J Doyle, Kelsa M Benensky, and Steven J Zinkle. Modeling the impact of radiation-enhanced diffusion on implanted ion profiles. *Journal of Nuclear Materials*, 509:168–180, 2018. 16

[50] JB Whitley, GL Kulcinski, P Wilkes, and HV Smith Jr. The depth dependent damage profile in nickel irradiated with nickel or copper ions. *Journal of Nuclear Materials*, 79 (1):159–169, 1979. 17

[51] A Müller, V Naundorf, and M-P Macht. Point defect sinks in self-ion-irradiated nickel: a self-diffusion investigation. *Journal of applied physics*, 64(7):3445–3455, 1988. 17, 84

[52] HAYNES International. HAYNES International The Home of HASTELLOY and HAYNES Alloys, 2024. URL https://www.haynesintl.com/en/alloys/. 18, 20, 22

[53] Haynes International. haynes 282 brochures, 2015. URL https://haynesintl.com/docs/default-source/pdfs/new-alloy-brochures/high-temperature-alloys/brochures/282-brochure.pdf. 20, 66, 69

[54] M Kumar and VK Vasudevan. Ordering reactions in an ni 25mo 8cr alloy. *Acta materialia*, 44(4):1591–1600, 1996. 20, 21, 50, 82

[55] A Arya, GK Dey, Vijay K Vasudevan, and S Banerjee. Effect of chromium addition on the ordering behaviour of ni–mo alloy: experimental results vs. electronic structure calculations. *Acta Materialia*, 50(13):3301–3315, 2002. 21, 50

[56] HP Alloys. Hastelloy c-276, 2007. URL https://www.hpalloy.com/Alloys/descriptions/HASTELLOYC_276.aspx. 23

[57] Jun Lu, ES Choi, and HD Zhou. Physical properties of hastelloy® c-276™ at cryogenic temperatures. *Journal of applied physics*, 103(6), 2008. 23

[58] Rui Luo, Qingtao Liu, Pei Gao, Tian Liu, Hengnan Ding, Di Zhang, Yu Cao, and Xiaonong Cheng. Effect of microstructural evolution and mechanical properties of haynes 230 superalloy during long-term aging at 700° c. *Journal of Alloys and Compounds*, 947:169495, 2023. 23

[59] S Agarwal, Y Lin, C Li, RE Stoller, and SJ Zinkle. On the use of srim for calculating vacancy production: Quick calculation and full-cascade options. *Nuclear Instruments*

and Methods in Physics Research Section B: Beam Interactions with Materials and Atoms, 503:11–29, 2021. 26

[60] Hefei Huang, Xiaoling Zhou, Chaowen Li, Jie Gao, Tao Wei, Guanhong Lei, Jianjian Li, Linfeng Ye, Qing Huang, and Zhiyong Zhu. Temperature dependence of nickel ion irradiation damage in gh3535 alloy weld metal. *Journal of Nuclear Materials*, 497: 108–116, 2017. 26

[61] Yan-Ru Lin, Arunodaya Bhattacharya, Da Chen, Ji-Jung Kai, Jean Henry, and Steven J Zinkle. Temperature-dependent cavity swelling in dual-ion irradiated fe and fe-cr ferritic alloys. *Acta Materialia*, 207:116660, 2021. 26

[62] H Schroeder. High temperature embrittlement of metals by helium. *Radiation effects*, 78(1-4):297–314, 1983. 27

[63] APGM Bolshakov and GM Pharr. Influences of pileup on the measurement of mechanical properties by load and depth sensing indentation techniques. *Journal of materials research*, 13(4):1049–1058, 1998. 27

[64] William D Nix and Huajian Gao. Indentation size effects in crystalline materials: a law for strain gradient plasticity. *Journal of the Mechanics and Physics of Solids*, 46 (3):411–425, 1998. 27

[65] Peter Hosemann, Daniel Kiener, Yongqiang Wang, and Stuart A Maloy. Issues to consider using nano indentation on shallow ion beam irradiated materials. *Journal of Nuclear Materials*, 425(1-3):136–139, 2012. 27

[66] Warren Carl Oliver and George Mathews Pharr. An improved technique for determining hardness and elastic modulus using load and displacement sensing indentation experiments. *Journal of materials research*, 7(6):1564–1583, 1992. 28

[67] George M Pharr, Erik G Herbert, and Yanfei Gao. The indentation size effect: a critical examination of experimental observations and mechanistic interpretations. *Annual Review of Materials Research*, 40:271–292, 2010. 28

[68] Pengyuan Xiu, Hongbin Bei, Yanwen Zhang, Lumin Wang, and Kevin G Field. Stem characterization of dislocation loops in irradiated fcc alloys. *Journal of Nuclear Materials*, 544:152658, 2021. 32

[69] RK Ham. The determination of dislocation densities in thin films. *Philosophical Magazine*, 6(69):1183–1184, 1961. 32

[70] Yang Meng, Xinhua Ju, and Xiaopeng Yang. The measurement of the dislocation density using tem. *Materials Characterization*, 175:111065, 2021. 32

[71] LM Pike. Development of a fabricable gamma-prime (γ) strengthened superalloy. *Superalloys 2008*, pages 191–200, 2008. 37

[72] Ceena Joseph, Christer Persson, and Magnus Hörnqvist Colliander. Influence of heat treatment on the microstructure and tensile properties of ni-base superalloy haynes 282. *Materials Science and Engineering: A*, 679:520–530, 2017. 37

[73] KL Kruger. Haynes 282 alloy. In *Materials for ultra-supercritical and advanced ultra-supercritical power plants*, pages 511–545. Elsevier, 2017. 37

[74] SM Levine, Cristelle Pareige, Z Jiao, PD Edmondson, GS Was, SJ Zinkle, and A Bhattacharya. Phase instabilities in austenitic steels during particle bombardment at high and low dose rates. *Materials & Design*, 217:110588, 2022. 50

[75] Z Jiao and GS Was. Novel features of radiation-induced segregation and radiation-induced precipitation in austenitic stainless steels. *Acta Materialia*, 59(3):1220–1238, 2011. 50, 83

[76] A Verma, JB Singh, N Wanderka, and JK Chakravartty. Delineating the roles of cr and mo during ordering transformations in stoichiometric ni2 (cr1- x, mox) alloys. *Acta Materialia*, 96:366–377, 2015. 50

[77] Hani M Tawancy, Robert B Herchenroeder, and Aziz I Asphahani. High-performance ni-cr-mo-w alloys. *JOM*, 35(6):37–43, 1983. 55, 82, 83

[78] David Tabor. The hardness and strength of metals. *J. Inst. Metals*, 79:1, 1951. 65

[79] JR Cahoon, WH Broughton, and AR Kutzak. The determination of yield strength from hardness measurements. *Metallurgical transactions*, 2:1979–1983, 1971. 65

[80] TR Mann, MG Fahrmann, and MS Titus. Deformation-induced planar defects in immm ni2 (cr, mo, w) strengthened haynes® 244® superalloy. *Metallurgical and Materials Transactions A*, 54(5):1874–1885, 2023. 66, 75, 77

[81] Jiaao Liu, Weihong Zhang, Feiqiang Mei, Xin Xin, Yichao Cao, Chongwei Zhu, Qingao Liu, Xuhui Zhu, and Wenru Sun. Microstructure evolution and work hardening behaviour during cold deformation of haynes 214 superalloy. *Journal of Materials Research and Technology*, 24:5792–5804, 2023. 66, 73

[82] Young-Joo Kim, Jae-Hyeun Park, and Yong-Sik Ahn. Comparison of creep properties of cast and wrought haynes 282 superalloy. *Advances in Materials Science and Engineering*, 2018(1):2048959, 2018. 66

[83] TS Byun and K Farrell. Tensile properties of inconel 718 after low temperature neutron irradiation. *Journal of Nuclear Materials*, 318:292–299, 2003. 66

[84] TS Byun and K Farrell. Plastic instability in polycrystalline metals after low temperature irradiation. *Acta materialia*, 52(6):1597–1608, 2004. 66

[85] Haynes International. haynes 244 brochures, 2024. URL https://haynesintl.com/en/datasheet/haynes-244-alloy/. 66

[86] Haynes International. haynes 214 brochures, 2024. URL https://haynesintl.com/en/datasheet/haynes-214-alloy/. 66

[87] Pengcheng Zhu, Yajie Zhao, Yan-Ru Lin, Jean Henry, and Steven J Zinkle. Defect-specific strength factors and superposition model for predicting strengthening of ion irradiated fe18cr alloy. *Journal of Nuclear Materials*, page 154823, 2023. 67, 70

[88] Cameron C Clickner, JW Ekin, Najib Cheggour, CLH Thieme, Y Qiao, Y-Y Xie, and A Goyal. Mechanical properties of pure ni and ni-alloy substrate materials for y–ba–cu–o coated superconductors. *Cryogenics*, 46(6):432–438, 2006. 67

[89] HA Roth, CL Davis, and RC Thomson. Modeling solid solution strengthening in nickel alloys. *Metallurgical and Materials Transactions A*, 28:1329–1335, 1997. 67

[90] Anthony AW Thompson. Yielding in nickel as a function of grain or cell size. *Acta Metallurgica*, 23(11):1337–1342, 1975. 68

[91] Alfred Seeger, J Diehl, Siegfried Mader, and H Rebstock. Work-hardening and work-softening of face-centred cubic metal crystals. *Philosophical Magazine*, 2(15):323–350, 1957. 68

[92] SJ Zinkle. Fundamental radiation effects parameters in metals and ceramics. *Radiation effects and defects in solids*, 148(1-4):447–477, 1999. 68

[93] Lizhen Tan and Jeremy T Busby. Formulating the strength factor α for improved predictability of radiation hardening. *Journal of Nuclear Materials*, 465:724–730, 2015. 68, 69, 70, 91

[94] Steven J Zinkle and Yoshi Matsukawa. Observation and analysis of defect cluster production and interactions with dislocations. *Journal of nuclear materials*, 329:88–96, 2004. 68

[95] Kevin G Field, Xunxiang Hu, Kenneth C Littrell, Yukinori Yamamoto, and Lance L Snead. Radiation tolerance of neutron-irradiated model fe–cr–al alloys. *Journal of Nuclear Materials*, 465:746–755, 2015. 68

[96] Alan J Ardell. Precipitation hardening. *Metallurgical Transactions A*, 16(12):2131–2165, 1985. 69

[97] Na-Qiong Zhu, Wei Liu, Zhi-Chao Wang, and Xiao-Gang Lu. Modeling of molar volume for the ni–al γ/γ binary phases within the framework of calphad method. *Calphad*, 71: 101792, 2020. 69

[98] Xinghe Luan, Hongbo Qin, Fengmei Liu, Zongbei Dai, Yaoyong Yi, and Qi Li. The mechanical properties and elastic anisotropies of cubic ni3al from first principles calculations. *Crystals*, 8(8):307, 2018. 69

[99] AJE Foreman and MJ Makin. Dislocation movement through random arrays of obstacles. *Philosophical magazine*, 14(131):911–924, 1966. 70

[100] GR Odette and GE Lucas. Recent progress in understanding reactor pressure vessel steel embrittlement. *Radiation effects and defects in solids*, 144(1-4):189–231, 1998. 70

[101] Sylvain Queyreau, Ghiath Monnet, and Benoit Devincre. Orowan strengthening and forest hardening superposition examined by dislocation dynamics simulations. *Acta Materialia*, 58(17):5586–5595, 2010. 70

[102] Ulbrich. haynes 282 -uns-n07208, 2004. URL https://www.ulbrich.com/alloys/haynes-282-uns-n07208/. 71

[103] CKL Davies, P Nash, and RN Stevens. Precipitation in ni-co-al alloys: part 1 continuous precipitation. *Journal of Materials Science*, 15:1521–1532, 1980. 73, 90

[104] Eckhard Nembach, Stefan Schänzer, and Klaus Trinckauf. The antiphase boundary energy of γ precipitates in nickel-based superalloys. *Philosophical Magazine A*, 66(5): 729–738, 1992. 73

[105] Benjamin A Szajewski, Joshua C Crone, and Jaroslaw Knap. Analytic model for the orowan dislocation-precipitate bypass mechanism. *Materialia*, 11:100671, 2020. 79

[106] Nnaemeka Emmanuel Ugodilinwa, Matt Khoshdarregi, and Olanrewaju Akanbi Ojo. Analysis and constitutive modeling of high strain rate deformation behavior of haynes 282 aerospace superalloy. *Materials Today Communications*, 20:100545, 2019. 79

[107] Jiahao Cheng, Xiaohua Hu, Timothy Lach, and Xiang Frank Chen. A macro-micro approach for identifying crystal plasticity parameters for necking and failure in nickel-based alloy haynes 282. *International Journal of Plasticity*, 178:103997, 2024. 79

[108] BH Sencer, GM Bond, FA Garner, ML Hamilton, SA Maloy, and WF Sommer. Correlation of radiation-induced changes in mechanical properties and microstructural development of alloy 718 irradiated with mixed spectra of high-energy protons and spallation neutrons. *Journal of nuclear materials*, 296(1-3):145–154, 2001. 80

[109] Pooyan Changizian. *Radiation Damage Effect on Mechanical Properties and Microstructure of X-750 Ni-based Superalloy.* PhD thesis, Queen's University (Canada), 2018. 80

[110] N Hashimoto, JD Hunn, TS Byun, and LK Mansur. Microstructural analysis of ion-irradiation-induced hardening in inconel 718. *Journal of nuclear materials*, 318:300–306, 2003. 80

[111] CJ Baroch. *Properties of reactor structural alloys after neutron or particle irradiation*, volume 570. ASTM International, 1975. 80

[112] JD Hunn, EH Lee, TS Byun, and LK Mansur. Ion-irradiation-induced hardening in inconel 718. *Journal of nuclear materials*, 296(1-3):203–209, 2001. 80

[113] P Changizian, HK Zhang, and Z Yao. Effect of simultaneous helium implantation on the microstructure evolution of inconel x-750 superalloy during dual-beam irradiation. *Philosophical Magazine*, 95(35):3933–3949, 2015. 80

[114] M Raghavan, BJ Berkowitz, and JC Scanlon. Electron microscopic analysis of heterogeneous precipitates in hastelloy c-276. *Metallurgical Transactions A*, 13:979–984, 1982. 81

[115] JI Akhter, MA Shaikh, M Ahmad, M Iqbal, KA Shoaib, and W Ahmad. Effect of aging on the hardness and impact properties of hastelloy c-276. *Journal of Materials Science Letters*, 20:333–335, 2001. 82, 83

[116] Gregory Edward Gdowski. Survey of degradation modes of four nickel-chromium-molybdenum alloys. Technical report, Lawrence Livermore National Lab.(LLNL), Livermore, CA (United States), 1991. 82

[117] YL Lu, LM Pike, CR Brooks, PK Liaw, and DL Klarstrom. Strengthening domains in a ni–21cr–17mo alloy. *Scripta materialia*, 56(2):121–124, 2007. 82

[118] L Karmazin. Lattice parameter studies of structure changes of ni cr alloys in the region of ni2cr. *Materials Science and Engineering*, 54(2):247–256, 1982. 82

[119] L Karmazin, J Krejčí, and J Zeman. γ phase and ni2cr-type long-range order in ni-rich nicrmo alloys. *Materials Science and Engineering: A*, 183(1-2):103–109, 1994. 82

[120] Jie Song, Robert Field, Doug Konitzer, and Michael Kaufman. Development of grain boundary precipitate-free zones in a ni-mo-cr-w alloy. *Metallurgical and Materials Transactions A*, 48:2425–2434, 2017. 82

[121] Huang HF, Li JJ, Liu RD, Lei GH, He SX, Q Huang, and L Yan. Nanostructure variations and their effects on mechanical strength of ni-17mo-7cr alloy under xenon ion irradiation. *Materials Transactions*, 55(8):1243–1247, 2014. 82

[122] Jinxi LIU, Jixiang ZHANG, Yanling LU, Xiaoke LI, Zhijun LI, and Xingtai ZHOU. Effect of long-term aging on microstructure and mechanical properties of alloy c276. *Acta Metall Sin*, 49(6):763–768, 2013. 83

[123] Chi Zhang, Liwen Zhang, Yan Cui, Qiyan Feng, and Congqian Cheng. Effects of high-temperature aging on precipitation and corrosion behavior of a ni-cr-mo-based hastelloy c276 superalloy. *Journal of Materials Engineering and Performance*, 29: 2026–2034, 2020. 83

[124] FG Hodge and RW Kirchner. An improved ni-cr-mo alloy for corrosion service. *Corrosion*, 32(8):332–336, 1976. 83

[125] Frank S Ham. Theory of diffusion-limited precipitation. *Journal of Physics and Chemistry of Solids*, 6(4):335–351, 1958. 83, 89

[126] J. Dong S. Jiao, G. Zhu and Q. Zhang. Carbide evolution and mo depletion law in hastelloy c-276. *J. Mater. Eng.,*, 1:47–56, 2011. 83

[127] K Maier, H Mehrer, E Lessmann, and W Schüle. Self-diffusion in nickel at low temperatures. *Physica status solidi (b)*, 78(2):689–698, 1976. 84

[128] Hao Sun and Laurent Karim Béland. Statistical distribution of spontaneous recombination radii of frenkel pairs in fcc and bcc metals. *Acta Materialia*, 229:117814, 2022. 84

[129] WG Wolfer. Fundamental properties of defects in metals. *Comprehensive nuclear materials*, 1:1–45, 2012. 84

[130] SL Dudarev. Density functional theory models for radiation damage. *Annual Review of Materials Research*, 43(1):35–61, 2013. 84

[131] Carelyn E Campbell, William J Boettinger, and Ursula R Kattner. Development of a diffusion mobility database for ni-base superalloys. *Acta Materialia*, 50(4):775–792, 2002. 84

[132] NQ Lam and H Wiedersich. Bombardment-induced segregation and redistribution. *Nuclear Instruments and Methods in Physics Research Section B: Beam Interactions with Materials and Atoms*, 18(1-6):471–485, 1986. 84

[133] Kai Nordlund, Steven J Zinkle, Andrea E Sand, Fredric Granberg, Robert S Averback, Roger E Stoller, Tomoaki Suzudo, Lorenzo Malerba, Florian Banhart, William J Weber, et al. Primary radiation damage: A review of current understanding and models. *Journal of Nuclear Materials*, 512:450–479, 2018. 84

[134] SJ Zinkle and RE Stoller. Quantifying defect production in solids at finite temperatures: Thermally-activated correlated defect recombination corrections to dpa (crc-dpa). *Journal of Nuclear Materials*, 577:154292, 2023. 85

[135] Donghua Xu, Alicia Certain, Hyon-Jee Lee Voigt, Todd Allen, and Brian D Wirth. Ballistic effects on the copper precipitation and re-dissolution kinetics in an ion irradiated and thermally annealed fe–cu alloy. *The Journal of chemical physics*, 145 (10), 2016. 85

[136] Yajie Zhao, Arunodaya Bhattacharya, Cristelle Pareige, Caleb Massey, Pengcheng Zhu, Jonathan D Poplawsky, Jean Henry, and Steven J Zinkle. Effect of heavy ion irradiation dose rate and temperature on α precipitation in high purity fe-18% cr alloy. *Acta Materialia*, 231:117888, 2022. 86, 87, 88, 89

[137] MSA Karunaratne, P Carter, and RC Reed. On the diffusion of aluminium and titanium in the ni-rich ni–al–ti system between 900 and 1200 c. *Acta materialia*, 49(5):861–875, 2001. 87, 88, 91

[138] Ilya M Lifshitz and Vitaly V Slyozov. The kinetics of precipitation from supersaturated solid solutions. *Journal of physics and chemistry of solids*, 19(1-2):35–50, 1961. 90

[139] C Wagner. Theory of the aging of precipitates by dissolution-reprecipitation (ostwald ripening). *Z Elektrochem*, 65(7):581–11, 1961. 90

[140] A Baldan. Review progress in ostwald ripening theories and their applications to nickel-base superalloys part i: Ostwald ripening theories. *Journal of materials science*, 37:2171–2202, 2002. 90, 91

[141] CKL Davies, P Nash, and R N_ Stevens. The effect of volume fraction of precipitate on ostwald ripening. *Acta metallurgica*, 28(2):179–189, 1980. 90

[142] JMG Crompton, RM Waghorne, and GB Brook. The estimation of size distribution and density of precipitates from electron micrographs of thin foils. *British Journal of Applied Physics*, 17(10):1301, 1966. 115

[143] WA Cassada, GJ Shiflet, and EA Starke. The effect of plastic deformation on al 2 culi (t 1) precipitation. *Metallurgical Transactions A*, 22:299–306, 1991. 115

[144] Mats Hättestrand and Hans-Olof Andren. Evaluation of particle size distributions of precipitates in a 9% chromium steel using energy filtered transmission electron microscopy. *Micron*, 32(8):789–797, 2001. 115

[145] Thomas Dorin, Patricia Donnadieu, Jean-Marc Chaix, Williams Lefebvre, Frédéric De Geuser, and Alexis Deschamps. Size distribution and volume fraction of t1 phase precipitates from tem images: Direct measurements and related correction. *Micron*, 78:19–27, 2015. 115

Appendix A

Additional information

A.1 Large precipitate size correction

Many efforts have been made to correct the distribution of the disk-shaped precipitates of two-dimensional projected images since the 1960s [142, 143, 144, 145]. In this study, we adopted the concept of a probability matrix proposed by Dorin [145] and incorporated modifications inspired by Crompton's derivation [142].

The key parameters are defined below:

k: Number of classes

Δ: Width of each class, $\Delta = (D_{max} - D_{min})/k$

D_i: The observed diameter of the long axis of projected particles, $D_i = D_{min} + (i + 1/2)\Delta$

Y: Distance of the particle centred outside the slide

P_{ij}: Probability of a particle whose projected diameter falls into D_i with a true diameter D_j.

N_m^i: Number of particles in i class measured from the TEM image

N_c^i: Number of particles in i class after correction

t: TEM sample thickness

The schematic side view of the intersection effect on precipitates is shown in Fig.A.1. The probability of a precipitate centred outside the slice leading to smaller observed sizes $j > i$ is described in Equ.A.1.

$$
\begin{aligned}
P(i,j) &= \frac{2\,|dy_i|}{t+D_j} = \frac{1}{t+D_j}\int_{D_i-\frac{1}{2}\Delta}^{D+\frac{1}{2}\Delta} \frac{D}{\sqrt{D_j^2-D_i^2}}dD \\
&= \frac{1}{t+D_j}\left(\sqrt{D_j^2-\left(D_i-\frac{1}{2}\Delta\right)^2}-\sqrt{D_j^2-\left(D_i+\frac{1}{2}\Delta\right)^2}\right)
\end{aligned}
\tag{A.1}
$$

The probability of a precipitate that the observed size and true diameter belong to the same class is described in Equ.A.2, including two terms:(1) the center of precipitates located inside sample, and (2) the center of the precipitates slightly located outside the Tem sample while the observed size and true size still falling into the same group.

$$
\begin{aligned}
P(i,i) &= \frac{t}{t+D_i} + \frac{1}{t+D_i}\int_{D_i-\frac{1}{2}\Delta}^{D_i} \frac{D}{\sqrt{D_j^2-D_i^2}}dx \\
&= \frac{t}{t+D_i} + \frac{1}{t+D_i}\sqrt{D_i^2-\left(D_i-\frac{1}{2}\Delta\right)^2}
\end{aligned}
\tag{A.2}
$$

The measured number N_m and corrected number N_c are presented as vectors. They can transform to each other by possibility matrix as shown in Equ.A.3. Thus, the number density of precipitates after correction can be calculated by $N_c = P^{-1} \times N_m$.

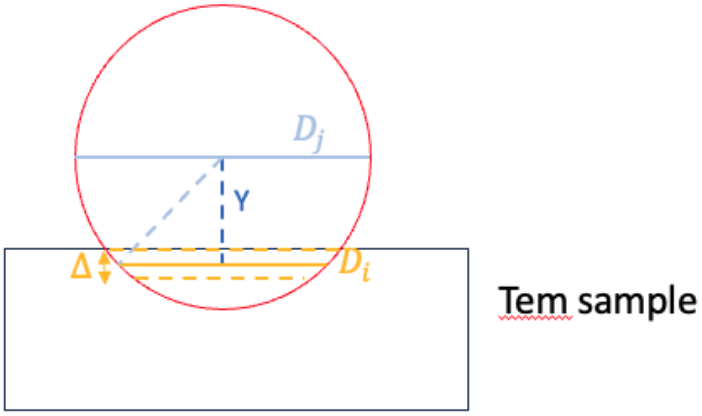


Figure A.1: The schematic representation of precipitates from side view.

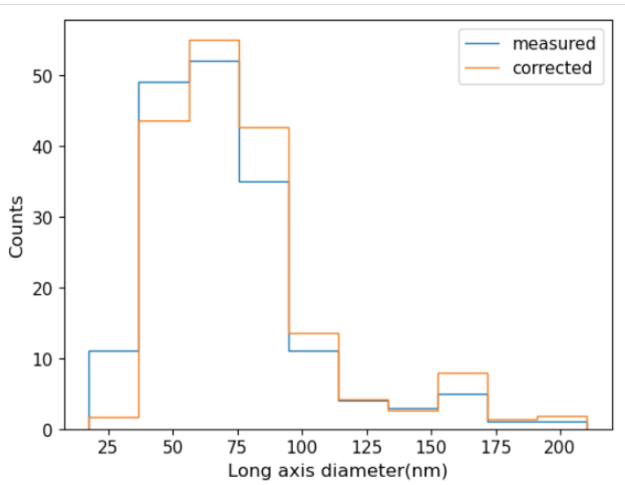


Figure A.2: An example of the size distribution of $Ni_2(Mo, Cr, W)$ precipitates' diameters before and after correction.

$$\begin{pmatrix} N_m^1 \\ N_m^2 \\ \vdots \\ N_m^{imax} \end{pmatrix} = \begin{pmatrix} P_{11} & P_{12} & \cdots & P_{1,imax} \\ 0 & P_{22} & \cdots & \vdots \\ \vdots & \vdots & P_{ij} & \vdots \\ 0 & 0 & \cdots & P_{imax,imax} \end{pmatrix} * \begin{pmatrix} N_c^1 \\ N_c^2 \\ \vdots \\ N_c^{imax} \end{pmatrix} \tag{A.3}$$

In Fig. **??**(b), the maximum diameter is approximately 200 nm, while the TEM lamella thickness ranges from 85 to 100 nm, making it appropriate for the correction of the truncation and intersection effects. Figure.A.2 illustrates the initial and corrected size distribution of one variant of $Ni_2(Mo, Cr, W)$ precipitates along the long direction in the unirradiated aged Haynes 244. The uncorrected and corrected average diameters are 77.4 and 71.1 nm, respectively. The difference between these values is relatively small compared to the standard deviation, suggesting that the correction to the remaining samples may not be necessary. Overall, the average diameter of precipitates in the unirradiated sample is approximately 73.8 ± 31.2 nm, and the average thickness is about 20.1 ± 6.1 nm.

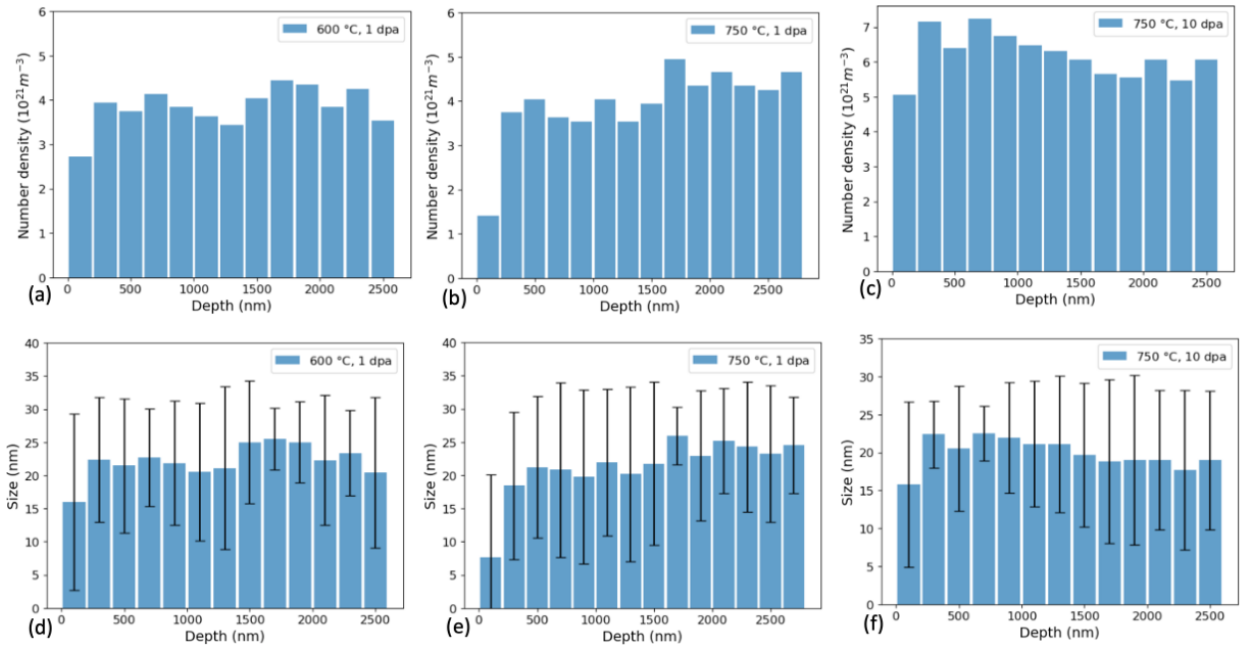


Figure A.3: The statistical depth dependence of (a)-(c) precipitate counts and (d)-(f) size distribution of γ' precipitates in irradiated Haynes 282. Subfigures (a) and (d) correspond to the 600 °C, 1 dpa sample; (b) and (e) represent the 750 °C, 1 dpa sample; (c) and (f) depict the 750 °C, 10 dpa sample.

A.2 Phase stability

A.2.1 γ' precipitates

The depth dependence for EDS mapping of Ti-enriched precipitates in Haynes 282 under different irradiation conditions is plotted in Fig.A.3. We did not observe a discernible dose-dependent trend in the size and count of γ' precipitates, except for the first 200 nm from the sample surface, where precipitate counts were notably lower than in other depth groups since the element label partially blocked the images. The fluctuations observed may be attributed to human counting errors and sample thickness variation. The detailed statistical information on precipitates in Haynes 282 is listed in Table. A.1.

Unlike the aged Haynes 282 containing γ' precipitates before the irradiation, precipitation occurred during irradiation and thermal exposure in Haynes 214. The relevant precipitate information is listed in Table. A.2.

Table A.1: Results of STEM-EDS analysis showing the size (average diameter), number density and volume fraction of γ' precipitates

		Irradiated region (500-1000nm)			Pristine region (2200-2700nm)		
Dose (dpa)	Temperature (℃)	Average diameter (nm)	Number density (10^{21}/m^3)	Volume fraction (%)	Average diameter (nm)	Number density (10^{21}/m^3)	Volume fraction (%)
1	600	25.3 ± 4.0	5.4 ± 1.2	4.5	25.16 ± 4.3	5.6 ± 1.5	4.7
10	600	29.4 ± 4.0	6.5 ± 1.7	8.7	27.5 ± 3.5	6.7 ± 1.7	7.3
1	750	28.3 ± 4.9	5.0 ± 1.3	5.3	27.4 ± 4.3	5.6 ± 1.5	5.9
10	750	25.3 ± 3.7	7.4 ± 1.9	6.3	24.1 ± 3.5	6.8 ± 1.8	5.1
0	RT				29.3 ± 4.8	5.1 ± 1.3	6.8

Table A.2: Size and number density of precipitates in Haynes 214 under various irradiation conditions

Counting region	Irradiation condition	Precipitate	
		Diameter (nm)	Number density ($/\times 10^{21} m^3$)
Irradiated region 500 -1000 nm	600 °C, 1 dpa	10.4 ± 1.5	40.9 ± 8.57
	600 °C, 10 dpa	13.0 ± 2.3	42.3 ± 9.23
	750 °C, 1 dpa	16.5 ± 3.25	14.2 ± 3.5
	750 °C, 10 dpa	29.1 ± 4.3	8.3 ± 1.8
Pristine region >2500 nm	600 °C, 1 dpa	9.1 ± 2.1	32.1 ± 7.2
	600 °C, 10 dpa	8.6 ± 1.3	65.2 ± 14.5
	750 °C, 1 dpa	11.8 ± 2.5	14.7 ± 0.4
	750 °C, 10 dpa	27.1 ± 5.9	7.3 ± 1.6

A.2.2 Ni_2(Mo, Cr, W) precipitates

The detailed STEM-EDS results of 600 °C, 10 dpa sample and 750 °C, 1 dpa Haynes 244 STD are plotted in Fig. A.4 and Fig. A.5, respectively.

The corresponding data of precipitates under all irradiation conditions in aged Haynes 244STD and solutionized Haynes 244SHT are listed in the Table. A.3 and A.4, respectively.

A.2.3 Simulation of electron diffraction pattern

Considering Cr carbides were also observed in the pristine region, as shown in Fig.4.17(a), it suggest that this phase is thermodynamically favorable in the phase diagram. The two possible phases that meet the high Cr content requirement are $Cr_{23}C_6$ and Cr_7C_3. However, Cr_7C_3 has a hexagonal crystal structure, which is coherent with the FCC Ni matrix. Thus, we finally focused on simulating with Ni, γ' and $Cr_{23}C_6$phases. The crystal structural information of each phase is obtained from the ICSD database for completely identified inorganic crystal structures. Minor deviations in lattice parameters may exist compared to real-world samples. The simulated multi-phase electron diffraction pattern is plotted in Fig.A.6, where the indices correspond to each phase and are color-coded for clarity. All phases are observed along the [001] zone axis and the final simulated multi-phase diffraction pattern matches precisely with the experimental diffraction pattern observed in the irradiated region of 750 °C, 1 dpa Haynes 214. This confirms the presence and identification of these phases in Haynes 214 irradiated at this condition.

A.3 Nanoindentation hardness

The summary of the pileup-corrected H_0 and h^* are listed in Tables from A.5 to A.8.

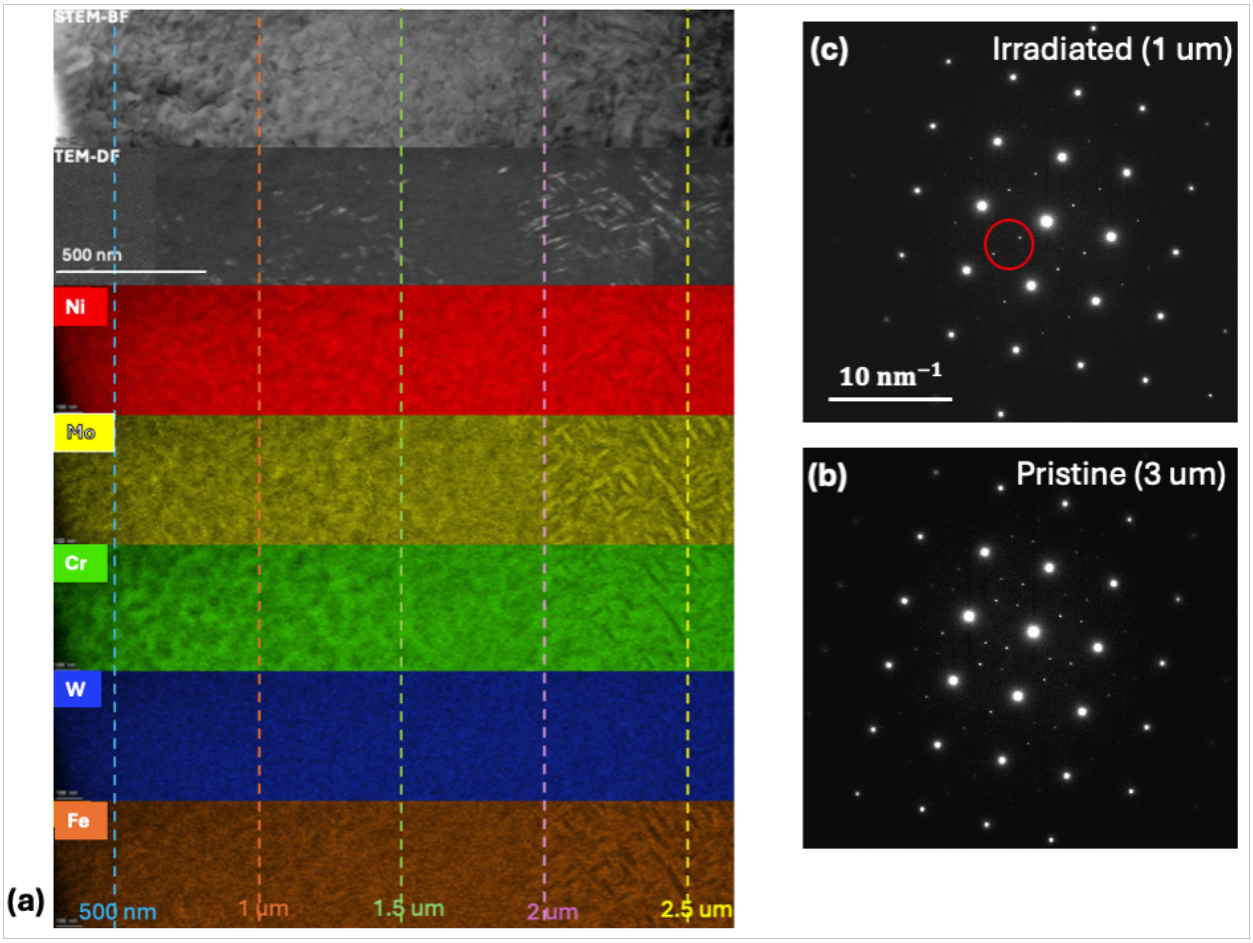


Figure A.4: (a) Micrographs showing the evolution of precipitates in aged Haynes 244 under Ni ion irradiation at 600 °C, up to a midrange dose of 10 dpa; (b) and (c) are selected area electron diffraction patterns captured from the region of the irradiated region (at a depth of 1 μm) and pristine region (at 3 μm.)

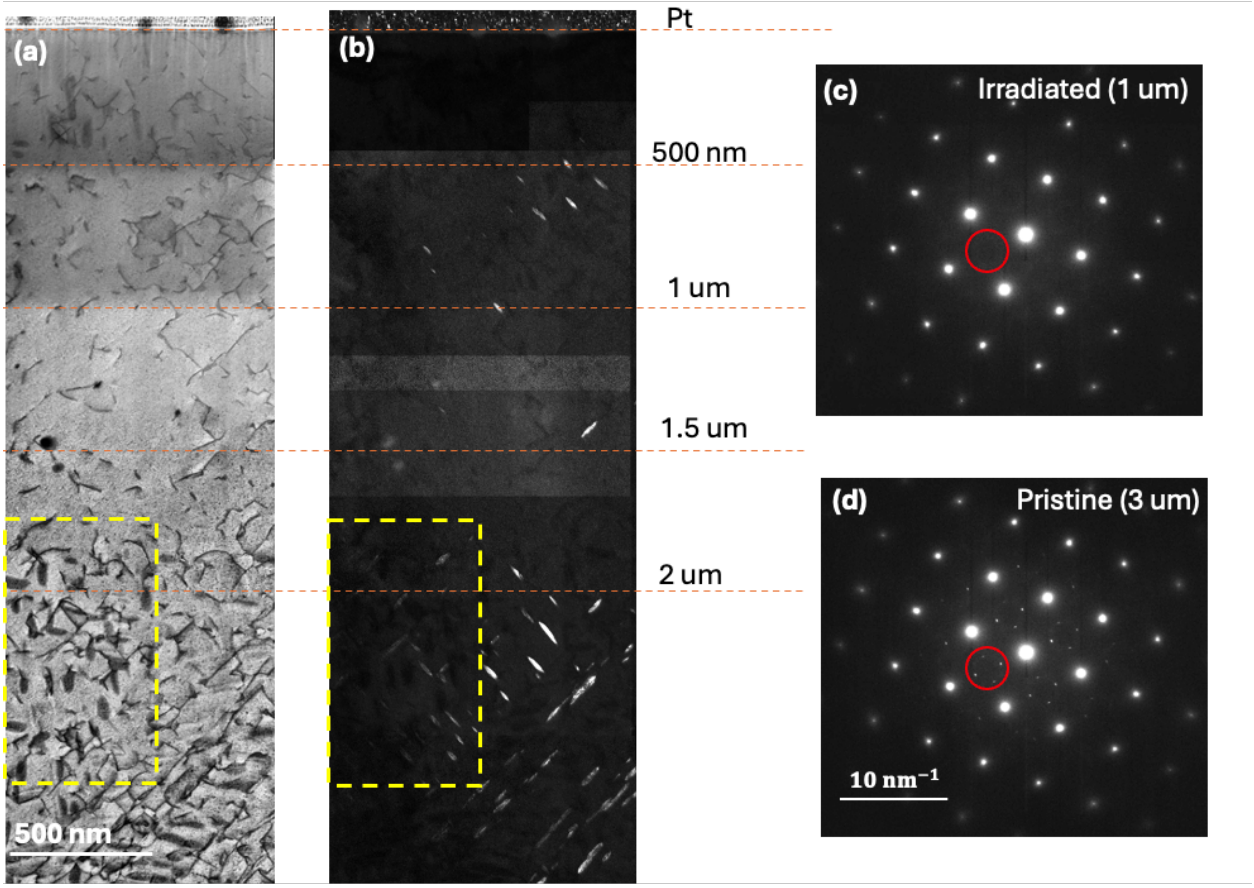


Figure A.5: (a)STEM-bright field image and (b) TEM-dark field image of aged Haynes 244 irradiated at 750 °C with a mid-range dose of 1 dpa. (c) and (d) are selected area electron diffraction patterns captured from the region of the irradiated region (at a depth of 1 μm) and pristine region (at 3 μm.)

Table A.3: Size and number density of features observed in aged Haynes 244 under various irradiation conditions

Counting region	Irradiation condition	Precipitate				Dislocation loop		Dislocation Line
		Diameter (nm)	Thickness (nm)	Number density ($/\times 10^{21} m^3$)	Approximate volume fraction	Diameter (nm)	Number density ($/10^{21} m^3$)	Dislocation density ($/\times 10^{14} m^2$)
Irradiated region 500 -1000 nm	600 °C, 1 dpa	67.0 ± 38.9	19.2 ± 8.6	2.2 ± 0.6	0.15	13.4 ± 5.9	1.1 ± 0.2	3.9 ± 0.9
	600 °C, 10 dpa	52.1 ± 16.0	23.1±4.3	1.0 ± 0.2	0.05	26.3 ± 10.8	0.9 ± 0.2	2.0 ± 0.4
	750 °C, 1 dpa	36.1 ± 15.7	9.6 ± 2.5	1.4 ±0.3	0.01			2.0 ± 0.5
	750 °C, 10 dpa	61.7± 31.2	17.1 ±8.0	2.1 ± 0.4	0.11			1.1 ± 0.2
Pristine region >2500 nm	600 °C, 1 dpa	76.9 ± 45.1	19.72±8.49	1.9 ± 0.5	0.18			3.4 ± 0.8
	600 °C, 10 dpa	59.0 ± 22.9	17.37±5.71	2.9 ± 0.6	0.14			2.9 ± 0.14
	750 °C, 1 dpa	49.5 ± 24.2	11.17±3.34	4.9 ± 1.1	0.11			2.0 ± 0.4
	750 °C, 10 dpa	72.7 ± 35.9	15.69±5.5	2.3 ± 0.5	0.15			1.8 ± 0.4
Entire region	Unirradiated sample	73.8 ± 31.2	20.1 ± 6.1	2.3 ± 0.5	0.19			3.3 ± 0.8

Table A.4: Size and number density of features observed in solutionized Haynes 244 under various irradiation conditions

Counting region	Irradiation condition	Precipitate			Dislocation loop		Dislocation Line
		Diameter (nm)	Thickness (nm)	Number density ($/\times 10^{21} m^3$)	Diameter (nm)	Number density ($/10^{21} m^3$)	Dislocation density ($10^{14}/m^2$)
Irradiated region 500 -1000 nm	600 °C, 1 dpa	21.7 ± 6.5	6.7 ± 1.4	12.9 ± 2.8	10.8 ± 2.4	0.37 ± 0.09	0.9 ± 1.3
	600 °C, 10 dpa	34.4 ± 20.0	12.1 ± 5.9	8.3 ± 0.2	9.5 ± 4.1	0.18 ± 0.04	
	750 °C 1 dpa						
	750 °C, 10 dpa	73.9 ± 15.1	20 ± 3.6	1.4 ± 0.3			

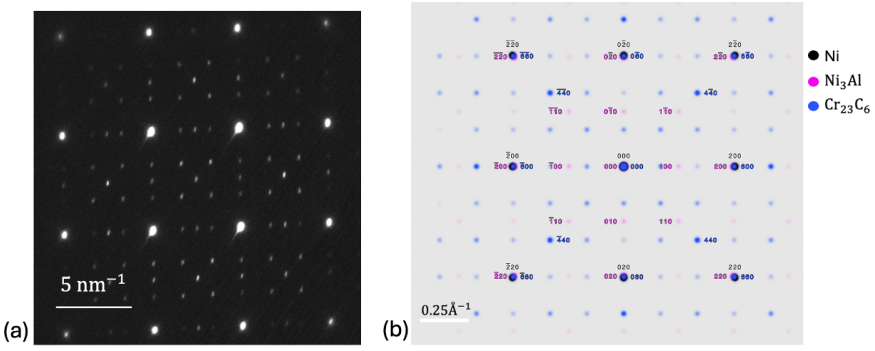


Figure A.6: (a) The selected area electron diffraction pattern of irradiated Haynes 214 (750 °C, 1 dpa); (b) The simulated multi-phase electron diffraction pattern consists of Ni, $\gamma' - Ni_3Al$ and $Cr_{23}C_6$ phases. All separate phases are observed from the [001] zone axis, simulated with SingleCrystal software.

Table A.5: Nanoindenation summary of Haynes 282 under various conditions

Heat Treatment	Condition	H_0 (GPa)	h^* (nm)
Solution treatment	Unirradiated	3.2 ± 0.4	171
Aging	Unirradiated	4.1 ± 0.4	108
	600 °C, 1 dpa	4.2 ± 0.5	65
	600 °C, 10 dpa	4.7 ± 0.4	34
	750 °C, 1 dpa	4.6 ± 0.5	54
	750 °C, 10 dpa	4.6 ± 0.3	56

Table A.6: Nanoindentation summary of Haynes 214 under various conditions

Condition	H_0 (GPa)	h^* (nm)
Unirradiated	2.4 ± 0.2	553 ±2
600 °C, 1 dpa	3.3 ± 0.4	124±5
600 °C, 10 dpa	3.8 ± 0.4	60 ± 3
750 °C, 1 dpa	4.1 ± 0.5	60 ± 4
750 °C, 10 dpa	4.3 ± 0.5	61 ± 4

Table A.7: Nanoindentation summary of aged Haynes 244 under various conditions

Condition	H_0 (GPa)	h^* (nm)
Unirradiated	5.0 ± 0.3	99 ± 1
600 °C, 1 dpa	4.9 ± 0.5	62 ± 3
600 °C, 10 dpa	4.7 ± 0.4	30 ± 2
750 °C, 1 dpa	4.1 ± 0.4	48 ± 2
750 °C, 10 dpa	4.7 ± 0.3	18 ± 1

Table A.8: Nanoindentation summary of aged Haynes 244 under various conditions

Condition	H_0 (GPa)	h^* (nm)
Unirradiated	3.1 ± 0.4	123 ± 4
600 °C, 1 dpa	3.7 ± 0.7	148 ± 17
600 °C, 10 dpa	4.8 ± 0.6	62 ± 4
750 °C, 1 dpa	3.3 ± 0.3	98 ± 5
750 °C, 10 dpa	4.4 ± 0.4	38 ± 1

Vita

Qinyun Chen grew up in Shanghai, China. She received her Bachelor's in Nuclear Engineering from Fudan University in the summer of 2018. After that, she joined Dr. Steven Zinkle's research group at the University of Tennessee, Knoxville (UTK), for a Ph.D. study on radiation damage on nuclear materials. In the same period, she earned the M.S. degree in Materials Science and Engineering at the UTK in May 2021 and the M.S. degree in Computer Science at the Georgia Institute of Technology in May 2024. She received a Ph.D. degree in Nuclear Engineering in December 2024.